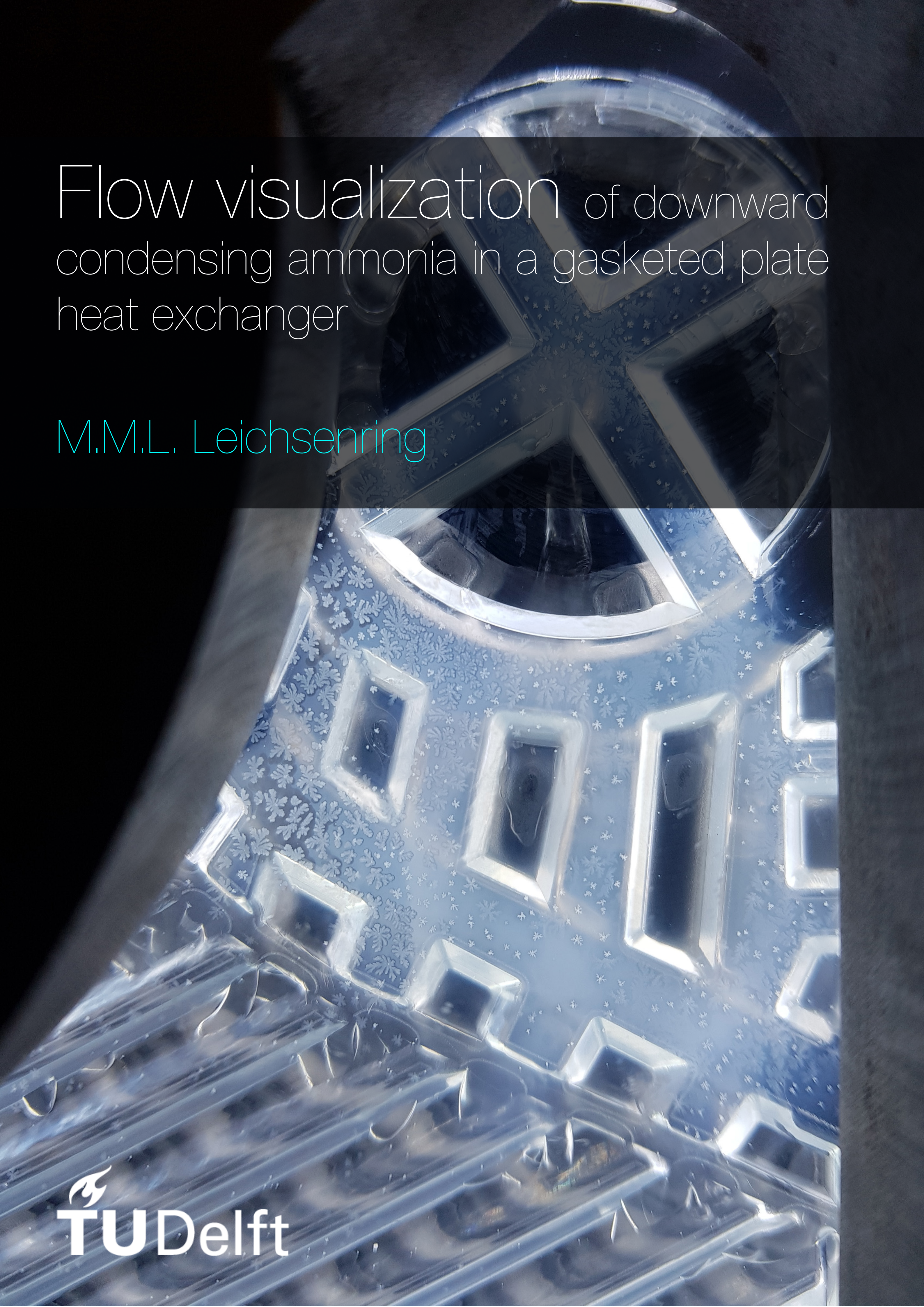

Flow visualization of downward condensing ammonia in a gasketed plate heat exchanger

M.M.L. Leichsenring

Flow visualization of downward condensing ammonia in a gasketed plate heat exchanger

by

M.M.L. Leichsenring

to obtain the degree of Master of Science

at the Delft University of Technology,

to be defended publicly on Wednesday April 24, 2019 at 10:00 AM.

Student number:	4014391	
Project duration:	April 1, 2018 - April 24, 2019	
Thesis committee:	Dr. ir. C.A. Infante Ferreira,	TU Delft, supervisor
	Dr. ir. W. P. Breugem,	TU Delft
	Dr. O. Moultos,	TU Delft
	Ir. J. Kirkenier,	Bluerise B.V., supervisor
	X. Tao, MSc.,	TU Delft, daily supervisor

This thesis is confidential and cannot be made public until April 24, 2024.

TU Delft

Summary

Ocean Thermal Energy Conversion (OTEC) uses the temperature difference between the surface and deep layers to generate electricity. The temperatures in the ocean hardly vary between day and night or between the seasons, which ensures a very constant energy production with OTEC. In order for OTEC to compete with the current forms of energy production, optimization is necessary such that costs are reduced to make OTEC power generation economically feasible. In cooperation with the Delft University of Technology, Bluerise B.V. constructed a small scale OTEC-plant to test the performance of the OTEC-cycle and optimize its outputs. The 100 W OTEC demo consists of an organic Rankine cycle using ammonia as the working fluid that is downward condensed in a gasketed plate heat exchanger (GPHE).

Plate heat exchangers (PHEs) have a wide range of applications due to their superior performance in relation to favourable heat transfer coefficients (HTCs), compactness, design flexibility and thermal effectiveness (Thulukannam, [46]). However, the two-phase behaviour inside the PHEs is yet not fully understood, resulting in over- or underestimating by several published heat transfer and pressure drop correlations, which are limited by the range of conditions they cover (Amalfi et al.[5]). Tao et al.[45] conclude that better predictions of flow patterns and dominant physical phenomena in PHEs will improve the calculation of heat transfer and pressure drop. Therefore, the goal in this research is to identify the flow patterns that occur in the GPHE, gain more knowledge on the dominant physical phenomena and how they relate to the performance. In the future, this can be used to increase the accuracy of performance calculations of the condenser. Flow visualization experiments are performed on the GPHE to identify the flow patterns and how they relate to the performance of the GPHE. A visualization section including a transparent plate is designed in the OTEC demo that allows for flow visualization.

The first part of this thesis involves material research on glass and several polymers to produce the transparent plate. The setup requires a plate that is chemically compatible with ammonia and has a mechanical performance that is fit for the operational pressures inside the GPHE. Chemical tests prove that Polystyrene is chemically well resistant to ammonia for four days. The results of a finite element analysis predict that the mechanical performance of PMMA is promising but glass is critical for the GPHE. To ensure a safe setup, a material combination of PS/PMMA is selected. A visualization plate is manufactured from a corrugated PS layer on top of a thick PMMA base plate. The PS layer acts as a chemical resistant barrier between ammonia and the PMMA base, while PMMA ensures the mechanical performance. However, after 7 days of performing the visualization experiments, the plate showed limited durability with respect to ammonia, as cracks in the material emerged and the plate lost its transparency.

The second part of the research in this thesis involves two types of experiments. The first type involves flow visualization experiments on a single-channel configuration. For all conditions, only film flow and partial film flow are observed. A low mass flux shows partial film flow with a smooth film, and a high mass flux corresponds to film flow with rough film characteristics. Partial film flow includes dry-out areas on the plate, and it is concluded that these surface area voids increase with vapor quality and volumetric void fraction. Mass flux contributes to a pressure drop increase and therefore film flow corresponds to a higher pressure drop in the PHE with respect to partial film flow. The HTCs increase with mass flux but mainly with vapor quality. However, there seems to be an optimum for the HTCs with increasing vapor quality when partial film flow is observed. For partial film flow, the surface area voids increase with vapor quality and for large voids the slope of the HTCs decay. It is concluded that surface area voids have a negative influence on the HTCs. Inertia and surface tension forces are dominant phenomena in the GPHE for these experimental conditions and influence the flow pattern. Proposed flow patterns maps by previous studies are not in accordance with the observed flow patterns inside the GPHE for the current experimental conditions. For this reason, a flow pattern map for downward condensing ammonia that includes the dominant phenomena is proposed for this experimental configuration and conditions. The second type of experiments involves multi-channel experiments without visualization to predict the flow patterns for lower mass fluxes. The slope of the HTCs followed the same trend with increasing vapor quality for the observed partial film flow in the visualization experiments. This indicates that partial film flow occurs in the multi-channel configuration of the GPHE.

Acknowledgements

First of all, I would like to thank my supervisor Carlos Infante Ferreira for his excellent supervision. The frequent meetings, attention to detail and constructive feedback ensured great support during my thesis and contributed in keeping me motivated. I am also very grateful to my daily supervisor Xuan Tao, I have always felt welcome for asking questions and I have found a lot of comfort in your advise and suggestions on how to improve this work. I would also like to thank Joost Kirkenier for offering the opportunity to graduate at Bluerise B.V., being my supervisor at the company and offering the freedom on how to approach the thesis assignment. I am grateful for the advise given by the employees at the DEMO on material selection and production of the required components for this thesis.

Furthermore, I would like to thank my dear friends at the TU Delft for all the laughter, kindness and emotional support when I was in need of it. Especially Pjotr, Shreyas and Dionne, you made the time spent in the Master's a true adventure. I would very much like to thank my parents on supporting me the entire duration at the TU Delft, and allowing to perform many extracurricular activities which contributed to my personal development on many other fields. I would like to thank my grandmother for all the celebrations that we held every time I achieved progress during my thesis. And last but certainly not least, I would like to especially thank my partner, Maarten, for the countless cheer up sessions and firm belief in my capabilities. I am truly grateful for your positive and cheery attitude, never failing to make my day.

Contents

Nomenclature

Abbreviations

ABS	Acrylonitrile butadiene styrene
FEA	Finite element analysis
GPHE	Gasketed plate heat exchanger
HFC	Hydrofluorcarbons
HTC	Heat transfer coefficient
ORC	Organic Rankine cycle
OTEC	Ocean thermal energy conversion
PC	Polycarbonate
PETG	Terephthalate Glycol
PFV	Photron FASTCAM Viewer
PHE	Plate heat exchanger
PMMA	Polymethylmethacrylaat
PP	Polypropylene
PS	Polystyrene
PSU	Polysulfone
PVC	Polyvinylchloride
SWAC	Seawater air conditioning
RMSE	Root mean squared error
SSE	Sum of squares due to error

Dimensionless quantities

Bd	Bond number
Co	Confinement number
Fr	Froude number
Ga	Galileo number
Nu	Nusselt number
Pr	Prandtl number
Re	Reynolds number
Re_{eq}	Equivalent Reynolds number
Re_f	Film Reynolds number
Re_{LO}	Liquid only Reynolds number
We	Weber number

Roman Symbols

A	Area	[m^2]
A_c	Contact area between effective heat transfer and visualization plate	[m^2]
A_{eff}	Effective heat transfer area	[m^2]
A_{fp}	Flow passage area	[m^2]
A_n	Amount of pixels in square area top window	[-]
AR	Aspect ratio	[-]
A,S	Top window square area	[m^2]
A_{wet}	Wetted area	[m^2]
c	Corrosion constant	[-]
C	Chisholm correlation constant	[-]
C_c	Coefficient of contraction	[-]
c_P	Specific heat capacity	[kJkg^{-1}K^{-1}]
d	Diameter	[m]
D	Bolt diameter	[m]
d_g	Channel gap	[m]
d_h	Hydraulic diameter	[m]
d_p	Plate thickness	[m]
D_p	Port diameter	[m]
ds	Maximum displacement	[m]
E	Square material matrix	[Pa]
f	Fanning friction factor	[-]
F	Load	[N]
f_{com}	Overall discharge coefficient for flow through orifice tubes	[-]
f_{edge}	Discharge coefficient for the sharp-edged orifice	[-]
f_{lam}	Friction factor for a smooth developing flow	[-]
g	Gravity constant	[kgs^{-2}]
G	Mass flux	[kgm^{-2}s^{-1}]
h	Enthalpy	[kJkg^{-1}]
I	Matrix containing average pixel values	[-]
I_m	Matrix containing summed pixel values	[-]
J	Jacobian	[-]
k_a	Strength reducing factor including stress distribution	[-]
k_e	Strength reducing factor including load direction	[-]
k_{mod}	Strength reducing factor including load duration	[-]
k_{sp}	Strength reducing factor including surface factors	[-]
L	Length	[m]
L_h	Port-to-port width	[m]
L_P	Effective length of plate	[m]

L_v	Port-to-port length	[m]
L_w	Effective width of flow	[m]
$\dot{m}$	Mass flow rate	[kgs^{-1}]
M	Magnification ratio	[-]
n	Number of measured data points	[-]
p	Corrugation pitch	[m]
P	Pressure	[Pa]
P_c	Condensation pressure	[Pa]
$\dot{Q}$	Heat transfer rate	[Js^{-1}]
S	Slip ratio	[-]
SF	Safety factor	[-]
T	Temperature	[K]
u	Velocity	[ms^{-1}]
U	Overall heat transfer coefficient	[Wm^{-2}K^{-1}]
V	Amount of pixels that represent void	[-]
w	Width	[m]
x	Vapor quality	[-]
X	Lockhart-Martinelli parameter	[-]
y	Data point value	[-]
$\hat{y}$	Correlation value	[-]
y_i	Height of image inside camera	[m]
y_o	Height of the object	[m]
z	Area conversion factor	[-]
Z_d	Matrix containing summed varied pixels	[-]
Z_{final}	Matrix containing final image	[-]

Subscripts

a	Ammonia
atm	Atmospheric
av	Average
$bend$	Bending
$circ$	Circumference
$clamp$	Clamping
de	Deceleration
ele	Elevation
env	Environment
exp	Experimental
f	Friction
$glass$	Glass material

hor	Horizontal
i	Inlet
in	Initial
$intern$	Internal
L	Liquid
LED	LED illumination source
max	Maximum
mix	Mixing
o	Outlet
ori	Orifice
P	Principle
$PMMA$	PMMA material
$port$	Port cross section
r	Rubber
red	Reduced
s	Stainless steel
SL	Superficial liquid
SV	Superficial vapor
t	Tensile
T	Torque
$tube$	Tube cross section
TP	Two-phase
V	Vapor
Val	Validated
VM	Von Mises
W	Water

Greek Symbols

α	Heat transfer coefficient	[$\mathrm{Wm^{-2}K^{-1}}$]
β	Chevron angle	[°]
ΔP	Pressure drop	[Pa]
Δs	Element size	[m]
Δt	Time span	[s]
Δx	Pixel height	[m]
ϵ	Volumetric void fraction	[-]
ϵ_A	Surface area void fraction	[-]
ϵ_s	Strain	[-]
$\epsilon_{A,S}$	Surface area void fraction of square area	[-]
ζ	Formula simplifying constant	[-]

η	Pixel value	[-]
κ	Thermal conductivity	[Wm^{-1}K^{-1}]
λ_{wave}	Corrugation wavelength	[m]
Λ	Fluid property modifying group	[-]
μ	Dynamic viscosity	[Pas]
μ_s	Friction factor	[-]
ν	Specific volume	[m^{3}kg^{-1}]
Π	Channel perimeter	[m]
ρ	Density	[kgm^{-3}]
σ	Surface tension	[Nm^{-1}]
Σ	Stress	[Pa]
τ	Torque	[Nm]
ϕ	Enhancement factor	[-]
Φ	Two-phase multiplier	[-]
ψ	Required frame rate	[s^{-1}]

1

Introduction

As the demand of renewable energy is increasing, the search beyond the more matured forms of renewable energy such as solar, wind and hydro energy becomes a necessity. One of these forms of new energy is Ocean Thermal Energy Conversion (OTEC), which is clean and has no emissions. Ocean energy has a huge potential but appears to be virtually unused[18]. The OTEC technology is especially interesting for islands where the land mass is limited, and the ocean's energy is in abundance. OTEC is a method to convert the thermal energy from the ocean into electricity.

1.1. OTEC-cycle

The water temperature remains quite constant in the areas of interest which means that the electricity generation by the OTEC-cycle is constant and stable. This is a big advantage as compared to other forms of renewable energy, since most of these techniques are dependent on intermittent sources such as wind and solar power. The ocean surface water is warmed up by the sun's radiation while the water at the bottom of the sea remains cold and constant. This creates a thermal energy potential which can be extracted by an OTEC cycle. The cycle operates with the principle of an organic Rankine cycle (ORC) or a Kalina cycle. Figure 1.1 shows a schematic representation of the OTEC principle where a hot water and cold water streams are used to extract energy from the ocean.

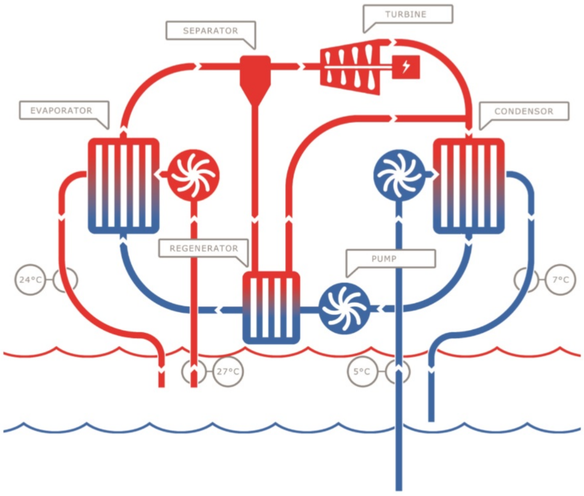

Figure 1.1: Schematic representation of the OTEC principle

The OTEC principle makes use of a turbine, an evaporator, a condenser and a recuperator (optional for ORC). The evaporator vaporizes the working fluid by using the warm ocean water available at the surface of the ocean as a hot source. In the condenser, the working fluid is condensed by using the in-depth cold water from the ocean. The vaporised fluid powers the turbine which produces electricity. An ORC uses a pure refrigerant, where a Kalina cycle uses a non-azeotropic mixture as the working fluid in the cycle. Due to a difference in boiling points, a part of the working fluid is evaporated while the rest remains a liquid. The liquid part of the working fluid is sent to a recuperator which pre-heats the working fluid right before entering the evaporator. Next, the liquid part enters the condenser where it mixes with the expanded vapor part that has been through the turbine. The separator can also be used for the ORC, where non-evaporated liquid is sent to the recuperator in order to prevent the turbine from damage. The recuperator serves as a pre-heater that is meant to increase the efficiency of the plant.

1.2. Working fluid

The maximum temperature of the warm sea water is usually between 25 – 30 °C. This warm water source is used to evaporate a working fluid, which means that the working fluid medium saturation temperature should be below this temperature. Commonly used working fluids for an OTEC cycle are therefore pure ammonia for the ORC configuration and highly concentrated ammonia diluted with water for the Kalina configuration. In this research, only pure ammonia is considered for the flow visualization study.

1.3. Bluerise B.V.

Bluerise is a company specialized in the application of ocean energy based in Delft. Bluerise specializes in OTEC, Seawater Air Conditioning (SWAC) technologies and related Deep Sea Water applications. Technology and development plans for implementations of OTEC and SWAC are provided by Bluerise as well as Ocean Eco parks that utilize the ocean resource by means of innovative technologies. Bluerise provides consulting and engineering services to governments, project developers and energy companies. In cooperation with the TU Delft, Bluerise has built a small scale 100 W OTEC plant located in the Energy & Process lab of TU Delft, which allows for research on the performance of the OTEC cycle. The 100 W OTEC demo consists of an organic Rankine cycle using ammonia as the working fluid that is downward condensed in a gasketed plate heat exchanger (GPHE). Projects are set up on several locations in the tropics to test the performance of an OTEC cycle on a larger scale. The first pilot projects in Jamaica and Curacao are close to realization.

1.4. Problem statement

The condenser that will be used in the full scale OTEC plant is a plate heat exchanger (PHE), which is the most common type of heat exchanger for this type of application. Countless studies report on the superior performance of PHEs, in relation to favourable heat transfer coefficients (HTCs), fluid distribution and general thermal effectiveness (Thulukkanam [46]). However, the two-phase behaviour inside the PHEs is yet not fully understood, resulting in over- or underestimating by several published heat transfer and pressure drop correlations, which are limited by the range of conditions they cover (Amalfi et al. [5]). For the full scale OTEC plant the cold water piping for the condenser will be one of the most costly parts. To properly predict the mass flow rate and thus the pipe diameter, it is important that simulations on the performance of the condenser are accurate.

A model was developed for the complete experimental setup of the OTEC cycle by Goudriaan [19] and Kuikhoven [30]. The heat exchangers were modelled using two phase heat transfer correlations developed specifically for plate heat exchangers, but the model did not predict the performance of the condenser well. For this reason, Geschiere [18] performed experiments on the brazed plate heat exchanger and Dahlgren [16] on the gasketed plate heat exchanger in the OTEC demo. Both developed new condenser models based on different principles for predicting the performance of the condensers. Geschiere [18] has adapted a falling film absorption model to the operating conditions of the brazed condenser of the Kalina OTEC cycle. This model allows for local prediction of heat and mass transfer for a film flow pattern. Dahlgren [16] generated a model for predicting the pressure drop and heat transfer performance inside the gasketed plate heat exchanger that does not include the flow pattern. Tao et al.[45] developed a general flow pattern map for PHEs by combining previous studies and translating the data from previous studies into dimensionless forms. This map can be used to predict the flow patterns in a PHE and the predicted flow pattern can be taken into account for modeling a condenser. These three researches form a first basis all containing different constructive elements necessary to form an improved detailed model of the GPHE that involves the occurring flow pattern and the dominant physical phenomena that play an important role in the two-phase behaviour inside the PHE. The missing link is the information of which flow patterns actually occur in the GPHE and what are the dominant physical phenomena that influence the flow configuration, heat transfer and pressure drop.

1.5. Research objective

The flow pattern is expected to have an influence on the performance of the heat exchanger and better predictions of the flow patterns in PHEs are expected to improve the calculation of heat transfer and pressure drop (Tao et al. [45]). There is a lack of available literature on condensing ammonia in PHEs and the relation between the PHE performance and the flow patterns inside the channel. Insight on the relations between flow patterns, physical phenomena that influence the flow patterns, HTCs and pressure drop for condensing ammonia is expected to be valuable for optimizing condenser models. The latter explains the necessity for flow visualisation experiments in PHEs.

The goal in this research is to identify the flow patterns that occur in the GPHE, gain more knowledge on the dominant physical phenomena and how they relate to the performance. A visualization section including a transparent plate is designed in the OTEC demo that allows for flow visualization. Flow visualization experiments are performed on the GPHE for a single-channel configuration to identify the flow patterns and how they relate to the performance of the GPHE. Second, multi-channel experiments without visualization are performed to investigate the performance of the GPHE for a multi-channel configuration, and predict which flow patterns occur for these experimental conditions. The objective of this study is answering the main research question and sub-questions (indicated by the roman numbers), defined below:

Main research question: 'Which flow patterns are dominant inside the gasketed plate heat exchanger condenser of the OTEC demo and how do they relate to its performance?'

(i) How are flow patterns identified by previous studies and is there a consistency in the classifications of the flow patterns?

(ii) Which visualization plate material is suitable for the OTEC demo conditions to enable visualization?

(iii) Which flow patterns are identified during the single-channel visualization experiments?

(iv) How are the occurring flow patterns related to heat transfer and pressure drop in the GPHE?

(v) Which physical phenomena play a dominant role in the transition between the flow patterns?

(vi) Do the observed flow patterns match the proposed flow pattern maps by previous studies for the experimental conditions of the visualization experiments?

(vii) Based on the experimental conditions, pressure drop and calculated HTCs of the multi-channel experiments, which flow patterns are expected to occur for multiple channel configurations in the GPHE?

1.6. Experimental setup

The OTEC experimental setup of 100 W is an advanced organic Rankine OTEC cycle. The warm and cold seawater streams are represented by tap water reservoirs that are kept in two bassins. The condenser investigated in this research is an TL3BFG10 GPHE by Alfa Laval that is used to condense the downward ammonia flow that acts as the working fluid in the OTEC cycle. The current heat exchanger configuration consists of 1 corrugated stainless steel heat transfer plate, a transparent polymer visualization plate and two outer pressure plates. The OTEC demo allows for flow visualization, recording of the flow configurations/regimes by use of a high speed camera and storing the sensor data of the experimental conditions. The experimental setup is the main tool used for answering the main research question and the related sub-questions.

1.7. Thesis outline

The research in this report consists of a literature review, material research, flow visualization experiments and analysis. Chapter 2 reviews flow patterns identified by previous studies and their classifications, answering sub-question (i). Chapter 3 gives a detailed explanation on the experimental configuration and what preparations were necessary to make a substantiated choice for illumination and type of camera. Extensive material research is performed in chapter 4 to find the right material for the visualization plate, answering sub-question (ii). Various production methods and materials are compared, while testing the materials on its chemical resistance to ammonia. Chapter 5 reveals the approach for the visualization experiments and multi-channel experiments first. The observed flow patterns and flow paths are explained, answering sub-question (iii). Next, the processed data and results are presented for the visualization experiments and compared to the identified flow patterns, answering sub-question (iv) , (v) and (vi). The data of the multi-channel experiments is analysed and compared to the data of the single-channel visualization experiments. Predictions are made about the occurring flow patterns for the multi-channel configurations, answering sub-question (vii). Finally, chapter 6 answers the main research question and sub-questions in a summary. Conclusions are drawn on the occurring flow paths, flow patterns and dominant physical phenomena playing a role in the flow configuration. A discussion is given at last that elaborates on assumptions made and likely errors in the calculations and findings. A conference paper is written for the 25th IIR international congress of refrigeration 2019 containing the results of the visualisation experiments and is attached in Appendix A of this report.

2

Literature review

In the literature review topics relevant for the current research are presented and discussed. Previous studies on flow patterns, flow pattern maps and its relations to heat transfer are summarized. The fluid property modifying parameter is introduced, as well as relevant dimensionless numbers and other influential factors that determine the transition between flow patterns. The possible involvement of surface tension into the flow pattern and heat transfer is discussed. Flow patterns are recognized in previous studies but the classification of the flow pattern seems subjective. For this reason, a comparison is performed on the classified flow patterns by various studies that involve air/water, refrigerants and ammonia. Based on this, a flow pattern classification by a schematic representation of the various flow patterns is proposed. This is used to identify the flow patterns in a consistent way during the visualization experiments of this study. At last, a summary is presented of various experimental setups for flow visualization, as the choice for recording and illumination during the experiments needs to be decided upon.

2.1. Flow patterns and related phenomena

In this section, flow patterns are introduced and the factors influencing the transition between the flow patterns are summarized. Factors that influence the heat transfer are evaluated and related to the flow patterns.

2.1.1. Flow patterns & flow pattern maps

A clear understanding of the momentum, heat and mass transfer rates involved in two-phase flow is essential for an optimal design and operation of heat transfer equipment. One of the difficulties in dealing with multi-phase flow is that the momentum, heat and mass transfer rates can be sensitive to the geometric distribution of components inside the flow. Most of the earlier investigations were concerned with arriving at workable correlations for pressure drop or for estimating heat fluxes. Little or no attention has been paid to flow pattern maps and how they relate to varying conditions. Tao et al. [45] proposed a phenomenological description of the geometric distributions or flow patterns that are observed in multi-phase flows that occur in plate heat exchangers. During the condensation of the working fluid in the condenser, multiple flow patterns might occur. Figure 2.1 shows the four main flow patterns observed for a downward two-phase flow in condensers. The sequence is generally based on the occurrence of flow patterns when the mass flux of the vapor is increased. The mass flux is defined as the rate of mass flow per unit area. In the ammonia channel of the GPHE, $G = \dot{m}_a {A_{fp}}^{-1}$ $\text{kgm}^{-2}\text{s}^{-1}$. Flow patterns are determined visually by an experimental setup where the flow is recorded through a transparent plate. A description of the various flow patterns is proposed by Tao et al. [45]:

1. *Bubbly flow*
   When the flow consists of a continuous liquid phase that contains a large amount of small gas bubbles, the flow is referred to as bubbly flow. This flow can be divided into regular and irregular bubbly flow. For regular flow, the bubbles are even sized with spherical shape. When the gas mass flux is increased, the flow transforms from regular into irregular. The bubbles vary in size and shape.

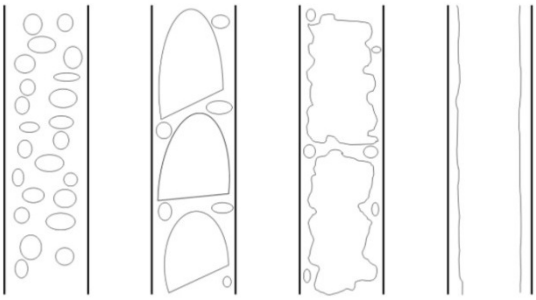

Figure 2.1: Schematic representations of the main flow patterns for downward two-phase flow in plate heat exchangers by Tao et al. [45]. From left to right: bubbly flow, slug flow, churn flow and film flow.

2. *Slug flow*
   When the gas bubbles are regularly shaped but grow to the same dimensions as the main channel, the flow is referred to as slug flow. The flow becomes intermittent due to the slugs which are formed due to coalescence of the smaller bubbles. The slugs have a characteristic shape and resemble a bullet with a hemispherical nose and a blunt tail. Some small bubbles still might be present in the flow.
3. *Churn flow*
   For churn flow, large vapor pockets become wavy and irregular. It is generally accepted that churn flow is the chaotic version of slug flow. This is because the amount of liquid between the large bubbles is too little to form stable liquid zones. Small bubbles might occur in between the vapor pockets.
4. *Film flow*
   For film flow, a continuous liquid films cover the walls of the channel. Between the liquid films, vapor remains a continuous bulk flow. However, as the amount of vapor increases, the limited liquid film is unable to wet the entire surface which causes parts of the surface to dry out. A film flow that includes dry surfaces on the heat transfer plate is classified as partial film flow.

A flow pattern map describes graphically for which combination of parameters a certain flow pattern occurs and helps distinguish the various regimes. The construction of a flow pattern map can be useful to gain some insight in which flow patterns occur on the inside of an apparatus, which is generally unknown. Different characteristics can be used on the axes to construct a flow pattern map. Generally, previous visualization studies show that for various types of heat exchangers the mass flux G has a large influence on the transition between flow patterns. Vlasiogannis et al. [51] conclude for vertical downward air-water flow in a corrugated PHE that a large ratio of superficial gas velocity over liquid velocity a film flow appears. A reversed ratio gives a bubbly flow, and a ratio equal to 1 gives either slug or churn flow. Oshinowo and Charles [39] investigated air/water flow in tubes and also conclude that for increasing gas mass flux a film flow is observed and a low mass flux shows a bubbly flow. The vapor quality x is defined as the mass fraction in a saturated mixture that is vapour, and also shows to have a significant influence on the transition between flow patterns. Al-Zaidi et al.[3] show for downward HFE-7100 flow in horizontal tubes that for a high vapor quality film flow is mostly seen. A very low quality shows bubbly flow and, in between, slug flow sometimes appears. Arima et al.[6] find for a vertical flat plate and upward evaporation of ammonia that a low vapor quality gives bubbly flow, and a high vapor quality shows a film flow. For a plate heat exchanger, it is expected that film flow is most advantageous in terms of heat transfer between the fluids inside the exchanger.

Figure 2.2 shows an example of a flow pattern map which contains the described flow patterns. In this case, the two-phase Froude number Fr_{TP}, the liquid Reynolds number Re_L and the fluid property modifying parameter Λ are used to graphically describe the different flow patterns occurring in two-phase downward flow in PHEs. These parameters are dimensionless numbers and introduced in subsection 2.1.4.

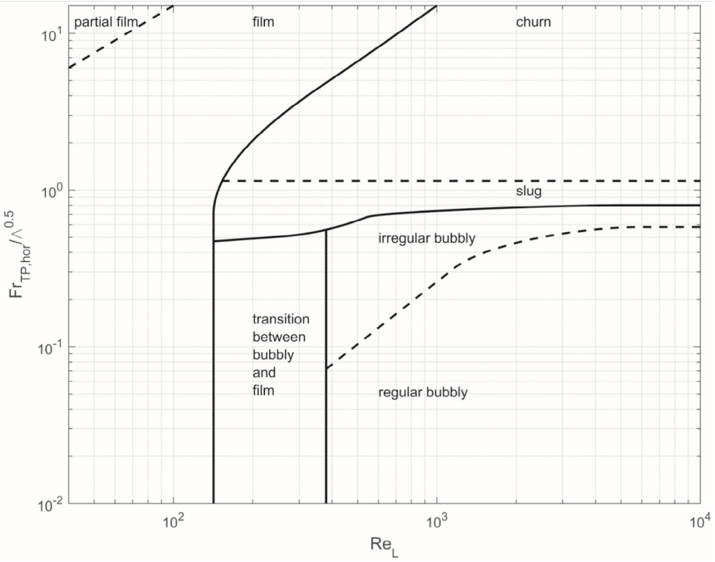

Figure 2.2: Simplified two-phase flow pattern map for PHEs including the liquid Reynolds number Re_L, the two-phase Froude number Fr_{TP} and the fluid property modifying parameter Λ

2.1.2. Condensation mechanisms

Tao et al. [45] investigated the effects on the transition of condensation mechanisms when variations of mass flux and vapor quality are considered. The heat transfer performance is sensitive to condensation mechanisms. According to Tao et al. it is widely accepted that condensation within plate heat exchangers can be classified as either gravity controlled or convection controlled. It is expected that flow patterns are associated with the condensation regimes.

Gravity-controlled and convection-controlled condensation
In the gravity controlled condensation regime, the HTCs decrease with increasing mass flux or stay almost constant (Tao et al. [45]). At small mass flux, condensation is mainly governed by gravity. Interfacial shear stress has a negligible effect on the flow.

The convective condensation regime is referred to as turbulent, shear dominated condensation. In this regime the HTCs increase with increasing mass flux (Tao et al. [45]). Convective condensation appears at larger mass flux and is dominated by interfacial shear. The interfacial shear reduces the thickness of the condensate film and promotes turbulence in the condensate film. The reduced thickness of the condensate film reduces the thermal resistance of convective heat transfer, while the promoted turbulence in the film adds to the heat transfer.

Transition regime
There is also a transition regime where both gravity and shear are non-negligible. In this regime the HTCs stay constant for a while even when the mass flux is increased. According to Tao et al.[45] this constant regime of HTCs suggests the combined effects of gravity and interfacial shear. To determine in which region the flow is in, the equivalent Reynolds number for two-phase flow is introduced in the study by Akers et al.[1], see Equation 2.1.

$$Re_{eq} = \frac{G\left[(1-x) + x\left(\frac{\rho_L}{\rho_V}\right)^{0.5}\right] d_h}{\mu_L} \tag{2.1}$$

For different types of both Hydrofluorocarbons (HFC's) and hydrocarbons investigated by Longo [33],[34] the transition value is at 1650 for the Reynolds equivalent number. The exact transition mass flux values are different among several researches and are affected by refrigerant properties and plate heat exchanger geometries (Tao et al. [45]). Mass flux is the main contributor to the transition from gravity-controlled condensation to convective condensation. It is expected that film flow corresponds to the forced convective region, where the HTCs are largest.

2.1.3. Incluences on heat transfer and HTCs

Vlasiogannis et al.[51] conclude that the heat transfer increases by increasing superficial liquid velocity and that air always has a positive effect on the HTC, i.e. measured values are higher than those for corresponding water flow rate without air. Al-Zaidi et al.[3] conclude that increasing the mass flow rate corresponds to an increase of the local condensation HTC. Arima et al.[6][7] also conclude that for an ammonia-water mixture the local HTCs increase with an increase in the mass flux but for pure ammonia the local boiling HTC is hardly affected by the mass flux. It is therefore expected in the visualization experiments in this thesis, the HTCs increase with mass flux.

Al-Zaidi et al.[3] conclude from the experiments that a high vapor quality gives the highest local condensation HTC. Arima et al.[7] spotted large voids for the ammonia-water mixture for high vapor fractions and concludes that this reduces the heat transfer. Arima et al.[6] show that the local HTC increases for increasing vapor quality but drops when the vapor quality increases above a value of 0.8. It is expected that HTCs increase with increasing vapor quality. However, when dry-out occurs on the surface area of the plate (i.e. partial film flow), it is expected that the HTCs decay.

Vlasiogannis et al.[51] conclude that film flow shows particularly favourable heat transfer enhancement in comparison to other flow patterns. Arima et al.[7] investigated the influence of the mass flux in reference to the relation between the flow pattern and HTC for a water/ammonia mixture. It appeared that for larger mass flux the HTC increased. It was considered that this was because of the difference in the thermal resistance by the flow pattern and the difference in the ammonia mass fraction of the liquid phase on the heated surface. Al-Zaidi et al.[3] compared condensation flow patterns to the local condensation HTC and concluded that for film flow the HTC was largest. When the fluid enters the condenser, the flow pattern is in the film flow regime and the local HTC is high. The local heat HTC decreases with decreasing local vapor quality due to the condensation process along the channel. This is due to the thickening of the liquid film and reduced vapor flow leading to higher fluid thermal resistance. For the visualization experiment, it is expected that the HTCs increase with increasing mass flux and vapor quality, and that the maximum HTC values are reached for film flow. However, when partial film flow occurs, it is expected that the HTCs drop.

2.1.4. Relevant dimensionless numbers

Tao et al. [45] suggested relevant dimensionless numbers for flow patterns. Flow patterns are affected by interaction of forces and fluid properties, which are represented by these dimensionless numbers. Dimensionless numbers can be used to classify a flow into a certain regime or to determine which phenomenon is dominant under certain conditions. If a dimensionless number is very large the force represented by the numerator is dominant over the force represented by the denominator. It can therefore be decided to neglect the force in the denominator and vice versa. In this way, it can be determined for a certain flow pattern which phenomena are dominant and which can be neglected.

Reynolds number
The Reynolds number Re is the ratio of inertial forces over viscous forces. The Reynolds number is used to classify the flow into a laminar or turbulent flow and is given by:

$$Re = \frac{Gd_h}{\mu} \tag{2.2}$$

The liquid Reynolds number Re_L describes in a two-phase flow only the liquid entrainment in the Reynolds number:

$$Re_{LO} = \frac{G(1-x)d_h}{\mu_L} \tag{2.3}$$

The Reynolds equivalent number Re_{eq} describes both phases in a two-phase flow including the vapor fraction and a mass flux:

$$Re_{eq} = \frac{G_{eq} d_h}{\mu_L} \tag{2.4}$$

Where $G_{eq} = G x_{eq}$ and $x_{eq} = [(1-x) + x(\frac{\rho_L}{\rho_V})^{0.5}]$.

Prandtl number
The Prandtl number Pr is a dimensionless number which is defined as the ratio of the viscous diffusion rate over the thermal diffusion rate of a fluid. It is often used in determining the convective HTC. It is given by:

$$Pr = c_p \frac{\mu}{\kappa} \tag{2.5}$$

Froude number
The Froude number is the ratio of inertia to gravity and is expected to play a role in vertical plate heat exchangers (Tao et al.[45]). The two-phase Froude number Fr_{TP} for two-phase flows used by Stephan et al.[43] is given by:

$$Fr_{TP} = \frac{xG}{g d_h \rho_V \left(\rho_L - \rho_V\right)^{0.5}} \tag{2.6}$$

Weber number
The Weber number We is the ratio of inertia to surface tension and might play a role for flow patterns, which is given by Stephan et al.[43]:

$$We = \frac{\rho u^2 d_h}{\sigma} \tag{2.7}$$

Bond number
The Bond number Bd is the ratio of gravity to surface tension, and is expected to be non-negligible at low mass flux (Bergman et al. [22]):

$$Bd = \frac{\left(\rho_L - \rho_V\right) g d_h^2}{\sigma} \tag{2.8}$$

Galileo number
The Galileo number is the ratio of gravitational force over viscous force and is used for condensing flows. It is expected that for wavy films the liquid wants to fall down because of gravity but viscous forces prevent this (Geschiere [18]).

$$Ga = \frac{\rho_L \left(\rho_L - \rho_V\right) g d_h^3}{\left(\mu_L\right)^2} \tag{2.9}$$

Fluid property modifying parameter
A fluid property modifying group Λ was defined as a function of the liquid properties relative to those of water under the same conditions:

$$\Lambda = \frac{\frac{\mu_L}{\mu_W}}{\left(\frac{\rho_L}{\rho_W}\left(\frac{\sigma_L}{\sigma_W}\right)^3\right)^{\frac{1}{4}}} \tag{2.10}$$

Tao et al. [45] created flow pattern maps for two-phase vertical downward flow in plate heat exchangers including the fluid property modifying group. Tao et al. made a qualitative comparison between flow patterns and constructed a combined flow pattern map to include fluid properties, see Figure 2.2.

2.1.5. The effect of surface tension

Molecules in fluid feel a mutual attraction. A molecule in a bulk fluid is surrounded by attractive neighbours, while a molecule at the surface has less neighbours and is in an energetically unfavourable state. Creating a new surface is energetically costly, and a fluid will therefore minimize its surface areas by forming spherical shapes. A molecule at a free surface will lose half of its cohesive energy relative to molecules in the bulk. Surface tension is a direct measure of this energy loss per unit area of surface and acts only at the free surface [9].

Alshqirate et al.[4] carried out an experimental and analytical investigation on small-sized tubes (with a diameter of 0.6, 1.0, and 1.6 mm) to show the effect of surface tension on the HTCs of gas flow inside tube heat exchangers during the condensation process. The results showed that the predicted HTCs of the proposed correlation was closer to the experimental results than any other correlation, a finding related to the consideration of the surface tension. Alshqirate et al. suggest that surface tension influences the two-phase flow characteristics and that it appears as the main parameter that affects the two-phase convective HTC expressed by the Nusselt number.

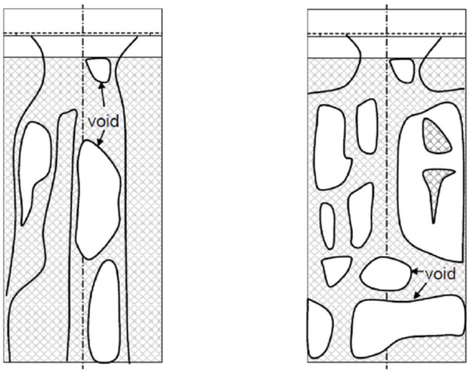

Figure 2.3: schematic representation of observed dry surface voids on the plate of a heat exchanger, by Kim[28]

Another factor that is expected to play a role on the heat transfer is the surface tension contributing to void formation on the plate during condensation, as mentioned by Geschiere [18]. When the surface tension increases the liquid wants to agglomerate and not spread out over the wall surface (Kim [28]). Kim and Arima et al. [6] suggest that this maldistribution is of negative influence on the HTC. Especially when using low Reynolds numbers a lot of dry surface voids were observed in the flow shown in Figure 2.3. Dry surface voids are expected to occur in the liquid film with increasing vapor quality. Ammonia is known for its good wettability properties due to low values of the surface tension (Zhang et al. [58]). A correction factor taking into account the influence of the flow pattern on the heat transfer performance was developed by Kim [28]. This correction is solely dependent on the Reynolds number and needs to be refitted for every situation:

$$\frac{A_{wet}}{A_{eff}} = bRe^{0.58} \tag{2.11}$$

The wettability for water and water/octanol are compared to the film Nusselt number, and a clear buckle in the Nusselt number plot is seen for an increasing film Reynolds number, see Figure 2.4. It is believed that the behavior of the Nusselt numbers in Figure 2.4 was due to incomplete wetting of the heat transfer surface [28].

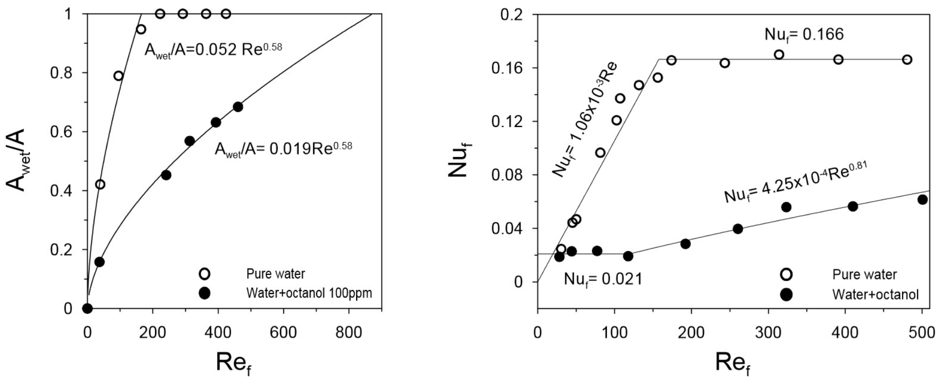

Figure 2.4: Fitted correlations for wettability and film Nusselt number, by Kim[28]

2.2. Previous experimental research on flow pattern maps

This section explains flow pattern classification by previous studies and maps which flow patterns were classified for certain flow configurations. The images of flows are compared to the flow pattern classifications to form an idea of the level of subjectivity. Second, a frontal view flow pattern classification is created for the visualization experiments in this research. At last, an overview is presented of the illumination methods and recording equipment. This helps determine which equipment is necessary for the visualization experiments.

2.2.1. Flow pattern classification

Flow patterns are defined visually. In the past, research is done on determining flow patterns inside experimental setups such as PHEs and tube heat exchangers. How the different flow patterns are recognized inside different experimental setups will help distinguishing those inside the OTEC GPHE. In each of the studies presented in Table 2.1 the flow is visualized by a transparent plate or window.

Table 2.1: Several flow visualization studies

Ref. nr	*Study*	*Type of working fluid*	*Type of equipment*	*Direction of flow*
1	Vlasiogannis et al. [51]	Air/water	Corrugated PHE	Vertical downward
2	Tribbe & Müller-Steinhagen [48][49]	Air/water	Corrugated PHE	Vertical downward
3	Nilpueng & Wongwises [38]	Air/water	Corrugated PHE	Vertical downward
4	Arima et al. [7]	Ammonia	Flat PHE	Vertical upward
5	Arima et al. [6]	Ammonia/water	Flat PHE	Vertical upward
6	Grabenstein et al [20]	Air/water	Corrugated PHE	Vertical downward
7	Winkelmann [56]	Air/water	Corrugated PHE	Vertical downward
8	Jassim et al.[26]	R134a	Corrugated PHE	Vertical upward

1. Bubbly flow
   Air/water-mixture: Vlasiogannis et al.[51] conclude that the bubbly regimes give a blurry image. The absence of bright regions indicate a continuous gas phase and therefore it is concluded that the air is dispersed in the form of small bubbles inside a liquid-continuous stream that covers the entire channel space, see Figure 2.5. The images made by Tribbe & Müller-Steinhagen [49] show both regular bubbly flow and irregular bubbly flow, where the regular bubbly flow shows a similar bubble shape and size while the irregular bubbly flow shows various gas bubbles size. Again, the gas bubbles show a clear image as compared to the liquid. Nilpueng & Wongwises [38] show an image where most gas bubbles reflect light where the liquid remains a bit blurry. Grabenstein[20] shows very small air bubbles in an air-water mixture in a 'diamond-grid'-like shape where the water remains in the core, similar to what can be seen in the images made by Vlasiogannis and Tribbe & Müller-Steinhagen. Winkelmann[56] recognizes bubbly flow as a large liquid film with some bubbles present in the flow, see Figure 2.6.

   Pure ammonia: An irregular bubbly flow is recognized on a flat plate by Arima et al.[6] with small liquid

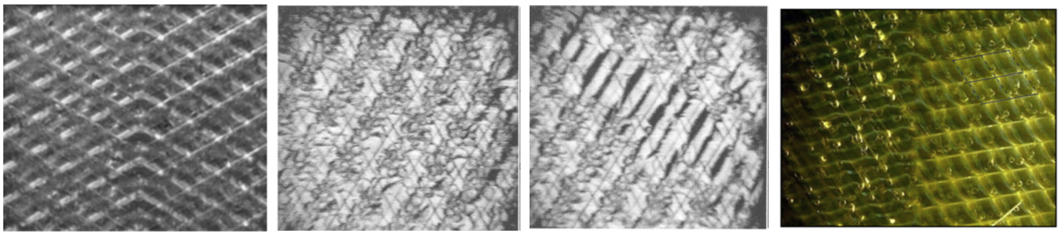

Figure 2.5: From left to right: Vlasiogannis et al.[51] (bubbly flow), Tribbe & Müller-Steinhagen[49] (regular bubbly flow), Tribbe & Müller-Steinhagen[49] (irregular bubbly flow), Nilpueng & Wongwises[38] (bubbly flow)

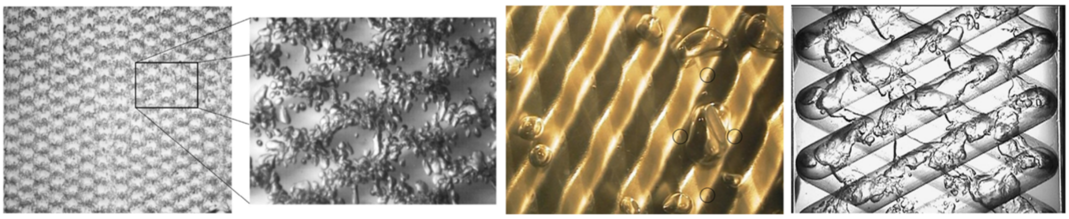

Figure 2.6: From left to right: Grabenstein[20] (bubbly flow and its close up), Winkelmann[56] (bubbly flow), Jassim et al.[26] (bubbly flow)

pockets being present in a continuous vapor flow. This is seen for a low vapor fraction of 0.28, see Figure 2.7. *Water/ammonia mixture*: Arima et al.[7] found irregular bubbly flow on a flat plate for an ammonia concentration of 80% and a vapor fraction of 0.4, see Figure 2.7. *R134a*: Jassim et al. recognized bubbly flow for R134a for low quality ranges where vapor bubbles are moving within the fluid, see Figure 2.6. Jassim et al. mention that this flow can also be considered as slug or churn flow, but still classify it as bubbly flow because they concluded it represents the flow pattern best when looking at the entire heat exchanger instead of individual channels.

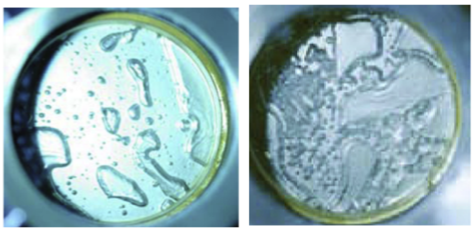

Figure 2.7: Left) Arima et al.[6] (bubbly flow). Right) Arima et al.[7] (bubbly flow)

2. Slug flow
   Water/air mixture: Vlasiogannis et al.[51] recognize the gas bubbles by a rather sharp front, which extends over the entire width of the channel and separates a liquid continuous region from a preceding gas continuous region. The slug fronts are horizontal or slightly inclined. Vlasiogannis et al. indicate that at lower water flow rates, slugs extend over a few corrugation wavelengths and appear as blurry ribbons. Nilpueng & Wongwises [38] also identified slug flow where alternating full water flow and air flow in the flow channel are present, see Figure 2.8. In Figure 2.8 a slug flow is detected by Grabenstein[20] when the liquid load is increased and is recognized by the large bubble shape covering the centre of the image. *Pure ammonia*: Arima et al.[6] determined the pattern in Figure 2.8 as slug flow for a vapor quality of 0.4 on a flat plate. The pattern looks calmer as compared to the bubbly flow from the same experiment. *Water-ammonia mixture*: Arima et al.[7] show a combination of slug and film flow in Figure 2.8 with an ammonia concentration of 80% and a vapor quality of 0.26.

3. Churn flow
   Water/air mixture: Vlasiogannis et al.[51] show that for churn flow, there are either liquid pockets in a gas-continuous flow or gas pockets in a liquid-continuous flow. The liquid is recognized by a blurry

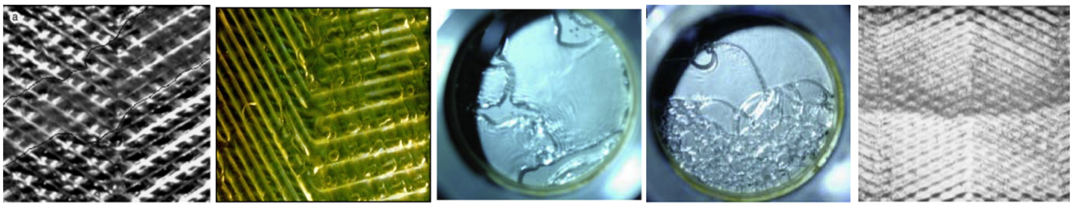

Figure 2.8: From left to right: Vlasiogannis et al.[51] (slug flow), Nilpueng & Wongwises [38] (slug flow), Arima et al.[6] (slug flow), Arima et al.[7], Grabenstein et al. [20] (slug flow)

view, while the gas gives a clear image on the picture. The black line is added to the figure by Vlasiogannis to make the distinction clear. Tribbe & Müller-Steinhagen[49] show a very blurry view for an image where they determined churn flow which could be easily mistaken for bubbly flow, see Figure 2.9. Winkelmann[56] recognizes churn flow and characterizes the flow by swarms of tiny bubbles rushing in waves of sweeping motion at velocities much higher than the velocity of the rest of the liquid. *Pure ammonia*: Arima et al.[6] found churn flow for a vapor quality of 0.4, where the figure shows both small and large liquid pockets in a gas flow. The flow is less calm than the slug flow.

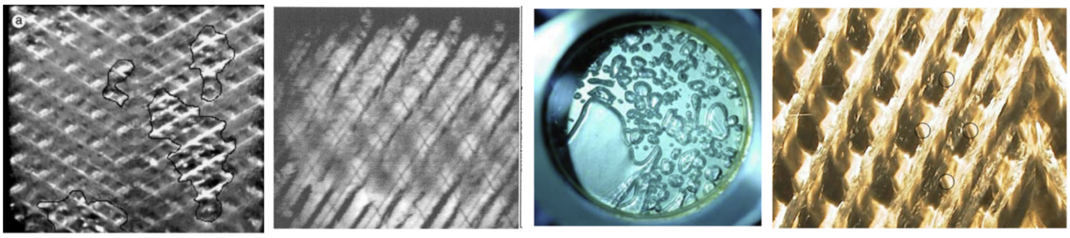

Figure 2.9: From left to right: Vlasiogannis et al.[51] (churn flow), Tribbe& Müller-Steinhagen[49] (churn flow), Arima et al.[6] (churn flow), Winkelmann[56] (churn flow)

4. Film flow
   Water/air mixture: Vlasiogannis et al.[51] noticed for film flow that it has a wide range of gas flow rates in which it occurs, see Figure 2.10. The image shows similar pattern as bubbly flow but has a clear image instead of blurry. Tribbe & Müller-Steinhagen[49] show also a very clear picture where the corrugations are clearly visible on the picture. The same holds for Nilpueng & Wongwises[38], where a clear image is shown over the corrugated plate, see Figure 2.10. Winkelmann[56] recognizes film flow and concludes that this flow is characterized by liquid that follows the orientation of the corrugations of the plate. *Pure ammonia*: A film flow is recognized by Arima et al.[6] with a clear liquid film covering the entire visualized area. This is for a vapor fraction of 0.63, see Figure 2.11. *Water/ammonia mixture*: Arima et al.[7] show two images of film flow for different vapor fractions at an ammonia concentration of 80%. Again, a smooth liquid film is shown which indicates the film flow, see Figure 2.11. *R134a*: Jassim et al.[26] classify both a rough film flow and a smooth film flow for the refrigerant, see Figure 2.11. The transition from rough film flow to smooth film flow takes place with increasing vapor quality while keeping the mass flux constant.

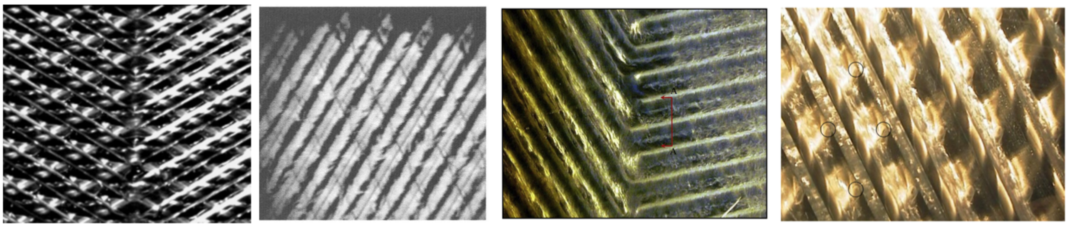

Figure 2.10: From left to right: Vlasiogannis[51] (film flow), Tribbe & Müller-Steinhagen[49] (film flow), Nilpueng & Wongwises[38] (film flow), Winkelmann[56] (film flow)

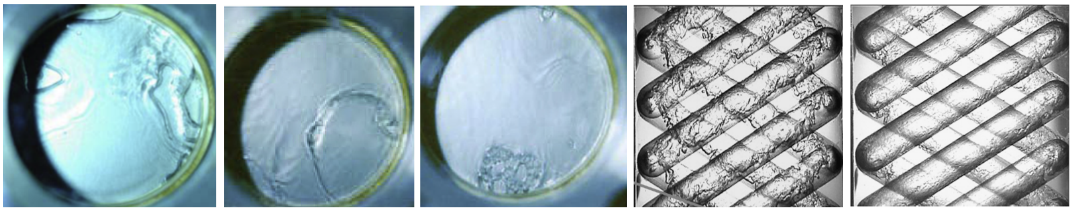

Figure 2.11: From left to right: Arima et al.[6] (film flow), Arima et al.[7] vapor quality of 0.4 (film flow), Arima et al.[7] vapor quality of 0.66 (film flow), Jassim et al.[26] (rough film flow), Jassim et al.[26] (smooth film flow)

Proposal of frontal view flow pattern classification

As Tao et al. [45] already concluded, the subjectivity of observations affects the determination of flow patterns and their transitions in three ways. The flow patterns in plate heat exchangers are not clearly defined and the description is not consistent. The judgement of flow patterns depends on researchers and the quality of the images taken from the experimental setup. In multiple researches it is concluded that churn and slug flow are most difficult to distinguish. Second, irregular bubbly flow can also simply be mistaken with churn or slug flow, therefor it is decided not to include the term irregular bubbly flow in the research. Tao et al. [45] made a schematic representation of the different flow patterns from a side perspective of the flow in the channel, see Figure 2.1. However, since the visualization experiments will be performed from the frontal side of the channel, a new schematic representation of the flow patterns is developed in this research to classify the flow patterns during experimenting for this study, see Figure 2.12. The black lines represent the corrugations from the stainless steel plate and the transparent plate. The blurry dark grey surface represents the liquid covering the surface, where the lighter grey pockets represent downward flowing vapor bubbles. When the surface is covered with liquid, the yellow lines represent reflections from lighting. In the bubbly flow pattern regime, many small bubbles are expected. Slug flow is classified by large horizontal vapor pockets in the liquid flow covering the entire width of the plate. Churn flow is less calm than slug flow and contains randomly sized and randomly located vapor pockets inside the liquid. Film flow is classified by an undisturbed view representing the liquid covering the plate entirely.

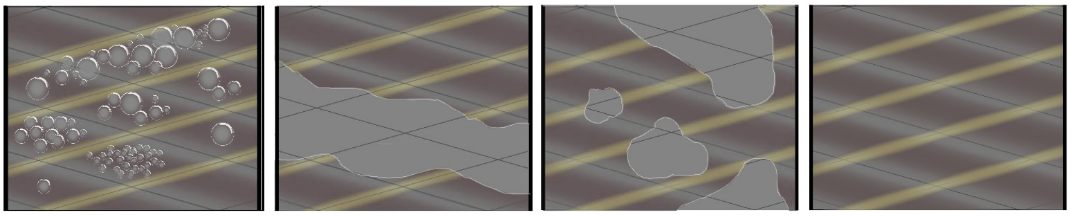

Figure 2.12: Schematic representation of the flow patterns seen from a frontal perspective. From left to right: Bubbly flow, slug flow, churn flow, film flow

2.2.2. Experimental configurations used in previous studies

Dahlgren[16] reviewed previous visualization studies on heat exchangers. Table 2.2 gives an overview of several visualization studies and what configuration they use. Grabenstein et al. [20] used a single gap and two transparent plates for the visualization study. The camera is positioned in front of the setup while the lighting is positioned at the backside. Jassim et al.[26] used a stroboscope for illumination. The stroboscope was placed behind the transparent plates and reflected light on a white background. According to Jassim et al., the optimal frequency for proper exposure was found to be 4800 flashes per minute. Vlasiogannis et al.[51] use UV lighting as an illumination source. A fluorescent dye is added to the two-phase mixture and is irradiated by UV-light.

Al-Zaidi et al. [3] uses a microscope that provides the illumination for the camera to record the flow patterns. Grooten et al. use a halogen light behind tissue paper to ensure diffuse light for clear visualizations. Arima et al.[6],[7] use a 250 W cold lamp but do not mention a position or angle with respect to the visualisation section. Tribbe & Müller-Steinhagen [48] create images by light-refraction. Nilpueng & Wongwises [38], D. Oshinowo et al.[39] and D. Winkelmann [56] do not mention the use of a lighting source. General problems

Table 2.2: Overview of several visualization methods, by Dahlgren [16]

Author	*Work. Fluid*	*Channels*	*Visualization method*	*Transp. Material*	*Lighting*	*Camera*
Grabenstein et al.[20]	Air/water R365	1	Corrugated gap, side view	Polyur-ethane	Halogen headlights	
Arima et al. et al. [6][7]	NH_3/water	1	Sight glasses	Glass	250 [W] cold lamp	Pentax *istD
Winkelmann [56]	Air/water	1	One transparent end plate, hole in frame	Plastic	From the front	High speed video camera (500 fps)
Nilpueng & Wongwises [38]	Air/water	1	One transparent end plate, two windows	Polyurethane		Samsung Digimax v3
Jassim et al. [26]	R134a	1	Three types of transparent plates	PVC	Stroboscope	Digital
Asano et al. [8]	Air/water	Single/multi	Neutron radiography			
Vlasiogannis et al. [51]	Air/water	6	Transparent end covers	Plexiglass	UV- and visible light	REdlake Motion scope PCI high-speed
Tribbe & Muller Steinhagen [49]	Air/water	1	Transparent end covers	Polyester	Light refraction	Kodak Ektapro 4340 high-speed

that occur by using frontal illumination is the light reflection that disturb the images. Therefore, in the visualization experiments in this study, a LED-strip is tried for illumination to prevent light refraction.

2.3. Summary

The flow configurations of a condensing flow are classified into four flow patterns: Bubbly, churn, slug and film flow. All four are expected to occur under varying experimental conditions and have specific flow configurations. It is expected that the different flow patterns have different heat transfer and pressure drop.

HTCs behave different with respect to condensation regimes. Therefore, it is important to identify in which condensation regime the flow is in during the visualization experiments.

HTCs are highest for film flow, and lowest for bubbly flow. HTCs are increased with vapor quality and mass flux when in the convective condensation regime. This makes sense as for high vapor quality and mass flux a film flow occurs.

Dimensionless numbers can be used to identify the dominant physical phenomena occurring in the flow and will be used in this research to eliminate or identify the relevant phenomena for the flow patterns observed.

Surface tension influences the occurrence of surface area voids on the heat transfer plates. This especially occurs for working fluids with a high surface tension, for experimental conditions with high vapor qualities and low mass fluxes. It is expected that this has a negative influence on the HTCs, and should be further analysed if partial film flow occurs in the visualization experiments.

A frontal view schematic flow pattern classification is constructed and presented in Figure 2.12. This classification will help identify the flow patterns in a consistent way and matches the general observations made in the previous studies.

Generally, strong illumination sources are used for visualization. A problem that occurs for frontal illumination is the reflections that disturb the images made by the camera. For this reason, a LED-strip is tested as a illumination source as it eliminates the problem of reflections.

3

Experimental setup

The experimental setup is a small scale OTEC cycle prototype (OTEC-Demo) located at the laboratory inside the Energy & Process department, TU Delft. This chapter explains the working principle of the OTEC cycle, the relevant components and the test section for flow visualization.

3.1. OTEC-Demo experimental setup

In cooperation with the TU Delft, Bluerise B.V. has developed a small-scale OTEC-plant. In the future, the knowledge gained from the experiments done on the demo will be used to scale up the design for large-scale OTEC-plants. A distinction can be made between a Kalina cycle and an ORC. The OTEC-demo is able to function as a Kalina cycle when the working fluid inside the cycle is an ammonia-water mixture, and as an ORC when ammonia is used as a pure fluid. In this study, only flow visualization on pure ammonia is performed, i.e. only the ORC cycle is used.

3.1.1. Organic Rankine cycle

An ORC is similar to a Rankine cycle but uses an organic working fluid instead of steam. The 100 W OTEC demo consists of an organic Rankine cycle using pure ammonia as the working fluid. Figure 3.1 shows a schematic representation of the experimental setup. Liquid pure ammonia is pumped by the process pump towards the evaporator. The ammonia is vaporized in a brazed heat exchanger by a hot water stream supplied by a hot water tank. The hot water tank contains a heating coil that brings the temperature to the desired value. The vapor ammonia flows towards a separation column, where the vapor is sent towards the 100 W turbine and the remaining liquid falls down due to gravity. The vapor is expanded and flows to the inlet of the GPHE. The liquid is sent through a recuperator, that pre-heats the liquid ammonia right before entering the evaporator. The vapor and liquid are reunited right before entering the GPHE. The two-phase working fluid is partially condensed in the GPHE, that serves as the test section in this study. After the GPHE, the two-phase flow is fully condensed in the sub-cooler, which is a brazed heat exchanger. The GPHE and sub-cooler condense the working fluid by use of cold water supplied by a cold water tank. Right before the process pump, a buffer tank is placed to make sure all the fluid is in a liquid state before entering the process pump.

3.1.2. Components

A short description of the most important components is given. The test section is described in more detail in section 3.2.

Heat exchangers
In the OTEC-demo four heat exchangers are present. All heat exchangers are brazed plate heat exchangers except for the GPHE, which is a gasketed plate heat exchanger. The benefit of this heat exchanger is that the

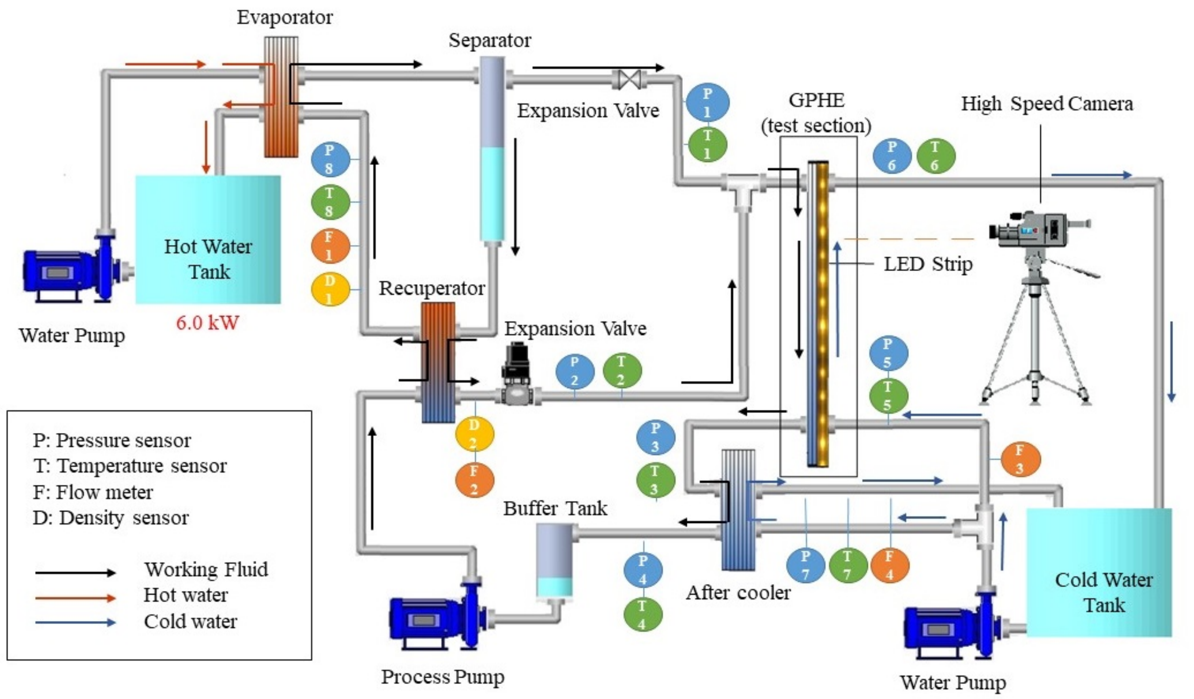

Figure 3.1: Schematic representation of the 100 W OTEC demo

amount of heat transfer plates can be varied. This gives freedom in performing research on the performance on the OTEC cycle and the GPHE for varying circumstances.

Separator & turbine
The separator – as the name inclines – separates the liquid from the vapor ammonia. The turbine requires a working fluid that is fully vapor, otherwise the liquid drops cause damage to the turbine and cause a lower efficiency. In the current OTEC demo, the turbine is replaced with an expansion valve, because it is easier to stabilize this system and maintain a steady state.

Pumps
The OTEC-demo contains three pumps. The process pump is a membrane pump and creates the working fluid flow. The two pumps that pump the water from and toward the water tanks are centrifugal pumps.

Sensors and valves
Several sensor types are used in the OTEC demo. In Figure 3.1 these sensors are indicated by the colored circles containing pressure sensors (P), temperature sensors (T) and flow meters (F). A pressure differential sensor is also installed to measure the pressure drop of the GPHE accurately. An expansion valve is placed after the separator to make sure that the pressure of the liquid and vapor ammonia are similar. The demo contains a lot of valves that are used for filling the system, draining and compartmentalising the system.

3.1.3. Control system

Bluerise B.V. uses a LabVIEW interface, which shows the measured values from the OTEC-demo at the corresponding sensor. The control system makes sure the pressure inside the system does not exceed a pressure of 12 bara and controls the expansion valve located between the recuperator and the condenser. With LabVIEW, the fluid flow rates and desired temperatures of the water tanks can be controlled.

3.2. Test section for flow visualization

The test section for flow visualization contains a partially insulated GPHE, a visualization plate, a stainless steel pressure plate with windows, a camera on an adjustable tripod and a LED-strip. For the flow visualization experiments, two stainless steel heat transfer plates are used for a single channel working fluid arrangement. One channel contains the ammonia working fluid and the other channel contains a cold water flow. An outer transparent visualization and a stainless steel windowed pressure plate is placed on the working fluid side to visualize the condensing ammonia. The test section is used to perform single channel flow visualization experiments. With single channel, it is meant that through one channel ammonia flows downward, and in one channel cold water flows upward, see Figure 3.2. Only one stainless steel effective heat transfer plate is used.

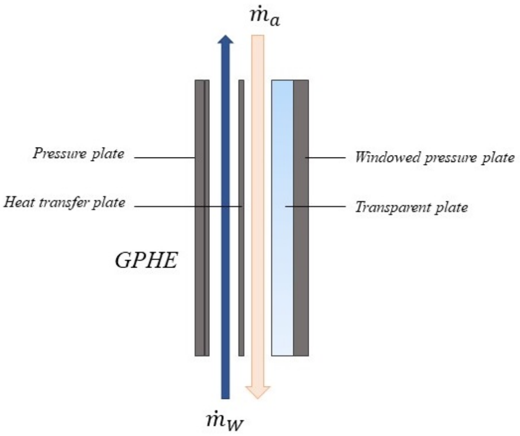

Figure 3.2: Schematic representation of single channel arrangement in GPHE, where $\dot{m}_W$ the cold water mass flow rate and $\dot{m}_a$ is the ammonia mass flow rate

Table 3.1: Plate specifications of the corrugated stainless steel plates inside the condenser

Description	***Symbol***	***Dimension***	***Value***
Channel gap*	d_g	[mm]	1.72
Chevron angle*	β	[°]	63
Corrugation pitch*	p	[mm]	7.5
Corrugation wavelength*	λ_{wave}	[mm]	6.67
Effective width of flow	L_w	[mm]	95
Enhancement factor	ϕ	[-]	1.149
Flow passage area	A_{fp}	[cm^2]	0.1634
Effective heat transfer area	A_{eff}	[m^2]	0.537
Hydraulic diameter	d_h	[mm]	2.99
Plate thickness*	d_p	[mm]	0.58
Port diameter	D_p	[m]	0.035
Port to port length plate	L_v	[m]	0.668
Port-to-port width	L_h	[m]	0.06
Thermal conductivity	κ	[Wm^{-1}K^{-1}]	16.3

3.2.1. Specifications original gasketed plate heat exchanger

The GPHE is a TL3BFG10 GPHE by Alfa LavalTM, and the original configuration is shown in Figure 3.3 (left) including two epoxy painted steel pressure plates. The middle and right images in Figure 3.3 show the overall dimensions of the GPHE. Table 3.1 shows the geometrical parameters of the stainless steel heat transfer plates. The values marked in the description with a '*' in the table are measured by hand by Dahlgren [16]. Figure 3.4 shows the schematic diagram of the configuration of the corrugations for the stainless steel heat transfer plates inside the GPHE. The hot and cold streams flow counter currently.

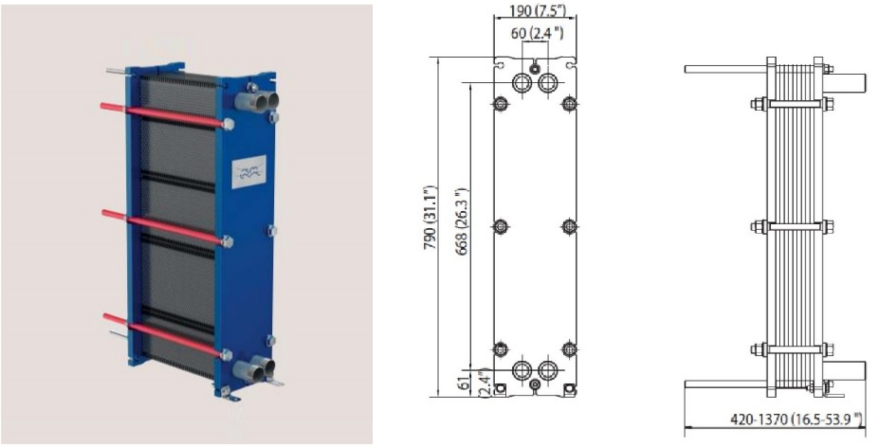

Figure 3.3: Left) The original TL3BFG10 gasketed plate heat exchanger by Alfa Laval^{TM}. Middle) Dimensions outer pressure plate. Right) Dimensions of the inlet port length and suspension tube in mm (inches)

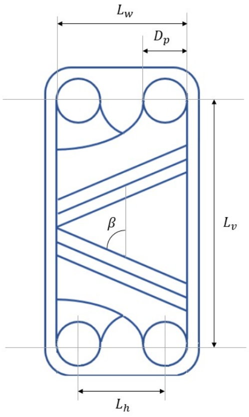

Figure 3.4: Schematic diagram of the heat transfer plates

3.2.2. Specifications of the windowed stainless steel pressure plate

The stainless steel pressure plate contains three windows and is designed and manufactured by Dahlgren [16]. It replaces one of the epoxy painted pressure plates of the original GPHE to enable visualization through the windows. This pressure plate has the same outer dimensions as the painted epoxy plates. The windows all have a width of 86 mm. The height of the middle window is 157 mm, and the maximum height of the upper and bottom window is 248.5 mm. The windowed stainless steel pressure plate is shown in Figure 3.8 b).

3.2.3. Specifications of the visualization plate

The visualization plate is a transparent polymer plate made of two layers, a 4.75 mm thick Polystyrene (PS) layer, and a 20 mm thick Polymethylmethacrylaat (PMMA) layer, see Figure 3.8 a). The plate is produced by a CNC-machine at the DEMO TU Delft. The model is generated in Solidworks 2018 by Dahlgren [16] and is used in this study for manufacturing the visualization plate. The visualization plate is designed to have the same corrugated pattern as the stainless steel heat transfer plates on one side. The other side is flat, so the windowed pressure plate can easily be pressed onto the transparent plate. The plate is designed to be chemically compatible with ammonia, able to withstand a maximum operational pressure of 12 bar and has a good optical quality. However, the model designed in Solidworks does not match exactly the dimensions of the heat transfer plates by the following:

- The modelled corrugations on the transparent plate: Because production of the plate was otherwise impossible, the corrugations on the transparent plate have connected linear parts instead of a continuous bend, see Figure 3.5. However, it is expected that this modification in the corrugation zone will have a limited on the flow pattern.

- Distribution zone: The distribution zone of the plate is located on the top and bottom of the plate and contains a less detailed structure. Dahlgren [16] mentions that it is unclear how much the distribution zone influences the flow.

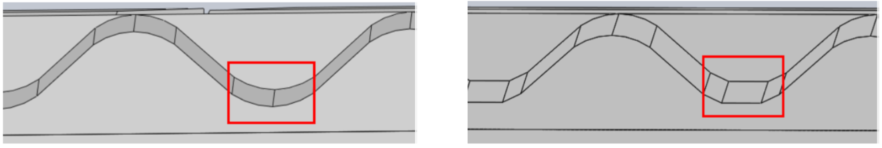

Figure 3.5: Left) The corrugated pattern on the steel plate, by Dahlgren [16]. Right) The corrugation on the transparent plate, by Dahlgren [16].

3.2.4. High speed camera

Calculating gas bubble velocity & required frame rate of the camera
The ammonia flowing through the section contains both liquid and vapor phases. It is typically the case that the vapor flow will have a higher velocity than the liquid [27], and should be computed in order to determine whether the camera is suitable for capturing clear images of the vapor bubbles. The experimental conditions of the experiments performed by Tao for pure ammonia, single channel configuration, will be repeated for the flow visualization experiments. For this reason, the determination of the inlet quality, superficial vapor phase velocity and required camera frame rate are based on the experimental conditions of the experiments performed by Tao.

Inlet quality gasketed heat exchanger
The inlet quality of the ammonia working fluid is necessary to compute the required frame rate of the camera. The vapor quality will be highest at the inlet of the condenser, which is why the inlet conditions of the GPHE are used to compute the upper limit of the required frame rate. The brazed heat exchanger functions as a sub-cooler to make sure that liquid only flows through the process pump. The single phase condition at the outlet of the brazed heat exchanger is used to determine the enthalpy of the ammonia. An energy balance is used to determine the two-phase enthalpy at the inlet of the brazed heat exchanger, which is assumed to be the same as the enthalpy at the outlet of the GPHE. Using a second energy balance, the enthalpy of the pure ammonia at the inlet of the GPHE can be determined. By interpolation, see Equation 3.1, the inlet quality of the GPHE is determined using the steady state experimental data from the OTEC demo generated by Tao. h_L and h_V represent the liquid and vapor phase enthalpy of the saturated ammonia at the inlet of the GPHE. The inlet quality x_i of the GPHE determined by the energy balance is indicated in Figure 3.6 by the blue markers.

$$x_i = \frac{h_i - h_L}{h_V - h_L} \tag{3.1}$$

The inlet quality can also be determined by dividing the vapor mass flow rate over the total mass flow rate of the ammonia, see Equation 3.2.

$$x_{i,Val} = \frac{\dot{m}_{a,V}}{\dot{m}_{a,V} + \dot{m}_{a,L}} \tag{3.2}$$

However, these sensors are less accurate in the OTEC demo, and so this calculation is used for validating the inlet quality from the energy balances only. The inlet quality determined by Equation 3.2 is indicated in Figure 3.6 by the red markers.

Figure 3.6 shows that the outlet quality x_o of the GPHE follows the trend line of the inlet quality x_i of the GPHE and is also lower than that of the gasketed heat exchanger, which is expected. The inlet quality $x_{i,Val}$ determined by the Equation 3.2 seems quite accurate for lower vapor qualities, and deviates somewhat from the results of Equation 3.1 at higher vapor qualities. It can be concluded that the calculation for the inlet

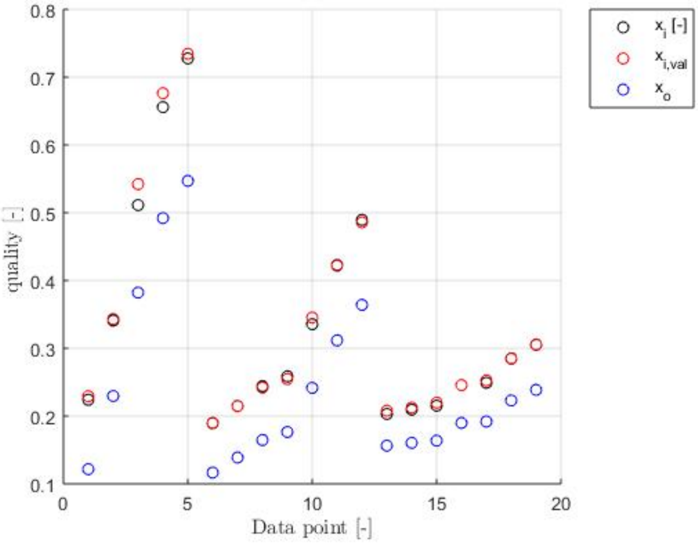

Figure 3.6: GPHE Inlet qualities of the experiments performed by Tao

quality of the gasketed heat exchanger by energy balances is validated and can be used for the determination of the vapor phase velocity.

vapor phase velocity
The vapor phase velocity is referred to by Tao et al. [45] as the superficial gas velocity and given by Equation 3.3, where x_i is used to over predict the vapor phase velocity.

$$u_V = \frac{\dot{m}_a x_i}{\rho_V A_{fp,V}} \quad [m/s] \tag{3.3}$$

Where $A_{fp,V} = \epsilon A_{fp}$. $A_{fp,V}$ is the flow passage area occupied by the vapor phase and ϵ is the volumetric void fraction inside the channel. Several void fraction relations are available, but when it is expected that the vapor phase has a higher velocity than the liquid phase, the slip ratio based void fraction model is recommended by Jassim [27], see Equation 3.4 and 3.5.

$$\epsilon = \frac{1}{1+\left(\frac{1-x_i}{x_i}\right)\left(\frac{\rho_V}{\rho_L}\right)S} \tag{3.4}$$

and

$$S = \left(\frac{\rho_L}{\rho_V}\right)^{\frac{1}{3}} \tag{3.5}$$

Where S is the slip ratio analytically derived by Zivi [60], assuming ideal, steady annular flow where the rate of entropy production is minimized, no liquid entrainment is present, and negligible wall friction is assumed.

Required frame rate of the camera
In order to gain a clear image of the bubbles without receiving strike-outs of bubbles on the image, the velocity of the bubble should be within a certain upper boundary.

The magnification ratio:

$$M = \frac{y_i}{y_o} \tag{3.6}$$

represents the ratio of the height of the image y_i inside the camera (1 cm) over the height of the object y_o, in case of the heat exchanger (80 cm) and leaves $M = \frac{1}{80}$. For the image not to be blurry, the bubble movement Δx on the image may not be larger than the height of 1 pixel on the image. For the available camera, the height of the pixel is 17 μm. The required frame rate rate ψ follows by equation:

$$\psi = \frac{1}{\Delta t} = \frac{u_V}{\frac{\Delta x}{M}} \quad [s^{-1}] \tag{3.7}$$

When the data of the pure ammonia experiments are implemented into these equations, the following range of frame rates are required to capture the vapor bubbles on a clear image for the working fluid mass flow rates and inlet qualities.

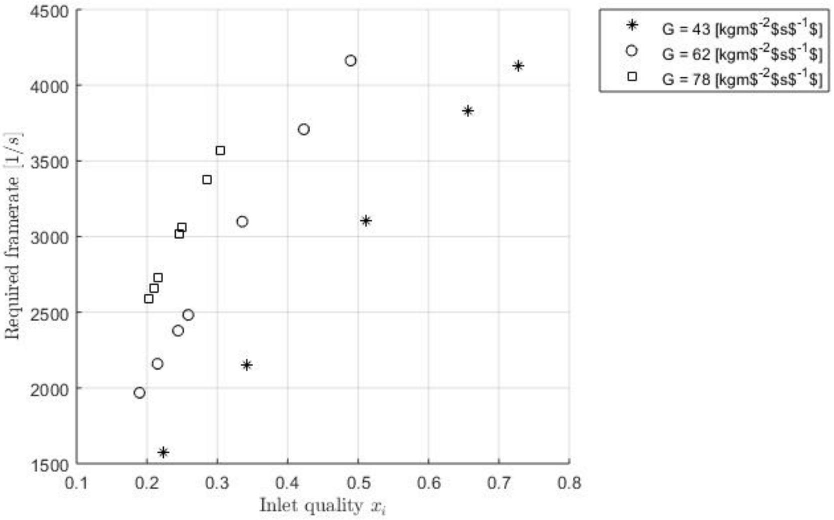

Figure 3.7: Required frame rate ψ versus inlet quality x_i

The available camera from the TU Delft Fluid mechanics department has a maximum frame rate of 3000 frames per second for a high resolution. These calculations formed the basis for selecting this camera, since the calculations predict that the camera is suitable for a range of the experiments, see Figure 3.7. Eventually, the camera was able to record all experiments up to vapor qualities of 0.6, which means that the calculations over predict the required frame rate. The high speed camera is connected to Photron FASTCAM Viewer software (PFV). The camera is mounted on a tripod, that is adjustable to the height of all windows and can therefore capture the flow over the total length of the channel, see Figure 3.8 d).

3.2.5. LED-strip

In section 2.2.2 several experimental configurations used in former research done are explained. However, the current setup has only one transparent side and therefor a configuration which uses illumination at the backside of the test section is not an option. Illuminating the visualization section can be done by frontal illumination, but previous studies mention that reflection can be problematic. For this reason, circumferential illumination by a LED-strip is tested and is proven to be sufficient. A 500 cm LED strip with 300 LED's is added to the visualization section. The degree of protection for this LED strip is IP-65 which means that it is waterproof and insensitive to dust. The LED strip encircles the transparent plate twice. The output voltage of the LED strip is 24 V and requires a current of at least 0.8 A. On the adapter the amount of Ampere can be varied between 0 and 3 Ampere so it can act as a dimmer. Because of the high density of LED's per meter, the light is well distributed over the visual area. Figure 3.8 c) shows the visualization section including the illumination by the LED strip.

3.2.6. Concluding remarks

The experimental setup serves as the main tool for answering the main research question in this study. The setup allows for determining the occurring flow patterns. The illumination will make the flow path and pattern clear, while the high speed camera records the flow for every stable experimental condition. The data from the camera is stored and can be used for image processing to recognize specific area's, shapes and movement of the flow that might relate to the heat transfer. At the same time the sensor values are stored for every condition and can be later on processed by data reduction to answer the question of how the flow patterns and heat transfer are related. Also, the combination of the recorded flow and the sensor data allows for producing a specific flow pattern map of the GPHE, which is desired.

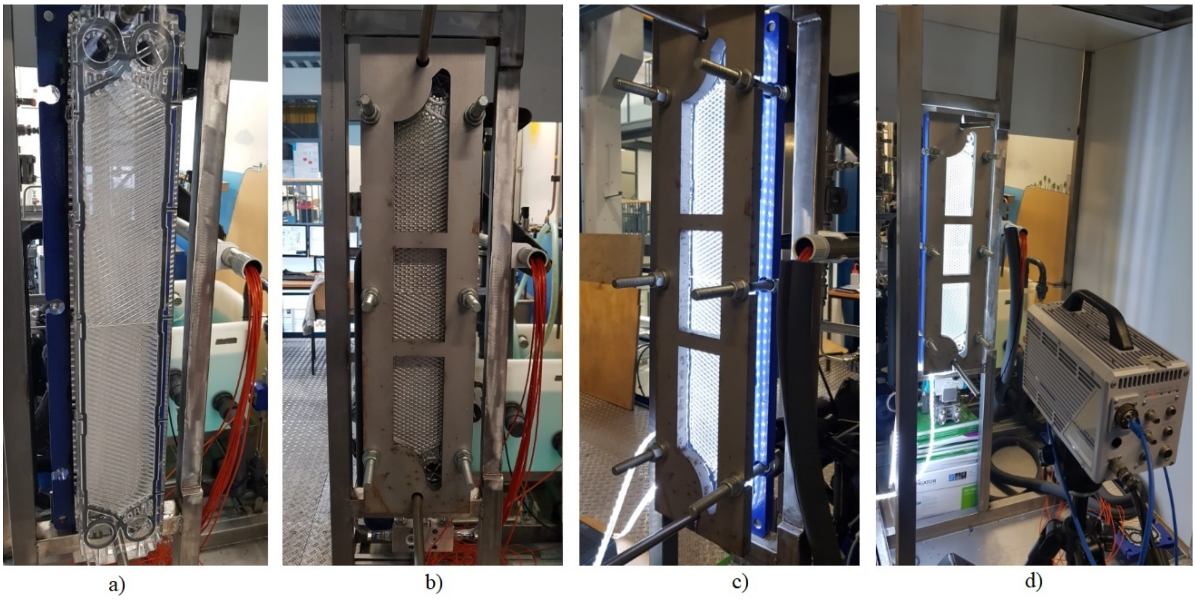

Figure 3.8: Experimental setup of test section. a) Visualization plate. b) Windowed pressure plate. c) illuminated setup by LED-strip. d) High speed camera positioned in front of setup

4

Material selection and production visualization plate

This chapter elaborates on the research performed for selecting a suitable material for the visualization plate. First, the cause of failure of the former plate produced by Dahlgren is diagnosed. Materials are selected to investigate on its performance and the production method of the visualization plate is presented. Finally, the cause of failure of the final visualization plate is discussed.

4.1. Failure diagnostics PMMA plate

The PMMA visualization plate produced by Dahlgren[16] appeared to be unsuitable for performing visualization experiments in the OTEC demo. This section explains the causes of failure and how these diagnostics are established.

4.1.1. Visual analysis on the PMMA plate

The plate was mounted on the GPHE, tightened with six bolts up to an applied moment of 70 Nm such that the leak of ammonia from the system was considered acceptable. The plate appeared geometrically suitable for the heat exchanger, and showed no clear deviations in the patterns from the stainless steel plates. However, the ammonia flow inside the system appeared to be blocked by the transparent plate. No ammonia mass flow rate was detected by the flow meters while the pump was activated. Three liquid columns became visible behind the transparent plate, indicating that some material was blocking the flow passage, see Figure 4.1. The columns are indicated by the white numbers.

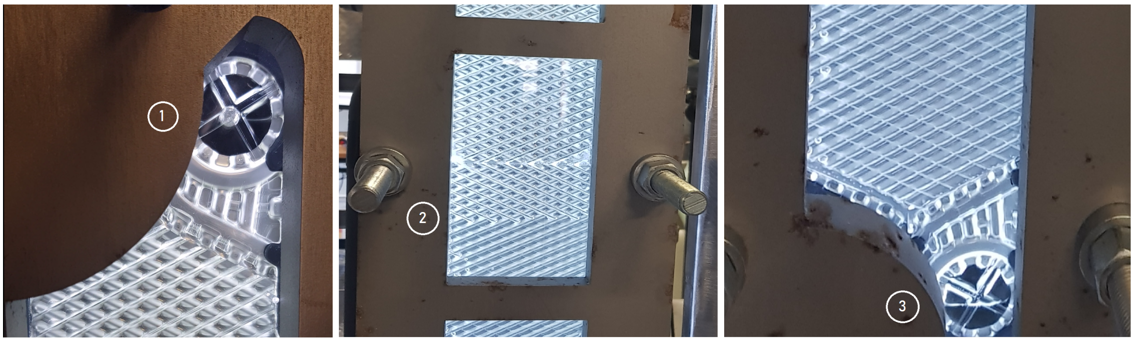

Figure 4.1: The liquid columns on the top (1), middle (2) and bottom of the plate (3)

Visible material alterations within 24 hours after dismounting
After dismounting the transparent PMMA plate, it became clear that the geometry of the plate was affected. The corrugations and inlet/outlet patterns that were 1.72 mm higher than the base plate were pressed down and smeared over the area that served as flow passages, causing to block the flow. Only the area of the plate that was in contact with the ammonia was intensely affected. The base plate was slightly warped. Another dominant phenomenon that appeared was the imprint of the corrugated steel plate into the transparent material. The absence of small cracks due to point forces indicates that the material had softened while being in contact with the ammonia, and hardened later into a rigid structure when the ammonia was absent, see Figure 4.2.

Figure 4.2: Deformed corrugations on the PMMA plate by imprint of the stainless steel heat transfer plate

Visible material alterations within a week after dismounting
Over time, the effects increased. The base plate started to buckle and large cracks appeared in the base plate, see Figure 4.3. A pungent smell of ammonia was present, indicating that the plate had absorbed the ammonia and was now slowly releasing ammonia vapor into the ambient air. This process caused the emergence of cracks and the plate to buckle.

Figure 4.3: The emergence of cracks on the PMMA plate after a week

Visible material alterations a month after dismounting
After a month, the entire surface of the corrugated zone was teared up into shards and some were broken off from the base plate. The area where the corrugated zone was glued onto the base plate also showed severe damage. This could indicate that ammonia was stored behind the corrugated zone. These phenomena indicated that the pure ammonia played a major role in the failure of the plate.

The material could have been damaged due to a lack of mechanical performance, a lack of chemical resistance to ammonia, or a combination of it. Due to the fact that the material damage increased over time indicates the dominant role of ammonia. However, a mechanical analysis is ought to be necessary to rule out the possibility of fatigue due to a lack of mechanical performance. CES Edupack (2018) states that PMMA is chemically compatible with ammonia, which is why it is considered necessary to perform a chemical resistance test to prove that indeed the ammonia had caused the severe damage.

4.1.2. Mechanical analysis on the transparent PMMA plate

Dahlgren [16] estimated the maximum deflection due to buckling by using the theory of flexure of slabs by Westergaard [54]. If the PMMA plate with a thickness of 3 cm was subjected to a pressure of 12 bar then this deflection was predicted to be 0.032 mm and considered acceptable. However, the plate is subjected to more different kind of deformations than buckling alone, which might have played a role in the failure of the PMMA plate. In section 4.4 a finite element analysis (FEA) is performed to check if it is expected that the plate is deformed or damaged due to bending or compression.

Reduced tensile strength PMMA plate
The tensile strength of a material is the measured maximum stress that a material can withstand while being stretched or pulled before breaking. AzoM [37] states a tensile strength of 70 MPa for PMMA, and CES Edupack [32] cites a range between 48.3 - 72.4 MPa. The stress-strain curve for PMMA however changes with varying temperature [13], see Figure 4.4. With a higher temperature, the tensile stress drops significantly. In the material properties sheet delivered by AzoM and CES Edupack no temperature is presented for the given properties. If 70 MPa holds for a temperature of 20 degrees, than a lower tensile strength than 70 MPa is expected for higher temperatures. To over predict the stresses in the PMMA plate, a higher temperature is assumed (between 20°C and 30°C) for the ammonia side of the condenser. From Figure 4.4 a tensile strength of approximately 50 MPa is assumed for these temperatures.

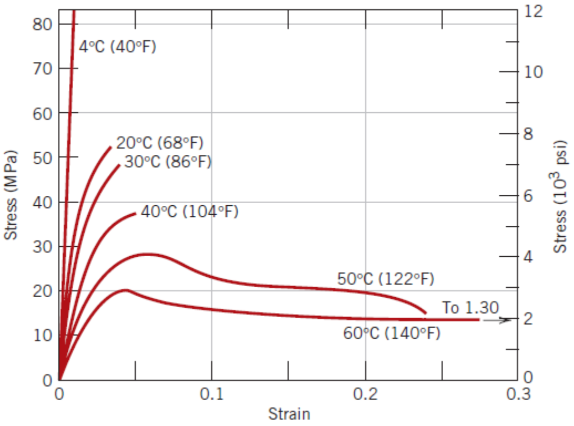

Figure 4.4: The influence of temperature on the stress-strain characteristics of PMMA [13]

F. Scrutton [42] concluded that after machining, the material PMMA becomes more brittle instead of ductile, which means a yield stress is not a measure that can be taken into account to avoid permanent deformations on the plate. Before reaching the tensile stress of the plate, deformations in the structure of the material can already take place, which is undesired. To compromise this effect, a safety factor of 3 is used. This reduces the tensile strength to 16.67 MPa:

$$\Sigma_{red,t} = \frac{\Sigma_{in,t}}{3} = \frac{50}{3} \tag{4.1}$$

The FEA results showed that the internal stresses are below the reduced tensile strength for mounting and operation and that the displacement is minimal, see Table 4.5. Therefore, it is unlikely for the plate to have failed due to mechanical ineptness.

4.1.3. Chemical compatibility with ammonia

Chemical charts on chemical resistance of PMMA to ammonia
Dahlgren [16] investigated the chemical compatibility of PMMA with ammonia using the material data- base from CES Edupack. CES Edupack [32] suggests that PMMA has a good chemical resistance to ammonia, but does not state any specific conditions. Cyro [23] offers a chemical resistance chart of PMMA including an aqueous solution of ammonia and classifies PMMA to be resistant. Gammacril [17] also states that PMMA is resistant to pure ammonia and ammonia-water solutions. However, no test conditions are mentioned. The Brain-researchlab [31] offers a chemical resistance list for pure ammonia at a temperature of 20 °C and 50 °C. It states that at a lower temperature, some damage was observed after 7 days on the surface. Nalgene Labwear [41] states for PMMA an excellent resistance for at least 30 days at 20 °C. Eriks [11] offers a chemical compatibility list for PMMA, and states that the PMMA is strongly attacked by high concentrated ammonia. Non of the lists give details on the test conditions. The varying results may be due to the difference in a liquid/vapor phase. This stresses the importance of performing chemical tests for the desired experimental conditions before production.

Chemical resistance test with liquid ammonia and PMMA and PVC samples
Four samples of PMMA and polyvinylchloride (PVC) were gathered. PVC is according to most literature chemically compatible with ammonia and has both good mechanical performance and optical quality. PMMA and PVC samples were tested at the same time to speed up the process for finding a new material. The samples were placed in the working fluid pipe connected to the outlet of the GPHE inside the OTEC demo. Figure 4.5 shows the samples before the test was performed. The colorless samples are PMMA and the samples with a blue haze are PVC.

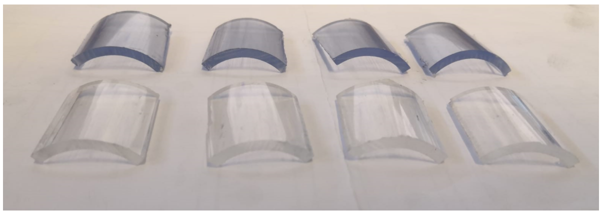

Figure 4.5: PVC (blue haze) and PMMA samples (colourless) before the test

The system was filled with ammonia and the samples were left in liquid ammonia for four days. The samples after performing the test are presented in Figure 4.6.

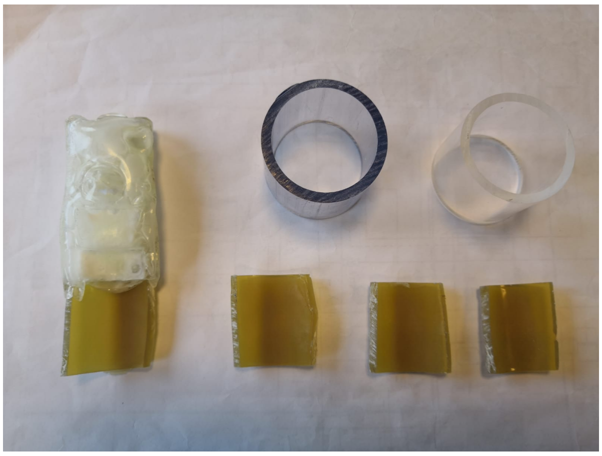

Figure 4.6: PVC (brown) and PMMA samples (white,bulky) after the test

One can see from Figure 4.6 that the PMMA samples clogged together, lost their transparency, grew in size due to absorption and became bubbly. The PVC samples turned brown, lost their transparency and became rubbery, indicating that it has lost its stiffness.

Table 4.1: Flow visualization materials used by previous studies

	Working Fluid	*Material visualization section*
Arima et al. [6]	Pure ammonia	Glass
Arima et al. [7]	Ammonia/water	Glass
Xue et al. [57]	Ammonia	Quartz glass
Vlasiogannis [51]	Air/water	PMMA
HJ Kim [28]	R-245fa	Optically clear resin
Jassim [26]	R-134a	Clear PVC
Al Zaidi [3]	HFE-7100	Polycarbonate
Oshinowo et al. [39]	Air/water & Air/glycerol	PMMA
Nilpueng & Wongwises [38]	Air/water	Polyurethane resin
Tribbe & Müller-Steinhagen [48][49]	Air/water	Polyester
Grabenstein et al. [20]	Water/air	Polyurethane (PU)

4.1.4. Materials used for flow visualization in previous studies

Table 4.1 gives an overview of used materials for visualization studies. Arima et al.[7],[6] use three sight glasses built in a stainless steel flat plate with a thickness of 30 mm for the visualization of ammonia/water mixtures and pure ammonia. Xue et al.[57] experimented on full visualization and start-up performances of a pulsating heat pipe while using ammonia. For this study, quartz glass tubes were used. No literature is found where polymers are used for visualization studies with ammonia as the working fluid. This stresses the importance of investigating the possibilities for glass as a visualization plate material.

Willighagen [55] performed a review on various polymers for the purpose of utilizing polymer heat transfer plates in OTEC heat exchangers. In this overview, a distinction is made between vapor/liquid ammonia and the chemical resistance is classified from 1 - 9, where 9 is an excellent resistance and 1 is poor resistance. The materials that showed high values were evaluated in CES Edupack to see which materials are transparent. Polystyrene, Prolyprolyene (PP), Polysulfone (PSU) and Acrylonitrile butadiene styrene (ABS) raised as possibilities. The refractive index, E-modulus, Youngs-modulus, Tensile strength and absorption showed to be promising. However, there was no availability of PP and PSU samples throughout the Netherlands, except for a sample of a thin transparent PS-sheet.

4.1.5. Conclusions on PMMA fatigue

From the PMMA plate failure diagnostics, the following conclusions are drawn:

- Using chemical charts, CES Edupack and other sources solely to determine the chemical compatibility of a material towards vapor/liquid ammonia proves to be insufficient. Chemical compatibility charts hardly state experimental conditions. Therefore, sample tests are required to prove the chemical compatibility of a material towards ammonia for the desired conditions.

- The sample test with PMMA and liquid ammonia proves that PMMA is not chemically resistant to liquid ammonia. PMMA absorbs the ammonia and deforms heavily.

- PVC is not chemically resistant to liquid ammonia and therefore not a suitable material for replacing the PMMA material.

- The FEA results indicate that the mechanical performance of the PMMA plate was fit to serve the visualization experiments in the GPHE. It is therefore concluded that the plate did not fatigue due to a lack of mechanical performance.

- More research is necessary to replace the material of the failed PMMA plate for the visualization experiments. Therefore, glass and other polymers are investigated on their mechanical performance and chemical resistance in the next sections.

Table 4.2: Several properties of soda lime silicate glass and borosilicate glass

	Soda lime silicate glass	*Borosilicate glass*
Young's Modulus [GPa]	68-72	49.7-52.2
Tensile Strength [MPa]	30.2-33.3	23.3-25.6
Compressive Strength [MPa]	302-333	232-256
Shear Modulus [GPa]	27.9-29.6	20.4-21.4
Fracture Toughness K [MPa*m^0.5]	0.64	0.545
Thermal conductivity [W/m°C]	0.7-1.3	1.1-1.2
Thermal shock resistance [°C]	46.9-52.9	141-159
Thermal expansion coefficient [ϵ_S/°C]	8.92E^{-6} -9.82E^{-6}	3.13-3.26
Sodium Oxide content by weight [%]	15	0.5
Price [GBP/kg]	1.07-1.26	3.41-5.68

4.2. Research on performance of Glass

Common used glass types for machining are soda lime silicate glass and borosilicate glass. Soda lime silicate glass is often utilized in windows of buildings. Borosilicate is often used in laboratories and is already present in the separator of the OTEC demo. It's resistance towards liquid ammonia is therefore already proven. This section compares the properties of soda lime silicate glass and borosilicate glass and an FEA is performed to predict the mechanical performance of glass inside the setup. At last, production methods are evaluated to investigate if the detailed pattern of the corrugations is possible to create using glass and if alterations to the geometry need to be made.

4.2.1. Comparison of glass properties

Glass has no plasticity phase, which means that glass does not deform first before collapsing. Figure 4.7 shows linear stress-strain behaviour of glass up to the moment of failure.

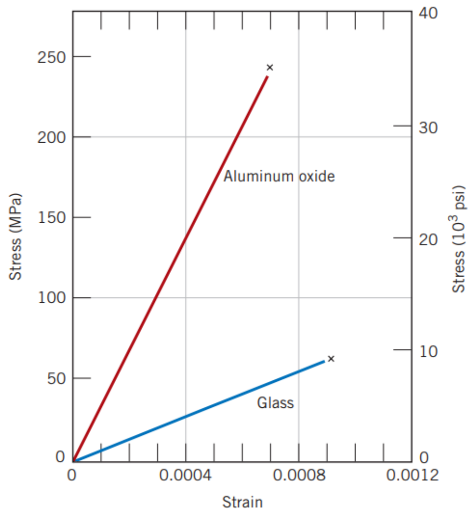

Figure 4.7: Typical stress–strain behavior to fracture for aluminum-oxide and glass [12]

On the glass surface micro-cracks are present due to its standard fabrication process [36]. After milling the plate, even more micro-cracks will be present. The initial micro-cracks start to widen when local stresses become higher than the atomic covalent bonds surrounding the micro-cracks. This leads to failure (Veer [50]). Soda lime silicate glass has the benefit that it is easier to machine than borosilicate glass. The main disadvantage of soda lime silicate glass is the relatively high thermal expansion and poor resistance to thermal shock. This is due to the soda content in the glass [36]. Borosilicate has the main benefit that it has a good chemical durability, a high maximum service temperature and high resistance to thermal shock [36].

While draining the ammonia from the OTEC system, the temperature can suddenly drop from 17°C to - 33 °C, which causes a sudden temperature drop of 50 K. The lower limit of the thermal shock resistance of soda lime silicate glass is 46.9 K. This means that there is a risk of damaging the soda lime silicate glass plate while draining the system from ammonia. If borosilicate glass is chosen, this risk is absent. Furthermore, Table 4.2 shows that the Young's modulus, tensile Strength, compressive strength, shear modulus and fracture toughness are all higher for soda lime silicate glass as compared to borosilicate. This makes soda lime silicate glass the most advantageous option, as long as the draining process of the OTEC demo is done with extra care. From this conclusion, soda lime silicate glass only is further considered for analysis.

4.2.2. Reduced bending tensile strength

Glass is well resistant to an evenly distributed compression but not to bending, see Table 4.2. This means that the bending tensile strength is an important property to evaluate. The Dutch Design Code 'NEN 2608,2014' [24] mentions that the bending tensile strength of soda lime silicate glass is strongly reduced when machining of glass plates or other factors are involved. The Dutch design code suggests a method to approach the reduced bending tensile strength. The factors reduce the initial tensile strength of the soda lime silicate glass by Equation 4.2:

$$\Sigma_{red,t} = \frac{\Sigma_{in,t} k_a k_e k_{mod} k_{sp}}{SF} \tag{4.2}$$

The strength reducing factors are as follows:

- k_e: Factor including directions of load due to plate geometry
- k_{sp}: Factor including surface factors such as coatings
- k_a: Factor including stress distribution on the surface
- k_{mod}: Modification factor including duration of load and contact with fluids

These strength reducing factors have a value between 0 and 1. The values are determined by following the method described by the Dutch design code 'NEN 2608,2014'. For the glass visualization plate the values are as follows:

- $k_e = 0.8$ due to corrugation patterns in the plate diverging the directions of the load
- $k_{sp} = 1$ for uncoated soda lime silicate glass
- $k_a = 1.644 A_c{}^{-\frac{1}{25}} \approx 1$, where A is the contact surface of the load
- $k_{mod} = (\frac{5}{t})^{\frac{1}{c}} = 0.7445$, where t is the time duration of the most critical loading, c is the corrosion constant

Where A_c is the contact area between the effective heat transfer area and the visualization plate. The most critical load time t is assumed to be a day of operation. The corrosion constant c is 27 for humid circumstances. SF is the safety factor prescribed by the Dutch design code, where SF = 1.8. $\Sigma_{in,t}$ is the initial tensile strength of the soda lime silicate glass without machining, pre-tensioning and coating. CES Edupack shows a lower limit of the tensile strength of 30.2 MPa, see Table 4.2. The reduced tensile strength of the machined glass $\Sigma_{red,t}$ then becomes 10.7 MPa. This method predicts that the actual tensile strength of the plate is about 3 times lower than the tensile strength of soda lime silicate glass presented in databases.

4.2.3. Chemical compatibility with ammonia

Glass in general is known to be chemically well resistant to strong acids and alkali's, but less is known about the influence of ammonia on covalent bonding between atoms of glass. The presence of ammonia might enhance the crack propagation. A chemical test is performed where shattered soda lime silicate glass is stored in liquid ammonia for four days, and showed no crack propagation after four days, see Figure 4.8.

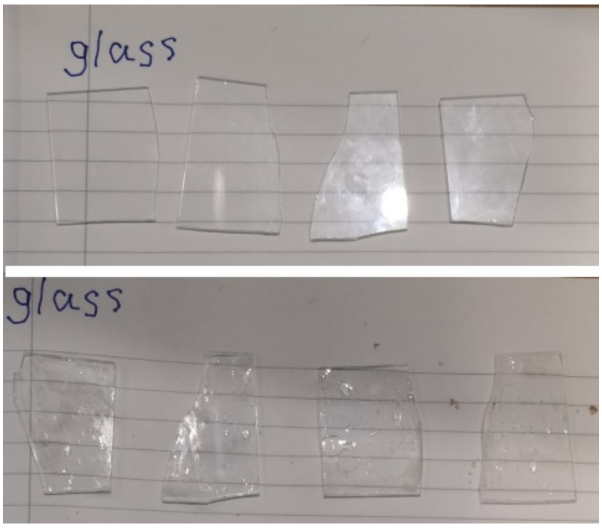

Figure 4.8: Soda lime silicate glass before (top) and after (bottom) chemical test

4.2.4. Mechanical performance

The largest thickness of a glass plate that still can be machined without risking the formation of large microcracks is 19 mm. An FEA is performed in section 4.4 to determine if the principle stresses inside the glass base plate do not exceed the tensile stress of 30.2 MPa and the reduced tensile stress of 10.7 MPa. The results show that for a plate with high tolerances the strength of the plate is only sufficient with respect to the initial tensile strength, but not the reduced tensile strength, see Table 4.5. It is not entirely sure if the reduced tensile strength is entirely accurate, since the method that is followed is designed for windows in buildings, but it gives some first reasons to doubt whether glass is a safe option for the PMMA visualization plate. This stresses the importance to elaborate on production methods and the tolerances of dimensions that come with the production method.

4.2.5. Production methods

To investigate the production methods for producing a corrugated glass plate, multiple companies are contacted that are in the business of producing of glass components. Most of the companies declined the proposed assignment due to the level of difficulty, but in the end two parties were open for discussion. Pouring of hot liquid glass into a mould and cold glass working are discussed.

Glass pouring
One of the expected possibilities is pouring glass into a steel mold. The mold could be produced easily since one of the available steel plates from the OTEC setup could be used as the bottom of the mold. However, after discussion it became clear that pouring glass would give the following difficulties:

- Having small corrugations with a height difference of only 1.72 mm would cause air to be embedded between the glass and the mold and alter the shape of the corrugations
- Pouring glass gives no guarantee in tolerances and absence of surface roughness, which is problematic since that will most likely cause extremely high stress concentrations and cause the glass plate to crack
- The cast would not maintain entirely flat/unbuckled over its length due to its timely discharge from the hot mold

Since high tolerances and surface smoothness are an absolute demand for the condenser not to leak or the plate not to fail under pressure and point forces, this option was declined.

Cold-glass working
Cold-glass working is the process of removing material from an existing glass plate using a grinding tool. However, removal of larger pieces of glass to produce the shape of the base plate brings the strength of the glass plate down drastically as compared to an original square shaped glass plate. The top and bottom of the

plate contain certain strong shapes, and these are considered to decrease the strength of the plate drastically. No alteration in the design with respect to fitting the steel pipe in the GPHE can be made.

A production method is milling the plate with a grinder wheel. However, this includes the necessity of geometrical alterations. The inlet/outlet ports and the gasket gaps can be produced, but not with the exact dimensions from the Solidworks model. A new rubber gasket needs to be produced to fit the new shape of the gasket gap. Second, the dimensions of the grinder wheel determine the shape of the corrugations, and are only capable of forming corrugations with a depth of 0.6 mm instead of 1.72 mm. This alters the flow path and pressure drop over the condenser, and is therefore expected to change the flow patterns which is undesirable. Leaving out the corrugations and forming a flat chamber inside the base plate is not an option, since the chamber will turn opaque due to the machining methods and therefore losing its transparency.

However, a diamond grinder can be developed that is capable of both making the corrugations and the patterns for the gasket, inlet and outlet ports of the plate. With this method the plate can be produced into the desired shape. This method is most costly with respect to investment and time as compared to the other production method. Second, the company cannot guarantee that the plate remains intact, which makes the risk on the production of such a plate with high costs very large.

4.2.6. Conclusions on the suitability of glass

Producing a visualization plate from glass contains large risks on investment, time and safety. The most effective production method is very costly and takes a lot of time. No guarantee can be given that once a crack forms in the plate during operation, crack propagation is prevented. The visualization experiments are performed with pure ammonia under pressure, and it is considered dangerous if the glass material bursts into scattering pieces and both liquid and vapor ammonia escape the setup with high velocities. It is decided that the search for a chemical compatible polymer is necessary. This research is described in the next section.

4.3. Research on performance of polymers

Polymers have the advantage of being easy to machine, they are inexpensive and known for beneficial mechanical performance. On the contrary, the chemical compatibility with a strong alkali like pure ammonia can be critical. It is most important to investigate the chemical compatibility before evaluating other properties of the material. In subsection 4.1.4 the polymer PS is mentioned that might be resistant to vapor and liquid ammonia. This section explains the results of chemical tests, the mechanical performance of PS and why PS is chosen to use for fabrication.

4.3.1. Chemical compatibility of several polymers

Various materials were available from the lab of Industrial Design and the DEMO at the TU Delft and were taken along in the chemical test. The chemical resistance of Polycarbonate (PC), Polyethylene Terephthalate Glycol (PETG) and PS are tested inside the OTEC demo for four days. The PC fully dissolved in the ammonia. PETG crumbled into a sand-like substance, see 4.9. The PS showed good results as no deformation, crack propagation and loss of transparency was observed. However, it was unknown how resistance of the material would change if the circumstances were also varied.

The same test is performed on PS, but now for different circumstances. A hole was created in an untested sample and pressurized by a screw and two bolts. Due to drilling of the gap, large cracks were present in the samples. Also, small rectangular PS samples were added that contained small cuts on the sides, i.e. samples that contained micro-cracks.

From Figure 4.10 it becomes clear that the chemical resistance changes when the conditions are also changed. The screwed samples lost their transparency and became soft. The rectangular samples that contained micro-cracks however did not change. It shows that once large cracks are present in the material, the chemical resistance to ammonia drops. Micro-cracks have less influence and do not change the chemical resistance of PS within a time span of four days. Because the plate needs to be machined, cracks or micro-cracks might be present in the material. For this reason, two samples were machined into the desired corrugation patterns with a CNC-machine by the DEMO TU Delft, see Figure 4.11. Stainless steel clamps were manufactured

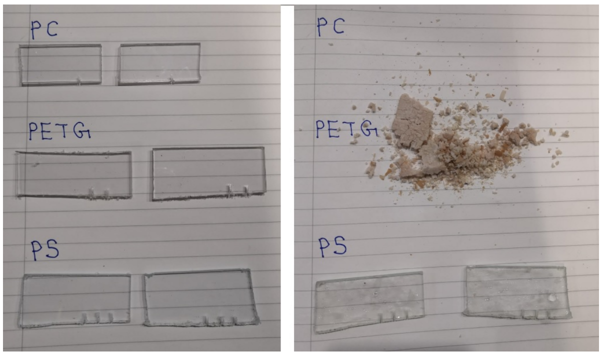

Figure 4.9: Left) Polymers before chemical test. Right) Polymers after chemical test in pure ammonia for four days

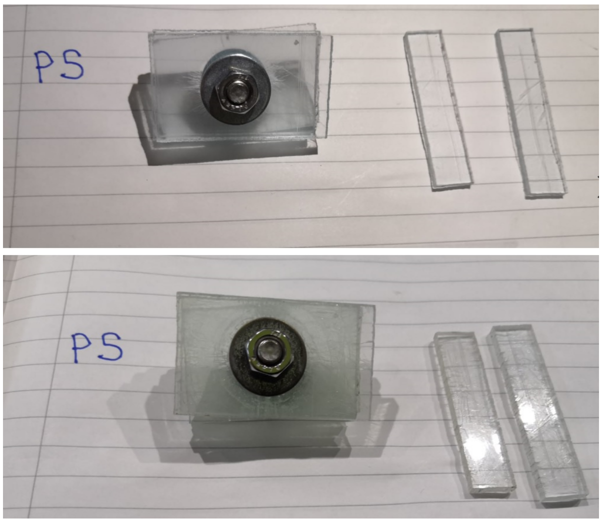

Figure 4.10: Top) PS under tension before chemical test. Right) PS under tension after chemical test

to press the samples onto each other. The clamped machined samples were tested for four days in liquid ammonia.

Figure 4.12 shows that the machined pattern did not reduce the chemical resistance. On the connection points between the stainless steel and the samples, very small scratches on the surface of the PS were observed. However, such point forces are not expected inside the GPHE and were therefore considered to be of minor importance. No transparency was lost and the effects of the ammonia were considered negligible.

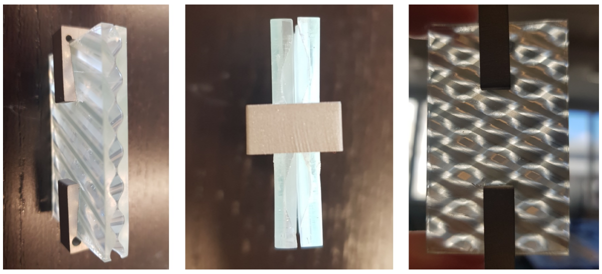

Figure 4.12: Left) Corrugated samples before chemical test. Middle) Top view of corrugated samples after test. Right) Side view of corrugated samples after test

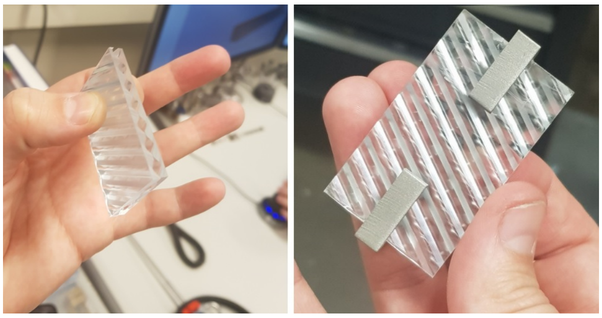

Figure 4.11: Left) Corrugated samples before chemical test. Right) Corrugated samples including stainless steel clamps before chemical test

4.3.2. Mechanical analysis of PS

PS has less strength as compared to PMMA. This means that PS should be investigated on its mechanical performance as well, since plastic deformation and cracks might occur due to stresses during operation.

Mechanical properties of PS
The mechanical properties of PS are compared to the properties of PMMA, see Table 4.3. The table shows that the Young's modulus, yield strength and tensile strength of PS is lower as compared to PMMA. The refractive index is higher, which means that the light passing through the material has a stronger angle and deforms the image a little more than PMMA.

Table 4.3: Several properties of PMMA and PS

	PMMA	*PS*
Young's Modulus [GPa]	2.24-3.24	1.2-2.6
Yield Strength [MPa]	53.8-72.4	28.7-56.2
Tensile Strength [MPa]	48.3-72.4	35.9-5.5
Poisson's ratio	0.387-0.4	0.387-0.4
Shear Modulus [GPa]	0.803-1.16	0.817-1.18
Thermal conductivity [W/m°C]	0.167-0.251	0.12-0.13
Absorption (Water@24h) [%]	01-0.4	0.817-1.18
Refractive index [°C]	1.49	1.55-1.61
Price [GPB/kg]	2.09-2.18	1.84-1.87

Since it is known that PMMA performs well with respect to leakages inside the setup and PS has lower mechanical strength, it is considered that only the top layer would consist out of PS, and the base plate of PMMA. For this reason, bending is not considered in the FEA of PS. However, if the top layer would be produced out of PS, the stress concentrations inside the corrugations are important to analyse. No detailed information is found on the stress strain relations of PS in a corrugated structure, except that corrugated patterns are expected to behave in a non-linear way for polymers. A non-linear analysis by a FEA is known for introducing large errors [2]. This stresses the importance of performing a physical material test with a sample of corrugated PS.

Mechanical performance of PS after chemical resistance test
To test the remaining strength and stiffness of the corrugated samples, a physical test is performed on a workbench in the Material science lab of the TU Delft. One corrugated sample is placed on top of the stainless steel plate and together they are placed inside the work bench of the materials lab, see Figure 4.13.

A compression test is performed, where the workbench pressurizes the materials until a desired pressure. The applied pressure to the sample was up to 18 bar. The measured deformation is of both the stainless steel plate and the sample, but it is assumed that the measured deformation is mostly due to the PS, as it has minor mechanical performance as compared to stainless steel. By vision it was clear that the sample showed no signs of cracks and plastic deformation. Figure 4.14 shows the results of the applied pressure versus the total deformation.

Figure 4.13: Left) Corrugated sample placed on the stainless steel plate. Right) Workbench ready to press the sample onto the steel plate

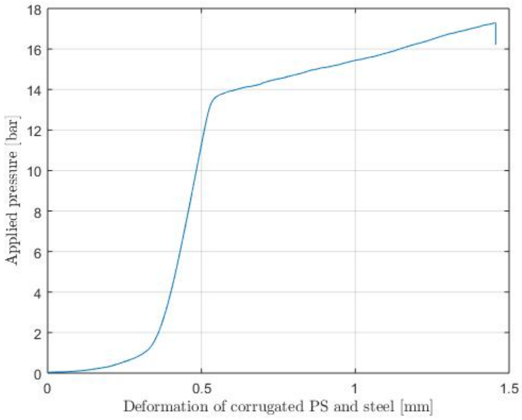

Figure 4.14: Applied pressure from workbench versus total deformation of stainless steel plate and corrugated sample

From Figure 4.14 it is clear that the response of the stainless steel plate and polymer is non-linear, which is expected for corrugated patterns [21]. The deformation rate enlarges after an applied pressure of 14 bar. However, it is expected that mounting the plate causes a pressure of 13 bar, where the total deformation is approximately 0.5 mm. This means that during the draining, the channel gap of 1.7 mm is not closed due to material compression.

4.3.3. Production method

The plate produced by Dahlgren [16] was designed in Solidworks 2018 and produced by the DEMO TU Delft. DEMO still had most of the code required for manufacturing the plate by a CNC-machine. This leads to lower production costs and the benefit of experience from the employees at the DEMO TU Delft. It was proven by the produced PMMA plate that the plate caused no leakages and fit the geometry of the GPHE without flaws. Production by the CNC-machine at the DEMO TU Delft is considered to be very beneficial.

4.3.4. Conclusions on the suitability of PS

From the research performed on the polymers, the following can be concluded:

- PETG and PC show a very bad chemical resistance to liquid ammonia, as the PC is fully dissolved and the PETG crumbled into small pieces. These material should never be used for applications that involve ammonia.
- Flat and smooth PS sheets show a good chemical resistance to liquid ammonia for at least four days. No signs of damage or loss in transparency are observed.

- PS material containing cracks inside the material shows less resistance, as it deforms, loses stiffness and transparency. This indicates that the resistance is not only dependent on conditions such as temperature, pressure and state of the chemical. The resistance of PS is also dependent on the physical state of the material itself.
- CNC-machined corrugated PS samples show a good chemical resistance to liquid ammonia for at least four days. No large cracks, modifications in geometry or loss in transparency is observed.
- The physical mechanical performance test in the material science lab showed non-linear deformation up to 18 bar, but the material remained intact and did not show signs of plastic deformation. The measured deformation of the material during the test did not show reason for doubts as the deformation was considered acceptable.
- PS is considered a material that performs well in the GPHE under operation with respect to chemical resistance and mechanical performance. PS is chosen as the corrugated layer material for the visualization plate.
- Production by a CNC-machine is advantageous with respect to time, costs and experienced employees at the DEMO TU Delft.

4.4. Finite Element Analysis

An FEA is a numerical method that can be used to solve a structural analysis for a specific geometry for a certain material. This is done in Solidworks 2018 following the method described in the book Finite element Analysis via Solidworks [2]. A static study is performed on PMMA and glass, calculating the displacements and stresses inside the material that involves mounting and operating the GPHE.

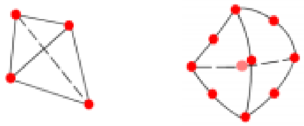

Figure 4.15: Left). Linear solid element, Right). Parabolic solid element [2]

Generally, Solidworks simulation assumes linear material behaviour for a static analysis, which means that the relationship between loads and displacement is assumed to be linear. Solidworks Simulation divides a geometry into small elements with a tetrahedral shape, a mesh. FEA uses both linear solid elements that have four nodes and parabolic solid elements that have 10, see Figure 4.15. Parabolic elements are placed at strong curvatures or difficult geometries where additional accuracy is required in terms of the discretization error. A finite element solution calculates the displacement of the nodes first, and the resulting strain in the attached elements second. Using Hooke's law the internal stresses Σ_{intern} are calculated, see Equation 4.3, where E is the square material matrix containing the elasticity modulus and the Poisson's ratio of the material, and ϵ_s is the strain.

$$\Sigma_{intern} = E\epsilon_s \tag{4.3}$$

4.4.1. Approach

During the various procedures of operation, the material of the plate is subjected to different phenomena, such as bending and point forces that result in stress concentrations. An overview of the procedures and phenomena that affect the plate are presented in Figure 4.16. First, the plate is mounted onto the GPHE and compressed by the outer pressure plates. This is done by tightening six bolts up to a certain applied moment. Creep occurs for polymers if the material is subjected to long-term loading, but it is considered to be inferior to the other phenomena due to the expected duration of the experiments. During operation, the operational pressure in the working fluid channel subjects the plate to bending where the windows of the outer pressure plate are located. Before filling the demo with ammonia, the system is placed in an almost vacuum state, where the corrugations of the stainless steel heat transfer plate are pressed onto the corrugated area of the visualization plate. This affects both the base plate and corrugation zone, but the stresses in the corrugation zone will be higher than in the base plate. The bending of the base plate during operations and stress concentrations in the corrugated zone in vacuum are identified as the most critical situations, indicated by orange and green boxes in Figure 4.16.

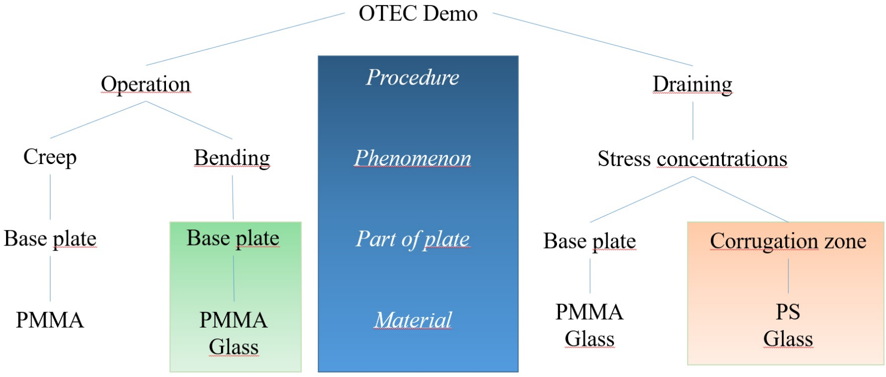

Figure 4.16: Schematic overview of OTEC procedures, occurring phenomena, geometry and material

Linear behaviour is expected to be accurate for the base plate of the visualization plate, since large displacements are unexpected in the GPHE during operational procedures. The shape of the corrugated zone however, does not allow for FEA to have accurate results due to the combinations of point forces, rounded corrugated shape and expected non-linear behaviour [2]. A large error is likely and therefore it is decided to test the corrugation zone physically by a work bench for PS. Accurate information on the behaviour of corrugated glass will remain unknown, and only the bending of the base plate for PMMA and glass is analysed with the FEA (indicated by the green box).

4.4.2. Mesh accuracy analysis

The accuracy of the solution depends heavily on the density of the mesh. Increasing the amount of elements generally increases the accuracy of the calculations. More elements results in more available nodes which gives a more precise outcome. It also results in smaller element sizes Δs which reduce the discretization error. The mesh quality also depends on aspect ratio, Jacobian and convergence. The quality of the outcome is dependent on the quality of the mesh.

Aspect ratio
The aspect ratio AR of an element is the ratio of the largest to the shortest edge of an element, which is unity for a equilateral tetrahedron. If the aspect ratio is large, the tetrahedral element no longer resembles the equilateral triangle, resulting into a larger calculation error. The system then tends to under predict the results. Decreasing the aspect ratio can be done by decreasing element size. A good mesh shows an average aspect ratio of $AR < 3.0$ [2].

Figure 4.17: Left) Aspect ratio of unity. Right) High aspect ratio

Jacobian
The Jacobian J is a square matrix containing all first order partial derivatives of a vector valued function. The Jacobian can be thought of as describing the amount of ‘transforming’, ‘rotating’ and ‘stretching’ that a local element is subjected to. A negative Jacobian means that element is self-intersecting or heavily distorted which leads to calculation errors. The amount of negative Jacobians is preferably zero.

Mesh convergence

Reducing the amount of elements in the mesh has a practical limit. A converged mesh gives no different values for a further decreased element size. If stress keeps rising during mesh refinement, the values are under predicting due to a too large element size. If after a certain decrease in element size the calculated stress remains the same, mesh convergence is reached. Finding the optimum where convergence is reached with the largest element size is done before the actual analysis to secure its accuracy and minimize the computational time.

Mesh accuracy
The entire plate including the base plate, corrugation zones and details is too complex to mesh without complications. Because the base plate is only investigated for a bending analysis, the corrugations and details are not relevant and therefore removed. A mesh analysis is performed for a plate thickness of 20 mm for both PMMA and glass. An operational pressure of 11 bar is applied to the inner side of the plate, while constraints are applied to the side where the stainless steel pressure plate with windows is pressed. The first principle stress is used as a reference for mesh refinement for glass and the Von Mises stress for PMMA.

Table 4.4: Mesh details and acquired stress per element size for bending

Δs *[mm]*	Elements	Nodes	AR_{max}	AR<3 [%]	J [%]	$\Sigma_{P,glass}$ [MPa]	$\Sigma_{VM,PMMA}$ [MPa]
12	8355	14667	3.2	100	0	5.7	2.76
8	25074	40259	3.75	100	0	5.76	3.14
6	49464	78148	9.8	100	0	6.1	4.2
4	172958	258183	4.4	100	0	6.7	4.9
3.5	285283	416225	4.8	100	0	6.5	4.8

Table 4.4 shows that 100% of the measured AR is below 3, while the maximum aspect ratio AR_{max} is 4.8. This seems contradicting, but the percentage is rounded up from 99.9 %. There is no negative Jacobian for the mesh, which reduces the chance on errors due to intersecting mesh elements. The maximum AR for Δs = 4 mm is 4.4. The aspect ratio plot shows a blue color in the region of interest which has an $AR \approx 1.7$ which is considered to be acceptable, see Figure 4.18. The Von Mises stress $\Sigma_{VM,PMMA}$ with Δs = 12 mm (8355 elements) is 1.7 times lower than for Δs = 3.6 mm (285283 elements), which is a significant difference and shows the importance of mesh convergence.

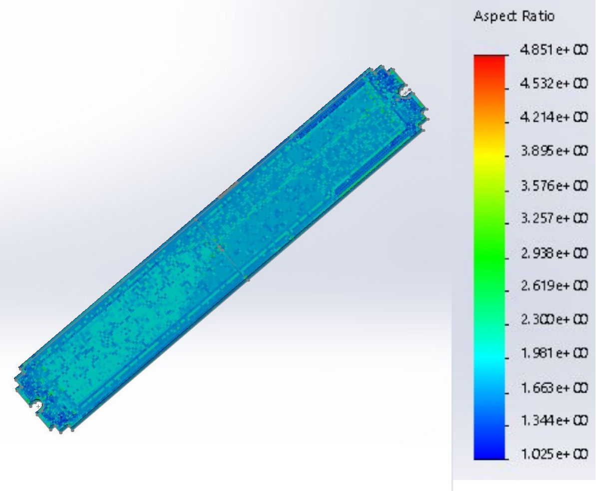

Figure 4.18: Aspect Ratio plot of chosen mesh for bending of PMMA

4.4.3. Pressures due to compression

For the failure diagnostics of the PMMA plate, it is investigated whether the PMMA plate withstands the tightening of the bolts during mounting. This analysis is not done for glass, since the compression strength is very high and the plate is more likely to collapse during bending. The visualization plate is pressurized by stainless steel pressure plates. The pressure is applied by six screws to which a certain torque τ is applied. The relation between the clamping force F_{clamp} and the applied torque τ is as follows:

$$F_{clamp} = \frac{\tau}{\mu_s D} \tag{4.4}$$

Where μ_s is the friction factor for a material combination of stainless steel and PMMA. According to the Engineering Toolbox [47], this friction factor lays between 0.4 and 0.5. The lower limit is taken for the cause of over-prediction. The outer diameter of the nut D is 16 mm. The required torque for the heat exchanger to have no leakages (without transparent plate) is expected to be 90 Nm. It is assumed for the heat exchanger including transparent plate that a torque in the same order of magnitude is necessary. An applied torque of τ = 100 Nm to the nuts located on the pressure plate is investigated. F_{clamp} is the force per screw. Six screws are tightened, and so the total force due to torque F_T is given by:

$$F_T = 6F_{clamp} \tag{4.5}$$

This results in a total force due to torque of F_T = 93.450 kN. The area of interest to which this force applies on the visualization plate is the total contact area between the steel heat transfer plate and the visualization plate. This area is measured with the Solidworks tool, A_c = 0.07 [m^2].

$$P_T = \frac{F_T}{A_c} \approx 13bar \tag{4.6}$$

Figure 4.19 shows the area, indicated with the blue color, where the compressive forces are applied.

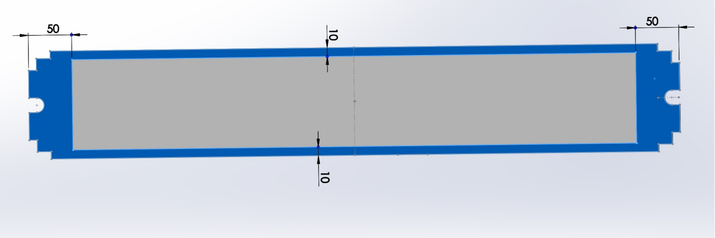

Figure 4.19: Area subjected to compressive forces

4.4.4. Pressures due to operation

The bending is evaluated for both PMMA and glass. On the location of the window, P_T = 0 and there is only an atmospheric pressure P_a. This means that the exerted pressure on the area of the window is equal to the condensation pressure P_c.

$$P_{bend} = P_c - P_{atm} \tag{4.7}$$

In Solidworks, the separation between the windows is removed to over-predict the situation, see Figure 4.20. The blue zone represents the zone where normally the windows are located, but are now formed into one big window with the same width. During the experiments, usually the condensation pressure is between 6 to 7 bar. For over-prediction, the pressure inside is chosen to be 12 bar. The pressure is evenly distributed over the plate.

4.4.5. FEA Results and conclusions

FEA results on glass
The maximum principle stress and displacement of glass due to bending under an operational pressure of 11 bar are shown in Table 4.5. The maximum principle stress $\Sigma_{P,glass}$ inside the glass base plate is 30.9 MPa and the maximum displacement ds = 9E^{-3} mm. If the operational pressure is brought down to 10 and 8 bar, the resulting stress is still higher than the reduced tensile stress (10.7 MPa) but below the initial tensile stress of glass (32.3 MPa).

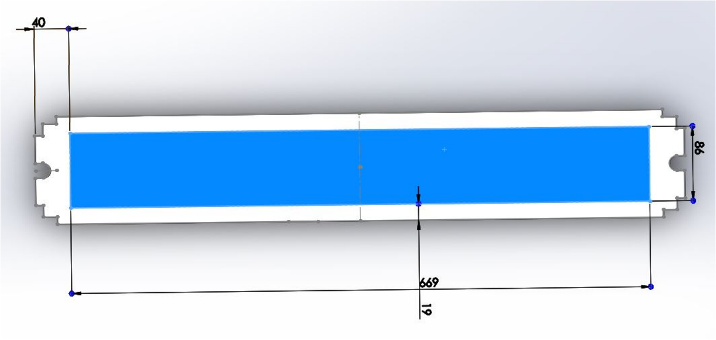

Figure 4.20: Area subjected to condensation pressure

Table 4.5: FEA results for glass and PMMA

Glass	$\Sigma_{P,glass}$ [MPa]	ds [mm]	*PMMA*	$\Sigma_{P,PMMA}$ [MPa]	ds [mm]
Bending @ $P_c = 12$ [bar]	30.9	$9E^{-3}$	Bending @ $P_c = 12$ [bar]	5.3	$2E^{-2}$
Bending @ $P_c = 10$ [bar]	25	$7.4E^{-3}$	Mounting @ $\tau = 100$ Nm	6.2	$2.48E^{-2}$
Bending @ $P_c = 8$ [bar]	18	$5.7\ E^{-3}$			

FEA results on PMMA
The maximum principle stress $\Sigma_{P,PMMA}$ and displacement ds of PMMA due to bending at an operational pressure of 12 bar and mounting are shown in Table 4.5. All stress values are below the reduced tensile strength of PMMA of 16.67 MPa and the deformation is considered acceptable.

Conclusions on FEA
The results presented by Solidworks for a pressure of 12 bar can be found in Appendix B. The FEA for glass shows that the performance during operation for various pressures is doubtful, as the internal stresses are below the initial tensile strength but above the reduced bending tensile strength. It is therefore advised not to use glass, as this simplified version of the plate does not include the corrugations and therefore does not say anything about crack formation due to point forces. According to the results of the FEA for PMMA, the plate did not fail due to mounting and operating the system. All internal stresses are below the reduced tensile strength and yield strength. This indicates that no failure or plastic deformation occurs for PMMA in the GPHE. PMMA is therefore considered to be a good material for the visualization plate in the GPHE with respect to mechanical performance.

4.5. Production and durability visualization plate

This section elaborates on the production of the PS/PMMA visualization plate, the difficulties along the way and its solutions. During the visualization experiments the plate showed material degradation after several days. The plate fatigue is reported and discussed.

4.5.1. Production of visualization plate

Material combination and geometry
Dahlgren [16] designed the geometry of the visualization plate in Solidworks (2018). This geometry is also used for producing the PS/PMMA plate. A more elaborate explanation on the geometrical modifications applied on the Solidworks model that were necessary for CNC-machining can be found in the thesis report of Dahlgren[16]. The maximum thickness of PS that could be delivered as a rectangular plate is 4.75 cm. Gluing multiple layers on top of each other is risky as it might reduce the transparency. Both PVC and PMMA can be delivered with a larger thickness of around 20 mm. The chemical resistance of PVC is higher than that of PMMA, but the delivery time of PVC would be much larger which is why PMMA is chosen for the base plate. It is assumed that PS would not penetrate the PS layer. PMMA with a thickness of 20 mm is chosen for the base plate. The layers are glued to each other and the PS layer is machined into the desired corrugation pattern by a CNC-machine.

Design alterations
The plate designed and produced by Dahlgren consisted out of two separate parts that were assembled after CNC-milling. The base plate included a chamber, where a thin corrugated PMMA layer was glued into that chamber. This was necessary for the CNC-machine to reproduce the Solidworks design as much as possible. However, the existence of the chamber inside the PMMA base plate showed to have an additional negative effect on the resistance once it is placed in the OTEC GPHE. The ammonia was able to penetrate through the sides of the corrugated layer and store behind the chamber, enhancing the material degradation locally. Therefore, it is decided for the PS/PMMA plate to machine the top layer of the base plate in one piece. The milling tool was therefore not able to produce the sharpest corners which lead to a more smooth geometric transition between the corrugated zone and base plate. However, the differences were very small and it is expected that this has no effect on the flow distribution and flow patterns.

Glue type selection
The glue that was used for the PMMA plate is two-component Anglosol which includes a hardener. Two tests are performed with 5 % hardener and 4 % hardener. The glue is designed for PMMA and worked very well for the PMMA/PMMA material combination, as no bubbles were visible in the glue layer. This glue was tested by the DEMO for its chemical resistance to ammonia and considered to have an acceptable resistance. Therefore, the same glue was used for the PS top layer and the PMMA plate. However, it became clear that this glue reacts different for the combination of PS/PMMA. The combination of the materials and this specific glue solution resulted in a significant amount of small bubbles and the formation of some large bubbles, see Figure 4.21 a).

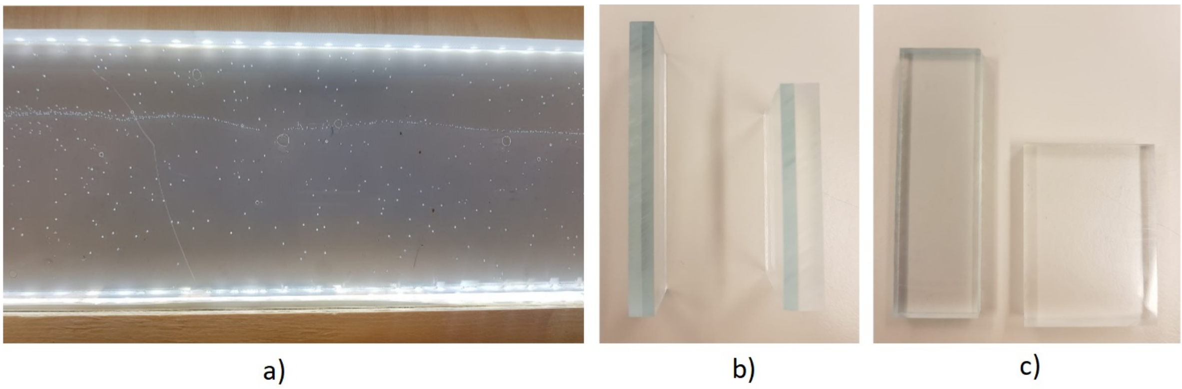

Figure 4.21: a) Bubble formation between PS and PMMA layer due to the use of Anglosol. b),c) Side and frontal view samples PS/PMMA with an UV hardener glue

For both tests, the resulting bubbles in the plate were considered to be unacceptable, as it is very unfortunate to have bubbles in a plate that is used for the observation of possibly bubbly flow. It is concluded that this type of glue is unfit for the PS/PMMA material combination. An UV-hardening glue DYMAX® type3099 is tested for the PS/PMMA combination. The benefit of the UV-hardener is that the timing of the curing process can be delayed and therefore the bubbles can escape from the glue layer to the ambient air. The glued samples are presented in Figure 4.21 b) and c), where no bubble formation is observed. The final plate does not contain bubbles, which proves that the application of this type of glue is successful for the assembly of PS onto PMMA. The downside of this glue is the lack of information about its chemical resistance to ammonia. Due to a lack of time the glue has not been tested, as material testing inside the OTEC demo is time costly. The application of this glue is discussed with all the members involved in the production of the plate and the risk is taken consciously, under the assumption that the pure ammonia will not penetrate the PS-layer.

Resulting visualization plate
Figure 4.22 shows the final result of the production of the PS/PMMA plate. The top right figure in Figure 4.22 shows the best transition from the PS layer to the PMMA base plate. The PS layer can be recognized by the blue haze. As expected, the plate shows a good optical quality. However, it is known that PS has a higher refractive index than PMMA. That, in combination with the corrugation patterns might distort the image that the plate is supposed to present. The plate is placed on top of a grid to present the difference in the actual image and the image that the plate shows, see Figure 4.23. The plate shows a distortion in the lines of the grid

by giving the lines a wavy slope, but the plate does not enlarge or decrease the size of the image. Only when the exact size of bubbles were to be measured, the distortion plays a role. For determining flow patterns or surface area void size, this distortion is considered to be acceptable.

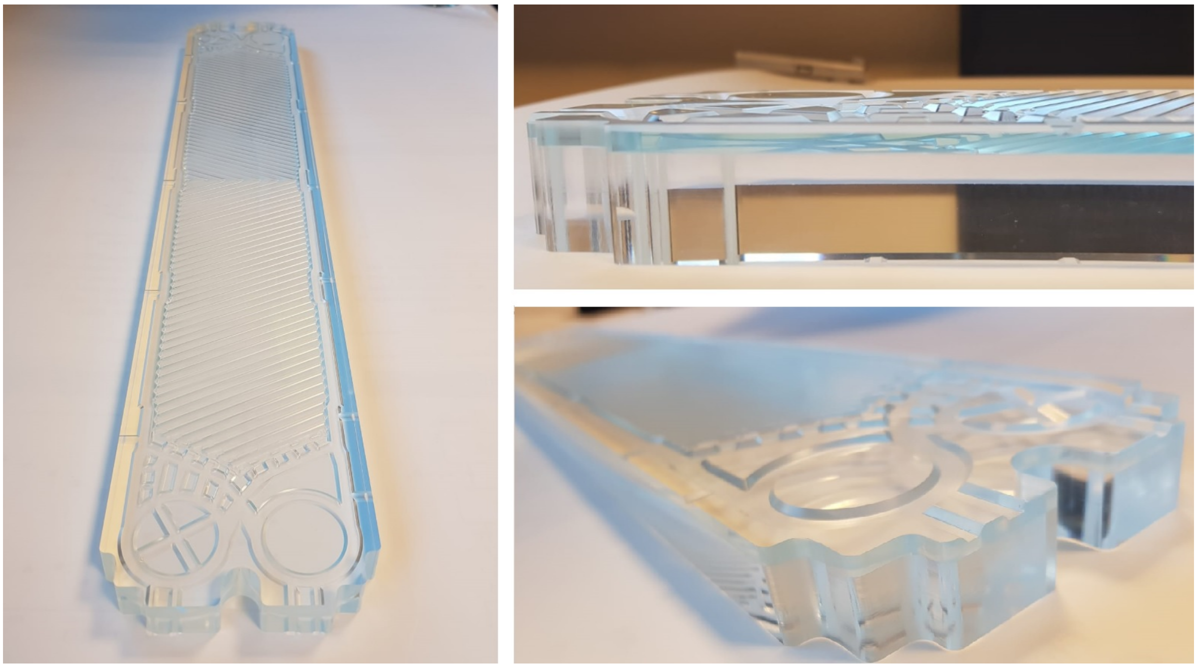

Figure 4.22: Final result of the produced plate. Left) Top view. Top right) Side view. Bottom right) Inlet/outlet zone

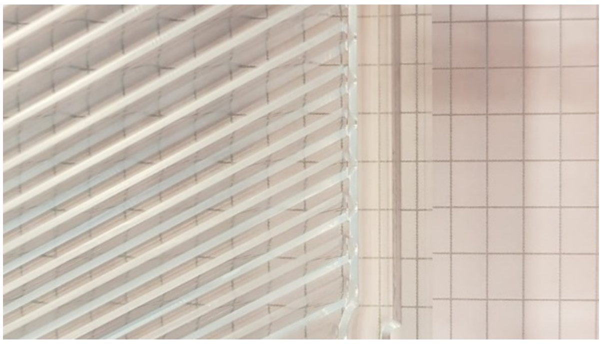

Figure 4.23: Plate placed on paper grid showing the transition of the grid image to a slightly distorted image of the grid by the PS/PMMA plate

4.5.2. PS/PMMA visualization plate fatigue

After seven days of operation, the PS/PMMA visualization plate started to degrade. Due to the various performed chemical tests, it was known that the plate would most probably remain intact for at least four days. After this time-span, there was no information on the durability of the plate. The first signs of degradation of the visualization plate were visible after 7 days of operation (including weekend). Very small crack-lines on some corrugations were observed. It is expected that the cracks were caused by ammonia absorption during the day and desorption of ammonia overnight when most of the ammonia turned into a liquid and sunk towards the liquid tank due to gravity.

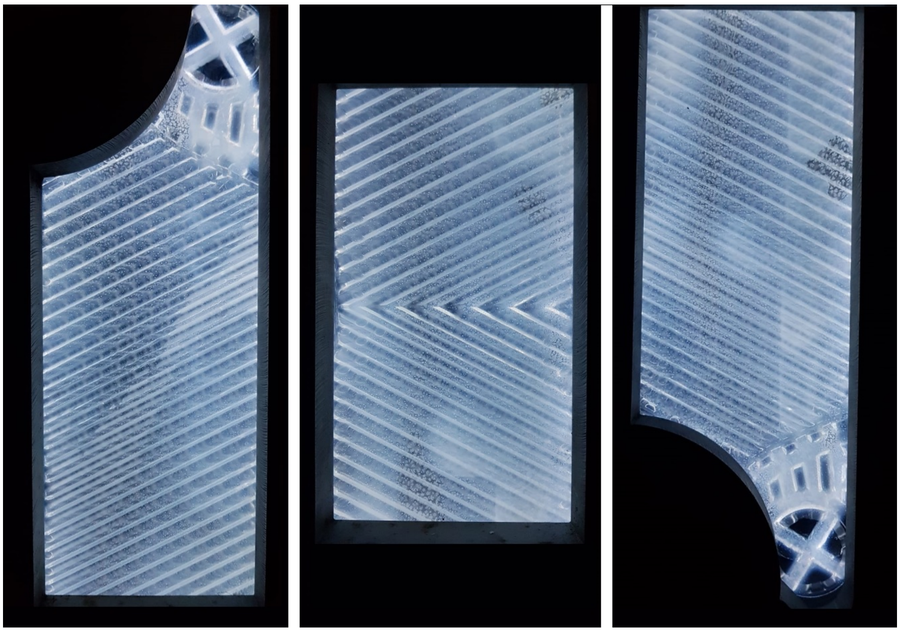

Figure 4.24: Crystal structured layer covering the visualization plate after 9 days of operation

After 9 days of operation, the crystal structures multiplied heavily and the sight decreased significantly. Some flow was still visible, but large patches became opaque, see Figure 4.24. Finally, the material turned fully opaque, see the most left figure of Figure 4.25. The plate fully lost its transparency, crack propagation was visible and the plate was no longer considered safe for operation. Due to the latter, the experiment was aborted.

Figure 4.25: Left) The degraded material after 12 days. Middle) Degraded material of inlet zone after dismounting the plate. Right) Degraded material of corrugated zone after dismounting the plate

Causes of the material degradation

It appeared that the crystal structures were located on the surfaces where the PS and PMMA were attached by glue. It seemed that the ammonia was slowly absorbed and had found a way to penetrate through the PS material until the glue layer. As no crystal formations were visible on the fatigued PMMA visualization plate produced by Dahlgren, it is expected that the formation of crystals is due to a chemical reaction between the penetrated ammonia and the glue. Finally, the crystal forming accumulated into an entire layer covering the surface of the PMMA. The plate was considered to be no longer of use and was dismounted. After removing the plate from the GPHE, the PS material formed large cracks and showed similar fatigue behaviour as the initial PMMA plate, see the middle and right images of Figure 4.25. What can be seen is that the PS layer shows no imprint, which means that the material does not soften over time due to the presence of ammonia. It does seem to get more brittle, as cracking behaviour was observed before dismounting. The plate did not show large material deformations, and the occurrence of leakages was absent.

4.5.3. Conclusions

From the production process and plate fatigue that was apparent during the visualization experiments, the following is concluded:

- Producing the corrugated and detailed structure of the polymer visualization plate by a CNC-machine proves to be a good method. The tolerances of the plate were sufficient and the plate caused no leakages in the GPHE.
- The UV-glue is an excellent glue for assembling PS to PMMA without the formation of any bubbles, but formed a chemical reaction with the penetrated ammonia and formed a crystal structured layer in between the materials that caused loss of transparency. It is therefore not advised to use this glue again for applications that involve ammonia and visualization purposes.
- PS is easy to machine, has a good optical quality and presents an acceptable image for flow visualization experiments.
- PS shows no clear signs of degradation with respect to mechanical performance. The material did not turn soft or rubbery when in contact with ammonia. However, the material does seem to become more brittle over time as cracks were observed on the corrugation patterns. No loss in strength is observed such as bending or material deformation.
- The durability of the plate is limited due to the chemical resistance of PS and the glue to ammonia as first material damage is observed after 7 days. The PS layer absorbed the ammonia slowly, which caused small cracks in the PS layer. It is not advised for safety reasons to use PS again for visualization studies that involve ammonia.

If in the future more research on flow visualization for pure ammonia is desired, more chemical tests are required on other polymers. A good start would be investigating the chemical resistance of transparent PP and PSU. If materials should be combined to form a plate with conform mechanical performance, research should be done to find a glue that forms no bubbles, does not lower the transparency and is chemically resistant to ammonia. At last, research can be done on surface coatings that can protect the PS material against the penetrating ammonia.

5

Flow visualization and analysis

This chapter elaborates on the performed experiments and analysis of the gained data. The main focus lays on the flow visualization experiments. First, the experimental approach and the relevance of the experiments are explained. Next,the observed flow path and flow patterns during the visualization experiments are presented and discussed. The recorded sensor data is used to gain the pressure drop, heat transfer coefficients and the volumetric void fraction. Image processing is performed to estimate the size of the surface area void that was apparent on the visualization plate. The volumetric and surface area void fraction are related to the heat transfer inside the GPHE. The dominant physical phenomena that influence the flow patterns are identified and a flow pattern map for downward condensing ammonia in the GPHE is proposed.

5.1. Experimental approach

This section discusses the two types of experiments that have been executed to obtain data to support the answers to the research questions formed in chapter 1. The first type concerns visualization experiments for a single channel configuration to investigate which flow patterns occur for various experimental conditions within the limits of the OTEC demo. The second type concerns multi-channel experiments with the purpose of gaining insight in the heat transfer and pressure drop and predicting the flow patterns for multi-channel configurations. The experimental approach used for the visualization experiments and multi-channel experiments is based on the approach used for the experiments performed by Tao. Tao performed single channel pure ammonia experiments on the original configuration of the GPHE in the OTEC demo. The experimental conditions of the single channel experiments by Tao are aimed to be repeated in the flow visualization experiments and the multi-channel experiments.

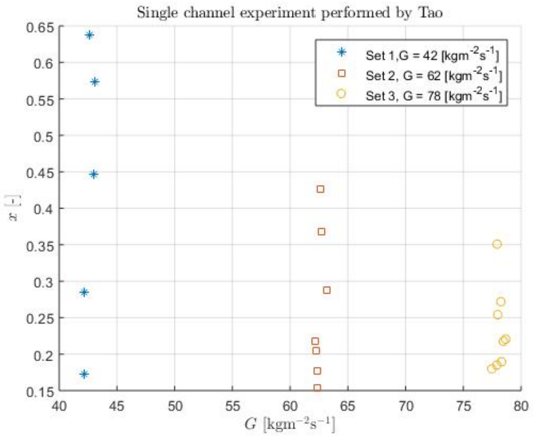

Figure 5.1: Experimental sets of the single channel experiments performed by Tao

Figure 5.1 shows three sets of the series of experiments performed by Tao. A set is referred to as a series of experiments where the mass flux G is kept constant while varying the inlet vapor quality of the two-phase flow in the GPHE, see Figure 5.1. A subset is referred to as one of these data points within a set where both G and x are constant. Every subset is executed during steady-state conditions for a duration of 10 minutes, and contains the average values of the sensor data for this time-span. The same approach is applied for the multi-channel experiments but for lower mass fluxes.

5.1.1. Experimental conditions of the flow visualization experiments

In the visualization experiments, five different sets are performed in a single channel arrangement. For every set, the mass flux G was kept constant while the inlet vapor quality x_i in the GPHE is increased. The most relevant experimental conditions of the visualization experiments are presented in Table 5.1. Here, G is the mass flux of the ammonia, P_c is the average condensation pressure inside the ammonia channel, x is the average vapor quality, $T_{W,i}$ is the cold water inlet temperature and $\dot{m}_W$ is the mass flow rate of the cold water side in the GPHE.

Table 5.1: Experimental conditions of the single channel visualization experiments, including one ammonia channel, one cold water channel and one effective heat transfer plate

	G [kgm^{-2}s^{-1}]	x range [-]	P_c [kPa]	$T_{W,i}$ [°]	$\dot{m}_W$ [kgs^{-1}]
Set 1	43	0.23 - 0.62	685	10	0.071
Set 2	64	0.2 - 0.43	685	10	0.069
Set 3	81	0.18 - 0.31	680	10	0.09
Set 4	88	0.25 - 0.29	710	10	0.065
Set 5	91	0.27 - 0.28	700	10	0.097

As can be seen from Table 5.1, the vapor quality range differs per set. For a lower mass flux, the average vapor quality range is larger. This is due to the limits of the system. With increasing ammonia mass flux G, it took much longer for the temperature of the hot water tank to stabilize. If during the experiment this temperature did not stabilize within an acceptable amount of time, it was considered that the upper limit of the quality range was reached. The lower limit of the quality is reached when the liquid level in the storage tank located before the process pump decreased without stabilizing. This phenomenon is more limiting for higher mass fluxes, which explains the smaller vapor quality ranges for these sets. The table shows that the cold water inlet temperature has been stable at 10 °C, while the cold water mass flow rate strongly varies.

5.1.2. Experimental conditions of the multi-channel experiments

These experiments do not include visualization and the GPHE is in its original configuration. Three sets are performed for the multi-channel experiments for a channel arrangement with two ammonia channels and three cold water channels, see Table 5.2. Instead of one effective heat transfer plate, four are present in these experiments. The ammonia channels are now condensing on both sides of the channels, where for the single channel experiments performed by Tao and for the visualization experiments the channel was cooled from only one side.

Table 5.2: Experimental conditions of the multi-channel experiments, including two ammonia channels, three cold water channels and four effective heat transfer plates

	G [kgm^{-2}s^{-1}]	x range [-]	P_c [kPa]	$T_{W,i}$ [°]	$\dot{m}_W$ [kgs^{-1}]
Set 1	21	0.40 - 0.56	685	10	0.16
Set 2	31	0.16 - 0.35	672	10	0.14
Set 3	40	0.18 - 0.28	680	10	0.145

High and low mass fluxes are difficult to stabilize in the OTEC demo, which explains the varying range of vapor qualities in the table. The cold water mass flow rate $\dot{m}_W$ is much higher than for the visualization experiments due to a lower pressure drop over the cold water side. Because the cold water is now distributed over three channels, the liquid encounters less resistance in the channels because the flow passage area through the water channels is now three times larger.

5.1.3. Discussion of relevance

The experimental approach is the same as used by Tao on his previous previous single channel experiments with the GPHE. The single channel experimental conditions by Tao will be compared to those of the visualization experiments. This is done to investigate the influence of the modifications to the GPHE to allow for the visualization experiments.

The visualization experiments will give information on how the flow configuration and identified flow patterns relate to the performance of the GPHE. In the future, OTEC will install large multi-channel heat exchangers in their OTEC plants. It is therefore useful to discuss the new multi-channel heat transfer and pressure drop results and compare these to the single-channel configuration. At last, the expected flow pattern in the multi-channel configuration is discussed based on the behaviour of the HTCs with respect to varying vapor quality and mass flux.

5.2. Observations flow visualization

Three windows were visible over the length of the plate: the top, middle and bottom windows, see Figure 5.2. All windows showed different phenomena as the vapor condenses over the length of the plate. For every subset (an experiment of 10 minutes with a constant G and x), approximately 500 frames with a frame rate of 3000 fps are shot for all the windows. This section gives an elaborate explanation of the visual observations. At last, a schematic overview of the approach for data-reduction is proposed.

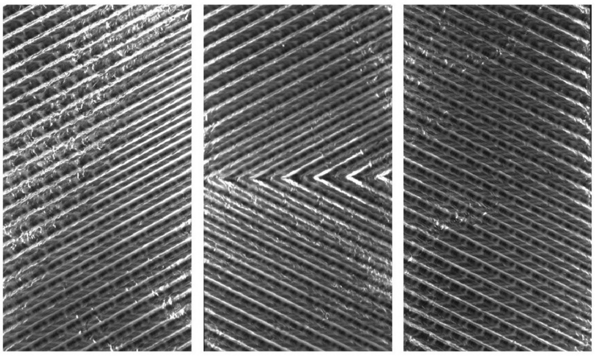

Figure 5.2: Left) Top window. Middle) Middle window. Right). Bottom window

5.2.1. Flow path

The flow path is the path over the width and length of the plate where the vapor or the liquid flows along. It is observed that the flow path of the liquid and the vapor are significantly different, especially for the top window when a large fraction of the vapor is still present. This phenomenon is widely known as separated flow. Due to the geometry of the distribution zone at the top of the channel, most of the liquid is pushed to flow over the upper diagonal of the top window. A rough liquid flow was easy to detect since it showed the most light reflections in all directions. The bottom diagonal of the top window is mostly covered in smooth liquid flow for high mass fluxes, indicated by a clear image without light reflections. For lower mass fluxes, an opaque (static) surface was visible, indicating the flow of the vapor phase that studded the window. A small liquid rough zone on the bottom right corner of the top window was seen for most mass fluxes. It was also observed that a significant amount of liquid flows along the sides of the window, which cannot be seen by the camera since the path of that liquid flow is located behind the stainless steel pressure plate.

Figure 5.3 shows the three windows of the plate, where the path of the rough liquid flow is indicated by the red arrows. The rest is either smooth film flow or a surface void area. The flow in the middle window showed less separated flow characteristics as compared to the top window. Halfway the middle plate, the direction of the corrugations switches, which changes the flow direction causing the liquid to evenly distribute along the width in the lower half of the middle window. The middle and bottom window gave a clear image for all sets indicating that the visualization plate surface was covered with a liquid film entirely. However, the outlet

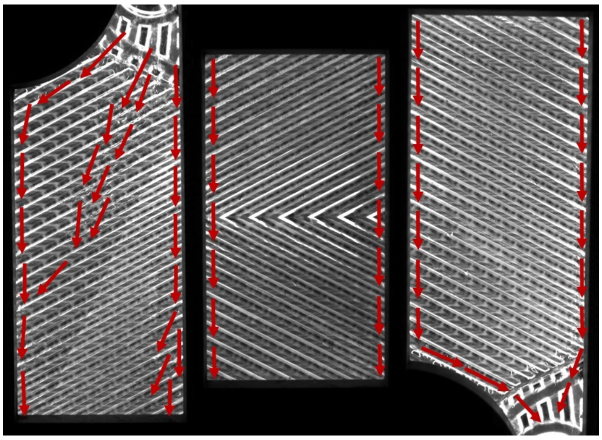

Figure 5.3: Top (left), middle (middle) and bottom window (right) where the path of the rough liquid flow is indicated by red arrows

vapor quality was not zero for any of the subsets. This means that vapor is still present in the middle and bottom window but not visible due to the evenly distributed liquid film on the visualization plate.

5.2.2. Flow patterns

For all performed sets and subsets, no bubbles, slugs or churns were observed within the visualization experiments. For sets 1 and 2, which contain a lower mass flux, partial film flow is observed. The opaque surface described in the previous subsection is known as dry-out. The amount of liquid film covering the visualization plate is not enough to cover the plate entirely, causing some spots on the plate that have direct contact to the vapor phase. Partial film flow is characterized by dry-out spots on the heat transfer surface. An example of a dry-out zone, which is in study referred to as a surface area void, is shown in Figure 5.4 and Figure 5.5. The area inside the black borders represents the surface area void, small light reflections outside the border indicate rough liquid flow, and a clear image indicates smooth liquid flow.

Film flow was observed for set 3, 4 and 5. These sets contain a higher mass flux and a smaller range of vapor quality. Film flow was identified by the occurrence of clear surface areas that both contained rough and smooth liquid flow, and the absence of surface area voids. For the lowest mass flux, smooth liquid flow is observed, which transitioned to rough liquid flow with increasing mass flux G. The behaviour of the vapor phase could not be observed due to either a studded window in case of dry-out, or the liquid film blocking the vision to the vapor ammonia flow. The top window shows most significant change in flow configurations for various conditions as compared to the middle and bottom window. For this reason, only the top window is used for further analysis.

5.2.3. Influence of mass flux on flow configuration

The images of subsets with an average vapor quality of 0.20 (or close to 0.20) are compared for increasing mass flux, see Figure 5.4. From Figure 5.4 it can be seen that for a lower mass flux of $G = 43\ \mathrm{kgm^{-2}s^{-1}}$, a small rough liquid film area is present right below the inlet zone of the plate. For $G = 64\ \mathrm{kgm^{-2}s^{-1}}$, the rough zone below the inlet zone has increased and spreads out over the diagonal of the top window. For $G = 81\ \mathrm{kgm^{-2}s^{-1}}$, also a rough film zone is observed at the bottom right of the top window.

The surface area void for $G = 43\ \mathrm{kgm^{-2}s^{-1}}$ covers almost entirely the lower diagonal of the top window, but decreases significantly for $G = 64\ \mathrm{kgm^{-2}s^{-1}}$, and vanishes for $G = 81\ \mathrm{kgm^{-2}s^{-1}}$. Figure 5.5 shows for $x = 0.31$ and increasing mass flux a larger surface area void for a mass flux of 43 and 64 $\mathrm{kgm^{-2}s^{-1}}$ with respect to Figure 5.4. For the highest mass flux, no surface area void is present. A higher mass flux leads to an increase of the rough film flow area, and therefore a higher pressure drop is expected. An increasing mass flux reduces surface area voids significantly.

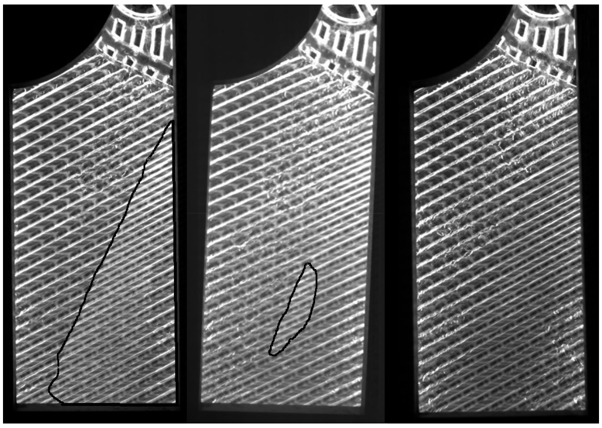

Figure 5.4: $x = 0.20$. Left) $G = 43$ kgm^{-2}s^{-1}. Middle) $G = 64$ kgm^{-2}s^{-1} Right) $G = 81$ kgm^{-2}s^{-1}

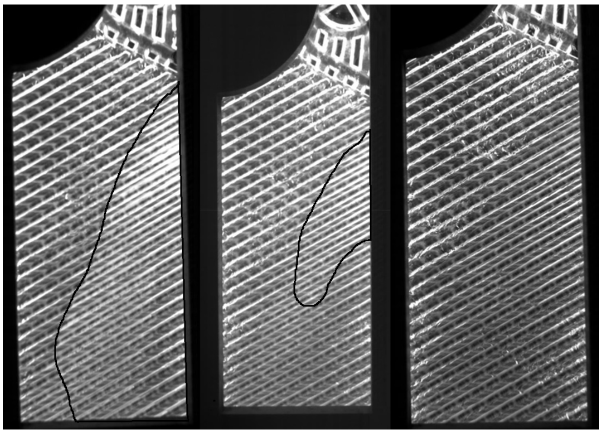

Figure 5.5: $x = 0.31$. Left) $G = 43$ kgm^{-2}s^{-1}. Middle) $G = 64$ kgm^{-2}s^{-1} Right) $G = 81$ kgm^{-2}s^{-1}

5.2.4. Influence of vapor quality on flow configuration

The influence of the average vapor quality x on the flow configuration was best seen for the lowest mass flux. First of all, this is due to the fact that high vapor qualities could not be tested for the higher mass flux sets since the limits of the OTEC demo did not allow for it. However, surface area voids have been observed for even the lowest vapor qualities at the low mass flux, indicating that mass flux does have a significant influence in the transition from partial film flow to film flow.

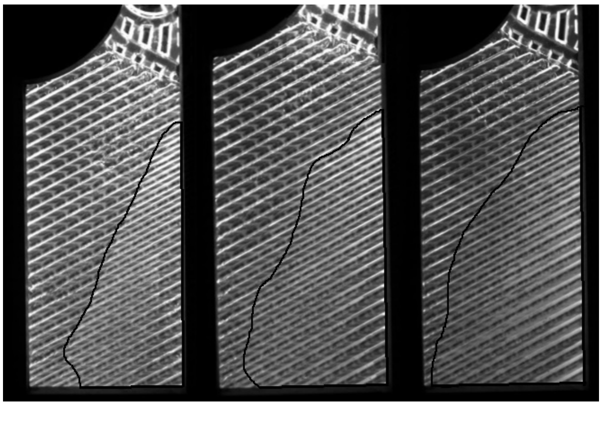

Figure 5.6: $G = 43$ kgm^{-2}s^{-1} Left) $x = 0.22$. Middle) $x = 0.48$. Right) $x = 0.62$.

In Figure 5.6 the flow configurations are shown for an increasing vapor quality at a constant mass flux of 43 $\mathrm{kgm^{-2}s^{-1}}$. For $x = 0.22$, a large surface area is already present. The upper diagonal gives a clear image without a lot of light reflection, indicating a partial film flow with a smooth liquid layer. For a vapor quality of 0.48, it can be seen that the clear upper diagonal has shifted upwards and that the surface area void has spread out. For a vapor quality of 0.62, again the surface area void has increased. The vapor quality has a strong influence on the growth of the surface area void if the mass flux is unchanged. For a high mass flux, the influence of x is unknown since high vapor qualities were not possible to test.

5.2.5. Approach for data processing

Flow patterns, heat transfer, pressure drop and void fractions are expected to be related. Figure 5.7 gives an overview on how the data is processed. During the visualization experiments, the sensor values are recorded and saved by Labview. At the same time, flow movies and pictures are recorded for every subset and stored. The sensor data gives insight in the HTCs and pressure drop. The camera data gives insight in the behaviour of the vapor, liquid and for which circumstances certain flow patterns occur. The observed flow patterns can be compared to the flow pattern maps proposed by previous studies and conclusions can be drawn on the accuracy of these flow pattern maps. A flow pattern map specifically for the GPHE geometry and experimental conditions can be created. The volumetric void fraction ϵ is generally used for modelling and plays an import role in determining the pressure drop and other important factors and can be calculated using proposed models by previous studies. By image processing of the images taken in the visualization experiments, the surface area void fraction ϵ_A can be determined and investigated if it is related to the volumetric void fraction. The surface area void fraction can be related to the flow pattern map that is generated for the experimental conditions of the visualization experiments, and compared to the behaviour of the ammonia and overall HTCs. By analysing dimensionless numbers (Re, We, Co, Ga), dominant physical phenomena can be recognized that might be related in the occurrence of the varying flow patterns. Conclusions can be drawn on the relation between the flow patterns and performance of the GPHE. Finally, by comparing the results from the visualization experiments to the new heat transfer and pressure drop data from the multi-channel experiments predictions can be made on the occurring flow patterns for the multi-channel configuration.

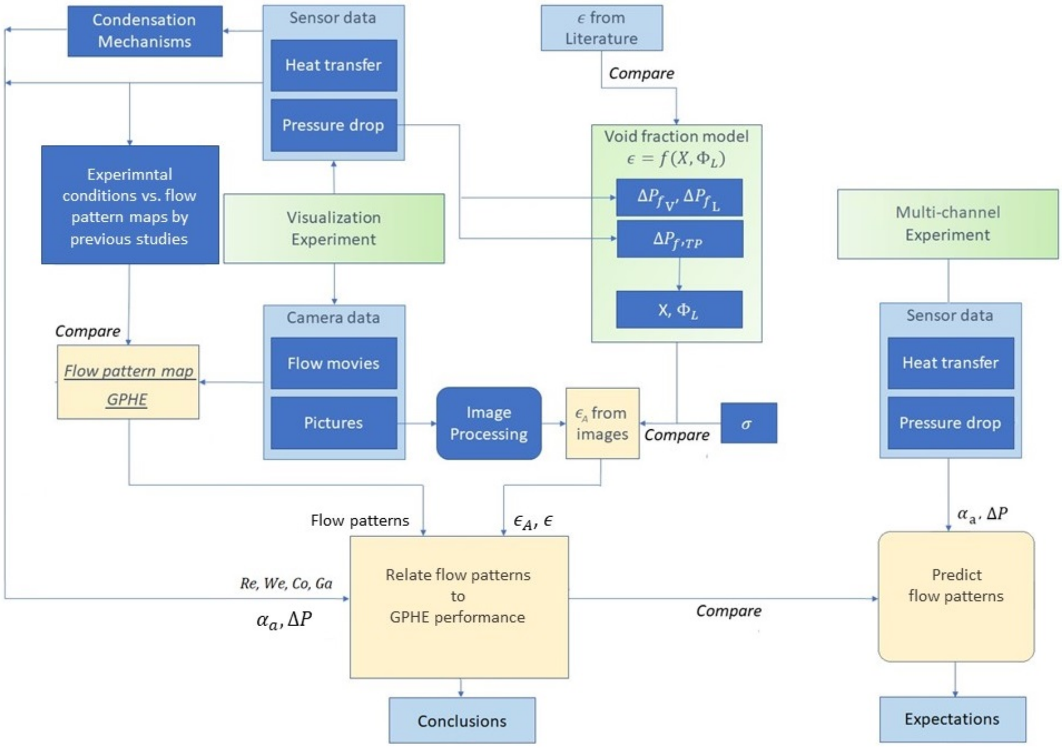

Figure 5.7: Flow diagram for processing the data of the visualization experiments and multi-channel experiments

5.3. Heat transfer and pressure drop

In this section, the HTCs and pressure drop are determined for the visualization experiments and compared to the observed flow patterns. Second, it is investigated what the influence is of the LED-strip, insulation and adjusted geometry of the GPHE which were necessary for allowing flow visualization. The HTCs and pressure drop of the multi-channel experiments are determined and compared to those of the visualization experiments.

5.3.1. Pressure drop of visualization experiments

It is expected that the pressure drop and the flow patterns are related. The total pressure drop in the GPHE on the ammonia-side is measured by a pressure differential sensor, that measures the pressure difference directly. The frictional two-phase pressure drop takes up most of the total pressure drop. The frictional two-phase pressure drop is relevant for determining the two-phase parameter Φ_L which is used for determining the volumetric void fraction. The latter is discussed in section 5.4.

Total pressure drop ammonia side

The inlet pressure is measured in the piping right before the inlet port of the GPHE and the outlet pressure is measured in the piping right after the outlet port. ΔP_{exp} is the total pressure drop measured by the differential sensor during the experiments. The total pressure drop per meter length is presented in Figure 5.8. From the figure it can be seen that the pressure drop increases with mass flux. Second, increasing mass flux corresponds to a steeper slope of the pressure drop. Evidently, film flow corresponds to a higher pressure drop because film flow is only observed for high mass flux. The figure shows that for a constant mass flux, the pressure drop increases with vapor quality. Pressure drop increase due to increasing quality has a stronger effect for higher mass flux. For G = 91 kgm^{-2}s^{-1}, the pressure drop of the second subset with a higher vapor quality is lower, this is due to the fact that the average mass flux is taken of those two points. The first point is close to 92 kgm^{-2}s^{-1} and the second to 90 kgm^{-2}s^{-1}, which explains the drop instead of increase.

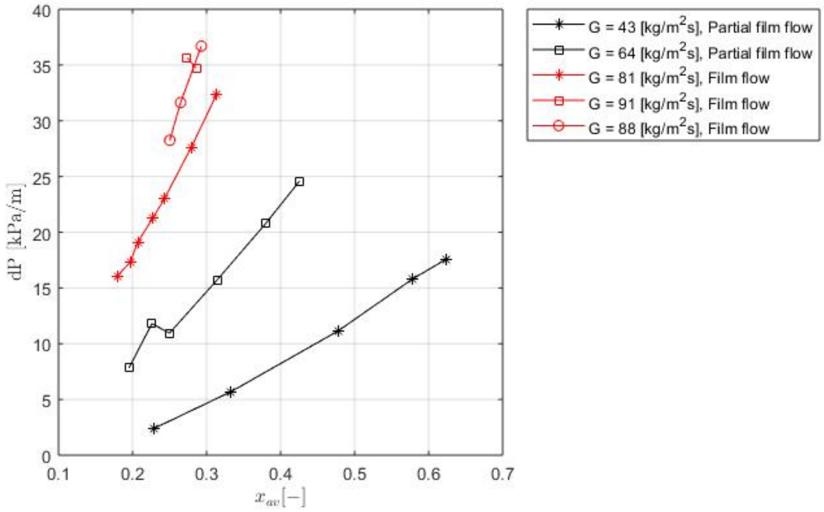

Figure 5.8: Total pressure drop ΔP_{exp} per meter length for every experimental set versus average vapor quality x

Two-phase frictional pressure drop ammonia side

To determine the two-phase frictional pressure drop $\Delta P_{f,TP}$ on the ammonia side of the condenser, the method described by Tao et al. [44] is used. Pressure drop components are subtracted from the measured total pressure drop ΔP_{exp}, see Equation 5.1. It is expected that some pressure is lost when the fluid passes through the in- and outlet ports, $\Delta P_{i,port}$ and $\Delta P_{o,port}$. Liquid ammonia originating from the recuperator is sprayed through small holes into the ammonia vapor line before entering the inlet port. A pressure drop is expected due to mixing of the liquid and vapor ammonia before entering the GPHE, ΔP_{mix}. During condensation, a minor pressure rise is also expected. The vertical downward flow creates a liquid column, which is described by the elevation pressure ΔP_{ele}. The fluid also decelerates during condensation and creates a pressure rise ΔP_{de}.

$$\Delta P_{f,TP} = \Delta P_{exp} - \Delta P_{i,port} - \Delta P_{o,port} - \Delta P_{mix} + \Delta P_{de} + \Delta P_{ele} \tag{5.1}$$

The pressure drop in the inlet and outlet ports are defined by Collier and Thome [15], see Equation 5.2 and 5.3. The relation is based on a sudden contraction and sudden enlargement of the cross-sectional area of the tube, which is the case for the port inlet and outlet. It is most likely that separated flow occurs but it is expected that the method for a homogeneous flow is still applicable. Wall shear and gravitational forces are ignored and Equation 5.2 is proposed.

$$\Delta P_{i,port} = G_{tube}^2 v_L \frac{A_{tube}}{A_{port}}(1 + \frac{v_V - v_L}{v_L} x) \tag{5.2}$$

The same approach by Collier and Thome [15] is used for two-phase separated flow passing through a sudden contraction, which is the case for the outlet port. During contraction, the flow is accelerated and pressure energy is mostly converted to kinetic energy (viscous dissipation is neglected). The coefficient of contraction C_c represents the liquid cross-sectional area at the contraction over the liquid cross-sectional area downstream in the smaller tube. Perry et al. [40] present a table for coefficients of contraction C_c for certain tube enlargements, and the proposed values are interpolated to a value of $C_c = 0.592$ for the contraction in the outlet port.

$$\Delta P_{o,port} = 0.5 G_{tube}^2 v_L (\frac{1}{C_c} - 1)^2 (1 + \frac{v_V - v_L}{v_L} x) \tag{5.3}$$

G_{tube} is the ammonia mass flow rate divided by the cross-sectional tube area of the liquid line A_{tube}. A_{port} is the cross-sectional area of the inlet/outlet ports. The mixing pressure drop is proposed by Jankowski et al. [25] and defined by Equation 5.4:

$$\Delta P_{mix} = 0.5 u_{ori}^2 \rho_L (1 - \frac{d_{ori}}{d_{tube}}^4) f_{com} \tag{5.4}$$

Where u_{ori} is the velocity of the liquid ammonia flowing through the small orifices with a diameter d_{ori} of 1 mm, d_{tube} represents the diameter of the tube. A semi-empirical model for the discharge coefficient for flow through orifices of arbitrary length-to-diameter ratio is developed by Jankowski et al. [25]. The total pressure drop through the orifice is treated as a pressure drop through a sharp-edged orifice and a pressure drop for developing flow along the walls of the orifice. The first term f_{edge} of Equation 5.5 represents the discharge coefficient for the sharp-edged orifice. The second term f_{lam} represents the friction factor for a smooth developing flow. Together, they form the overall discharge coefficient f_{com} for flow through orifice tubes.

$$f_{com} = f_{edge} + f_{lam} \tag{5.5}$$

$$f_{edge} = \frac{25}{9}(1 + e^{(-.12\sqrt{Re_{L,ori}})} - 2.16 e^{-0.26\sqrt{Re_{L,ori}}} + 0.16(1 - \frac{\sqrt{Re_{L,ori}}}{1 + \sqrt{Re_{L,ori}}})^{-2}) \tag{5.6}$$

$$f_{lam} = \frac{4}{Re_{L,ori}} \frac{L_{ori}}{d_{ori}} (\frac{3.44}{\sqrt{\zeta}} + \frac{16 + 0.3125\zeta^{-1} - \frac{3.44}{\sqrt{\zeta}}}{1 + 2.12 * 10^{-4}\zeta^{-2}}) \tag{5.7}$$

The Reynolds number in the orifice (small holes) in the liquid line $Re_{L,ori}$ and ζ are proposed by Jankowski et al. and defined by Equation 5.8 and 5.9:

$$Re_{L,ori} = \frac{\rho_L u_{ori} d_{ori}}{\mu_L} \tag{5.8}$$

$$\zeta = \frac{L_{ori}}{d_{ori} Re_{L,ori}} \tag{5.9}$$

The deceleration pressure rise ΔP_{de} and the elevation pressure rise ΔP_{ele} proposed by Collier and Thome [15] are defined by equations 5.10 and 5.11, based on the two-phase homogeneous model.

$$\Delta P_{de} = G^2(v_V - v_L)(x_i - x_o) \tag{5.10}$$

$$\Delta P_{ele} = \rho_{av} g L_p \tag{5.11}$$

Where $\rho_{av} = \frac{1-x_{av}}{\rho_L} + \frac{x_{av}}{\rho_V}$.

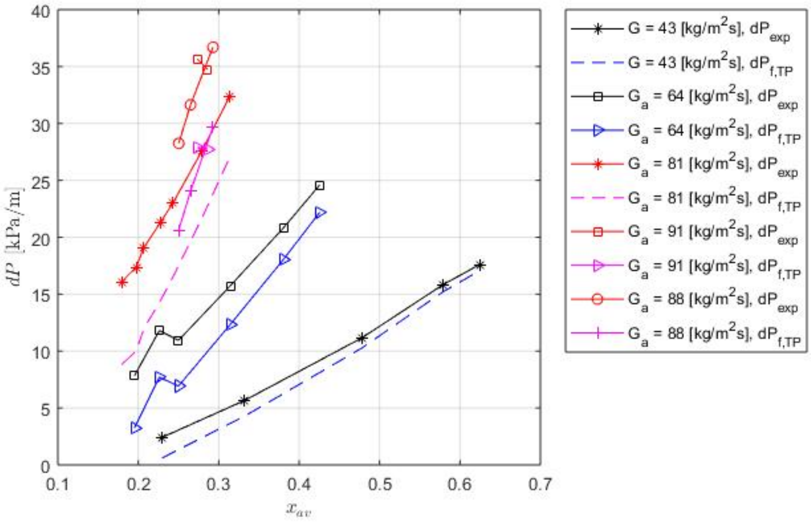

Figure 5.9: Total pressure drop ΔP_{exp} and two-phase frictional pressure drop $\Delta P_{f,TP}$ per meter length for every experimental set versus average vapor quality x

The two-phase frictional pressure drop and total pressure drop are presented in Figure 5.9. The results show that indeed the two-phase frictional pressure drop takes up most of the total pressure drop. For higher mass flux G, the difference between the total pressure drop and frictional pressure drop enlarges. Mostly, this is due to the mixing pressure drop. For higher mass flux, the velocity u_{ori} is large due to the small diameter it flows through, and increases quadratically. Therefore, the increased difference is not unexpected.

5.3.2. Heat transfer of visualization experiments

As is discussed in the literature review, the heat transfer behaviour is dependent on the condensation mechanisms. Longo et al. [33],[34] proposed a transition value of 1650 for the Reynolds equivalent number Re_{eq}. For the visualization experiments, the minimum $Re_{eq} = 2800$, it is therefore expected that the condensation mechanism is convective condensation. This regime is expected to be dominated by turbulence and shear, and the thermal resistance of the liquid film is reduced due to a reduced film thickness. It is expected that the HTCs increase with increasing mass flux. In this section, the HTCs of the pure ammonia and the overall HTCs inside the GPHE during visualization are determined and compared to the various sets and observed flow patterns.

HTCs cold water side

Tao et al. [44] performed water/water experiments to obtain single-phase HTCs and Fanning friction factors. Tao et al. used the generally accepted form of Equation 5.12, where θ_1 and θ_2 are dependent on the geometry of the heat exchanger and calculated by the Wilson-plot method. Tao et al. [44] proposed $\theta_1 = 0.275$ and $\theta_2 = 0.7$.

$$Nu_W = \frac{\alpha_W d_h}{\kappa_W} = \theta_1 Re_W^{\theta_2} Pr_W^{(1/3)} \tag{5.12}$$

Finally, the following correlation for the water side HTC, α_W can be determined for $320 < Re_W < 2600$:

$$\alpha_W = 0.275 \frac{\kappa_W}{d_h} Re_W^{0.7} Pr_W^{1/3} \tag{5.13}$$

HTCs ammonia side

The enthalpies of the inlet and outlet of the ammonia side GPHE and the inlet and outlet vapor qualities are determined by the energy balance method described in section 3.2.4. It is also assumed that there is no heat loss to the environment and that the heat transfer due to the temperature of the LED-strip is negligible. Furthermore, it is assumed that the two-phase inlet enthalpy of the after cooler is equal to the outlet enthalpy of the GPHE. Now that the cold water side HTC α_W and required enthalpies are known, the heat transfer rate $\dot{Q}$ of the GPHE can be determined, see Equation 5.14.

$$\dot{Q} = \dot{m}_a(h_{a,i} - h_{a,o}) = UA_{eff} \frac{(T_{a,i} - T_{W,o}) - (T_{a,o} - T_{W,i}))}{ln \frac{T_{a,i} - T_{W,o}}{T_{a,o} - T_{W,i}}} \tag{5.14}$$

Where U is the overall HTC and is defined by Equation 5.15:

$$U = \frac{1}{\frac{1}{\alpha_a} + \frac{d_p}{\kappa_s} + \frac{1}{\alpha_W}} \tag{5.15}$$

Finally, the HTC on the ammonia side α_a of the GPHE is the only unknown left in the equations and can therefore be determined. The overall HTCs and the ammonia HTCs are presented in Figure 5.10 for average vapor quality x (left) and liquid Reynolds number Re_L (right). The red data-points indicate film flow, and the black data-points indicate partial film flow.

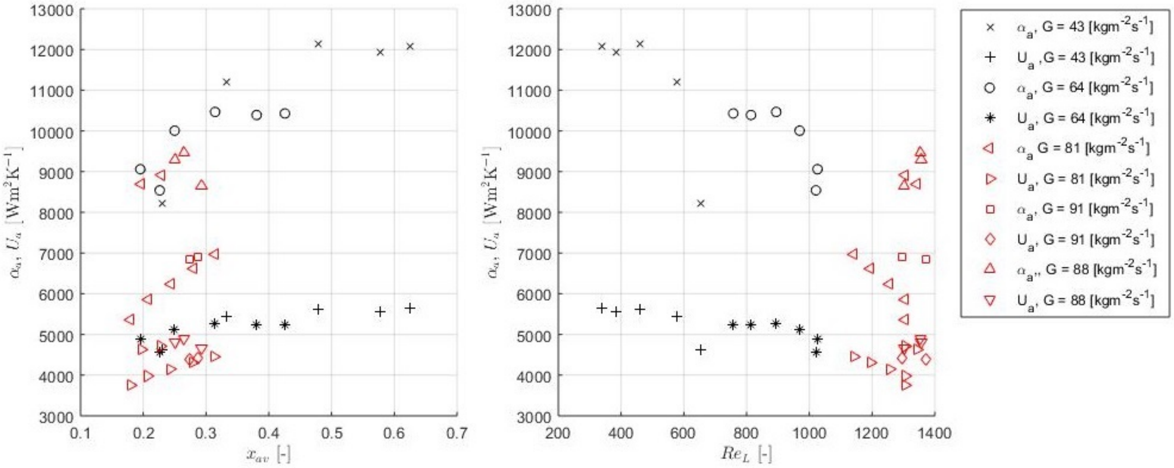

Figure 5.10: HTCs of the visualization experiments. Left) HTCs vs. vapor quality x. Right) HTCs vs, the liquid Reynolds number Re_L

Effect of vapor quality on HTCs

The left figure shows that the ammonia HTCs α_a increase with vapor quality. There seems to be a different slope for the HTCs with increasing vapor quality for partial film flow than for film flow. Film flow, indicated by the red points, show more linear characteristics for increasing vapor quality. Partial film flow shows at first a strong increase in HTCs but then stabilizes at a constant value with increasing x. This effect is best seen in the right figure, where the partial film flow HTCs stabilize around α_a = 12000 Wm^{-2}K^{-1} for G = 43 kgm^{-2}s^{-1}, and around α_a = 10500 Wm^{-2}K^{-1} for G = 64 kgm^{-2}s^{-1}. For partial film flow, it is known that a surface area void is present on the heat transfer plate which might have a negative effect on the heat transfer and be the cause of the decay in the slope of the HTCs. The figure does not give insight in the size of the surface area void, but it is expected to grow with increasing vapor quality. Therefore, the relation between the increase of the surface area void fraction ϵ_A and the HTCs is discussed in section 5.4.7.

For G = 64 kgm^{-2}s^{-1} and x = 0.22 no void was observed. It is expected that this is due to the fact that this subset is executed on another day, after a set with a high mass flux. This means that the entire surface was already wetted, and therefore it remained entirely wet even though the mass flux was decreased. This point shows a lower HTC as compared to the points that contain a surface area void inside the set, but this might be due to the fact that the set is executed on another day and therefore has slight different experimental conditions.

Effect of mass flux on HTCs
Increasing the mass flux has an effect, but is a little harder to distinguish because there are not many data points with the same vapor quality and different mass flux. Second, the cold water mass flow rate is not the same for every set, which influences the HTCs. However, when looking inside the same set for G = 81 kgm^{-2}s^{-1}, the left figure shows a significant higher α_a for x = 0.2 and x = 0.22. This jump is due to the fact that for these two points, the mass flux approached 82 rather than 81. It seems that the HTCs increase with mass flux for the conditions where the other parameters are kept constant.

It is expected that HTCs increase with vapor quality and mass flux. The best heat transfer performance is expected for a high mass flux and high vapor quality. If the inertia of the mass flux is high enough, film flow is expected even for higher vapor qualities. Therefore, film flow is expected to have the best heat transfer performance.

5.3.3. Influence of the modified GPHE setup for visualization experiments

By comparing the heat transfer and pressure drop of the visualization study to that of the experiments performed by Tao, insight can be gained on the influence of the modifications of the GPHE for visualization purposes.

Influence of polymer plate geometry
The surface of the PS is machined by a CNC-machine into a corrugation pattern similar to the pattern of the heat transfer plate. However, some minor geometrical alterations on the corrugation pattern were necessary to make sure the CNC-machine was able to perform the work. A description of the specific geometrical alterations on the corrugated pattern can be found in the report of Dahlgren [16]. The total pressure drop of the GPHE including polymer plate is compared to the total pressure drop of the original GPHE for similar experimental conditions. The results are shown in figure 5.11. For these pressure drops of both experiments, the pressure difference between the inlet pressure sensor and outlet pressure sensor of the GPHE are used and not the pressure differential sensor, because that sensor was not installed yet during the experiments of Tao. Only the sets with similar mass fluxes are shown in Figure 5.11.

The figure shows that the pressure drop of the GPHE including the polymer plate is lower than the pressure drop of the GPHE including the stainless steel plate. The difference in pressure drop especially is almost a factor two. It is possible that the lower pressure drop is due to the modified geometry of the visualization plate but it is expected to be mostly due to the difference in the moment applied when tightening the bolts. The applied moment for the stainless steel pressure plates was 90 Nm for the single-channel experiments performed by Tao, while for the visualization configuration this was 60 Nm.

Influence of LED-strip and insulation on heat transfer balance
The LED-strip added heat to the GPHE from the circumference of the plates. The LED-strip encircled the GPHE circumference twice, covering both the circumferential surface of the cold water side and the working fluid side. For a well insulated GPHE, it is assumed that the heat transfer between the environment and the GPHE is zero, which is the case for the experiments performed by Tao. However, for the visualization

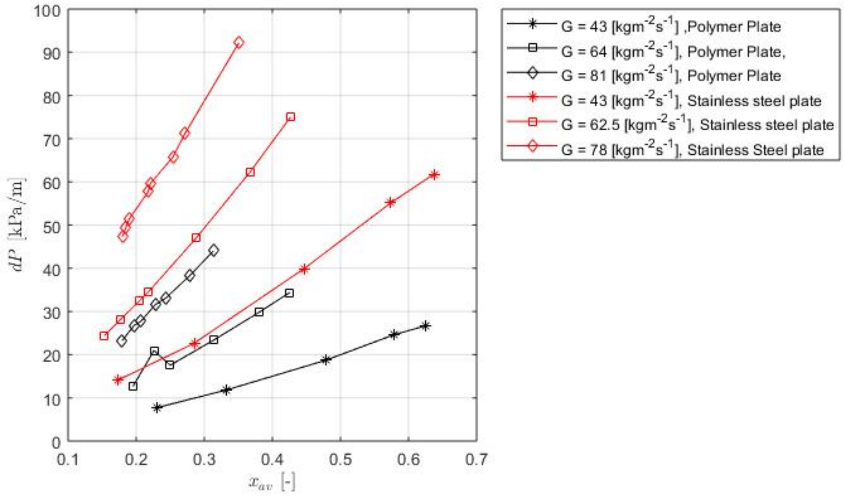

Figure 5.11: The measured total pressure drop for the experimental setup including the polymer plate and stainless steel plate versus the average quality

experiments, the front of the GPHE is not insulated, see Figure 5.12. The thickness of the polymer plate is 25 mm, which could work as insulation itself.

Figure 5.12: Applied insulation material to the GHPE, rear and frontal view

Equation 5.16 shows the heat transfer balance for the GPHE including the heat transfer by radiation from the LED $\dot{Q}_{LED,W}$ and $\dot{Q}_{LED,a}$ and the heat transfer by conduction from the environment through the plate.

$$\dot{Q}_{LED,W} + \dot{Q}_W = \dot{Q}_a + \dot{Q}_{LED,a} + \dot{Q}_{env} \tag{5.16}$$

Where $\dot{Q}_{env}$ is defined by:

$$\dot{Q}_{env} = \kappa_{PMMA} A_{eff} \frac{(T_{env} - T_{av})}{d_{p,PMMA}} \tag{5.17}$$

According to CES Edupack [32], the thermal conductivity of PMMA $\kappa_{PMMA} \approx 0.09$ [Wm^{-1}K^{-1}]. The plate thickness of the polymer plate $d_{p,PMMA} = 25$ [mm]. For simplification, the PS-layer is neglected because it takes up a very small amount of the total thickness of the plate. The outer pressure plate with windows is also neglected. The temperature of the environment is determined as follows. A picture is taken with an infrared camera that determines the temperature right outside of the PMMA plate, which is around 18.7 °C. For the temperature inside the GPHE ammonia channel, the minimum temperature inside is taken. According to CES Edupack [32], PMMA is a very good insulator, and as expected, $\dot{Q}_{env}$ is negligible. It can be concluded that the difference in insulation between the original GPHE and GPHE for visualization can be neglected.

The LED-strip is located inside the insulation material and might have a stronger effect. From a side view of the GPHE, the LED-strips cover the gaskets, where heat transfer might occur towards the cold water and working fluid channel, since the rubber gasket is the only material barrier between the LED-strip and the fluids. According to CES Edupack (2018), the thermal conductivity of rubber is also small, $\kappa_r \approx 0.08$ [$\mathrm{Wm^{-1}K^{-1}}$]. The temperature of the LED T_{LED} indicated by the infrared picture is around 26 °C. For $T_{av,W}$, the minimum temperature of the cold water side is used for all sets.

$$\dot{Q}_{LED,a} = \kappa_r A_{circ} \frac{(T_{LED} - T_{av,a})}{w_r} \tag{5.18}$$

$$\dot{Q}_{LED,W} = \kappa_r A_{circ} \frac{(T_{LED} - T_{av,W})}{w_r} \tag{5.19}$$

Where A_{circ} is the circumferential area of the gasket, w_r is the width of the rubber gasket located between the ammonia and the LED strip. Both $\dot{Q}_{LED,a}$ and $\dot{Q}_{LED,W}$ are very small (around 1 % of $\dot{Q}_a$), since the gasket is a good insulator and the temperature difference between the LED strip and the internal water and working fluid temperatures are too small to make a significant difference. It is therefore concluded that the alterations on the GPHE have a negligible effect on the heat transfer inside the GPHE for the visualization experiments. Therefore, the inlet quality of the ammonia channel is determined by using the heat transfer balances by assuming there is no heat loss to the environment. The heat added by the LED-strip is negligible and therefore, $\dot{Q}_a = \dot{Q}_W$.

5.3.4. Pressure drop of multi-channel experiments

The pressure drop of the multi-channel experiments is compared to that of the visualization experiments, see Figure 5.13. In the left figure, the pressure drop measured by the pressure differential sensor is shown. The right figure shows the pressure drop calculated by subtracting the outlet pressure sensor values from the inlet pressure sensor values. The visualization experiments are indicated in the legend by 'Visualization', and the multi-channel experiments by 'Multi-channel'.

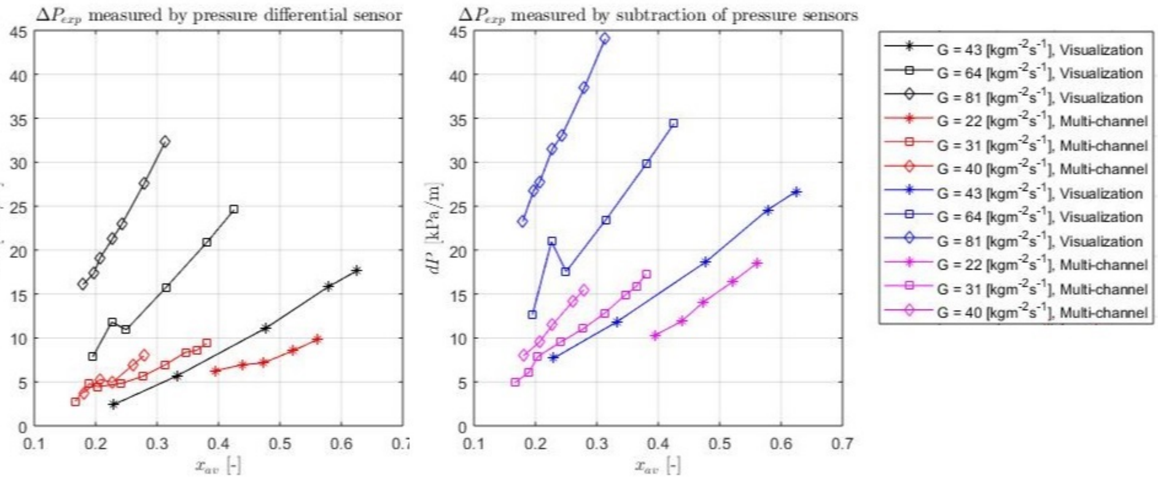

Figure 5.13: The measured pressure drop per meter length of the GPHE of the visualization experiments and the multi-channel experiments versus the average quality. Left) Measured pressure drop by differential sensor. Right). Measured pressure drop by subtraction of in- and outlet sensor values

It becomes immediately clear that the pressure drop ΔP_{exp} calculated by subtraction of the inlet pressure and outlet pressure is much higher than the measured pressure difference by the pressure differential sensor. The pressure differential sensor is expected to have a higher accuracy, and therefore it is advised in the future to always use this sensor. The range of quality is smaller for the multi-channel experiments as compared to the visualization experiments. This is because stabilizing the system for lower mass flux is more difficult. Interesting is that the pressure drop for the multi-channel experiments with similar mass flux to the visualization experiments is slightly higher (for $G \approx 40$ kgm^{-2}s^{-1}). This can be due to the fact that inside the tubes of the in- and outlet ports the flow is not divided yet over the channels, and the local flux in the tubes is twice as high. This also holds for the mixing pressure drop. Inside the channel, the ammonia mass flow rate divides over 2 channels instead of over one, which reduces the pressure drop. Figure 5.13 shows that when the mass flux of the multi-channel experiments is increased, the difference between two points with the same vapor quality are small. For the multi-channel experiments, the pressure drop is therefore more strongly related to the vapor quality then to mass flux. The pressure drops for the multi-channel experiments are comparable to the pressure drops of the partial film flow observed in the visualization experiments with a mass flux of $G =$ 43 kgm^{-2}s^{-1}.

5.3.5. Heat transfer multi-channel experiments

For the multi-channel experiments, the minimum value of the equivalent Reynolds number $Re_{eq} = 1662$, which is just above the proposed value by Longo et al. of 1650. It is expected that most of the subsets are in the convective condensation regime, but some might be in the transition regime. The HTCs for the multi-channel experiments for all performed sets are presented in Figure 5.14. It is clear from both figures that the HTCs increase with vapor quality. The behaviour of the HTCs with respect to mass flux is more clear in the left figure for this series of experiments. The left figure shows that the vapor quality range of $G = 31$ kgm^{-2}s^{-1} and $G = 40$ overlap kgm^{-2}s^{-1}. Here it is seen that the HTCs increase with the mass flux, which is in accordance with a convective condensation mechanism. Remarkable is the buckle in the slopes with increasing vapor quality. This phenomenon is especially seen for $G = 22$ kgm^{-2}s^{-1}. The slope of the HTCs for $G = 31$ kgm^{-2}s^{-1} also flattens for increasing x. As mentioned in section 5.3.2, this change in the slope is also seen for a mass flux of $G = 43$ kgm^{-2}s^{-1} and $G = 64$ kgm^{-2}s^{-1}, see Figure 5.10. Kim [28] also mentions a buckle in the Nusselt number for a varying Reynolds number and explains this phenomenon by partial wetting. In section 5.4.4, the influence of the growth of this void is further inspected.

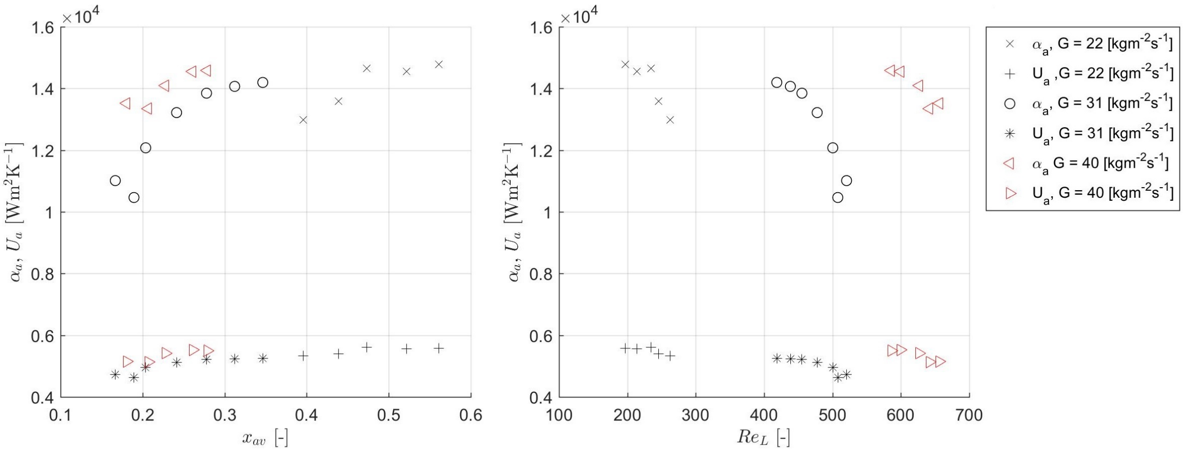

Figure 5.14: Overall and ammonia HTCs of the multi-channel experiments. Left) HTCs versus average vapor quality x_{av}. Right) HTCs versus the liquid Reynolds number Re_L

5.3.6. Conclusions

Conclusions are drawn on the pressure drop and heat transfer analysis of the visualization experiments and multi-channel experiments.

Conclusions visualization experiments:

- For single channel experiments, the pressure drop increases strongly with the mass flux and vapor quality.
- Partial film flow is observed for the lower mass flux which corresponds to a lower pressure drop. Film flow is observed for higher mass flux and a higher pressure drop.
- The HTCs seem to increase with mass flux, which is in agreement with the convective condensation regime.
- The HTCs increase with vapor quality. However, partial film flow shows a different slope for the HTCs with increasing vapor quality than film flow. For partial film flow, the HTCs seem to stabilize instead of further increase with vapor quality while film flow shows more linear characteristics. It is expected that the change in slope for partial film flow has to do with the increasing size of the surface area void.
- The influence of the LED-strip and partial insulation on the GPHE have minor effects on the performance of the GPHE. Therefore, the determination of the inlet vapor quality by energy balance is considered to be accurate for the assumption that $\dot{Q}_a = \dot{Q}_W$.
- The GPHE configuration for visualization does influence the pressure drop by a decrease in pressure drop for all visualization experiments as compared to the single-channel experiments performed by Tao. This could be due to the smaller applied torque to the bolts as compared to the other experiments and the modifications of the visualization plate geometry.

Conclusions multi-channel experiments:

- The pressure drop measured by the inlet and outlet pressure sensors over-predicts pressure drop measured by the pressure differential sensor. It is advised for future experiments that for pressure drop analysis the pressure differential sensor should be used.
- The HTCs of the multi-channel experiments also increase with vapor quality. This is in accordance with the convective condensation mechanism.
- The HTCs of the multi-channel experiments show a buckle in the slope of the HTCs for an increasing vapor quality at constant mass flux. This is also seen for the HTCs of the partial film flow of the single-channel visualization experiments.
- It is expected that the latter is related to the growth of the surface area void. While for a constant mass flux the vapor quality is increased, the HTC grows. However, it is expected that as the void surface area grows, this increase of the HTC becomes less, explaining the curve of the HTC to flatten or become a constant for increasing vapor quality.

5.4. Void fraction analysis

In this section, a distinction is made between a volumetric void fraction ϵ and surface area void fraction ϵ_A. The volumetric void fraction is the amount of vapor volume present in the channel with respect to the total volume, and is widely used for predicting the pressure drop in plate heat exchangers. However, most correlations neglect the possible effects of flow patterns, the rate of change of the vapor quality during condensation and the inclination of the channel [10]. An analysis is performed to investigate if there is a strong relation between the expected void fraction in the GPHE and the observed flow patterns during the visualization experiments (film flow and partial film flow). The surface area void fraction however, is different and should not be confused with the volumetric void fraction over a cross-sectional area. The surface area void fraction is in this thesis referred to as the fraction of the surface area of the heat transfer plate that is not wetted by the liquid. In literature, this phenomenon is mostly referred to as 'voids', 'partial wetting' and 'dry-out', but were considered either confusing or less clear than the current definition. With partial film flow, dry voids occupied by vapor only are present on the surface area. It is expected that this has a negative influence on the heat transfer with respect to the case where the entire surface is wetted. In this section the surface area void fraction is estimated by image processing using Matlab and an analysis is performed where the volumetric void fraction inside the GPHE is compared to the surface area void fraction. At last, the surface area void fraction is related to the HTCs.

5.4.1. Volumetric void fraction models from previous studies

Two important parameters for determining the volumetric void fraction are the two-phase multiplier Φ_L and the Lockhart-Martinelli parameter X. The two-phase liquid multiplier is defined by Equation 5.20 and represents the ratio of the frictional two-phase pressure drop to the frictional single-phase pressure drop.

$$\Phi_L^2 = \frac{\Delta P_{f,TP}}{\Delta P_{f,L}} \tag{5.20}$$

Lockhart and Martinelli based their analysis on separated flow and their correlation is defined by Equation 5.21. The Lockhart-Martinelli parameter X represents the ratio of the frictional liquid phase pressure drop to the frictional vapor phase pressure drop if only one of the two phases would flow in the channel.

$$X = \sqrt{\frac{\Delta P_{f,L}}{\Delta P_{f,V}}} \tag{5.21}$$

Chisholm [14] proposed a correlation that relates the two-phase multiplier to the Lockhart-Martinelli parameter for gas-liquid or vapor-liquid flow in pipes, but is also used in several later studies for various working fluids in PHEs. The Chisholm correlation is defined by Equation 5.22 where C is determined by iteration for each data point. Finally, the average of C is taken for the correlation.

$${\Phi_L}^2 = 1 + \frac{C}{X} + \frac{1}{X^2} \tag{5.22}$$

Wallis [52] analytically derived a relation for the volumetric void fraction ϵ for annular separated flow in tubes by assuming that the velocity of the vapor is much higher than the velocity of the liquid. The proposed relation is found to be approximately valid by numerous investigators. The void fraction relation proposed by wallis is defined by Equation 5.23.

$$\epsilon = 1 - \frac{1}{\Phi_L} \tag{5.23}$$

Zivi [60] proposed a volumetric void fraction relation for steam with x the vapor fraction:

$$\frac{1}{\epsilon} = 1 + \frac{1-x}{x}\left(\frac{\rho_V}{\rho_L}\right)S \tag{5.24}$$

Where $S = (\frac{\rho_L}{\rho_V})^{\frac{1}{3}}$, is the slip ratio analytically derived assuming ideal, steady annular flow where the rate of entropy production is minimized. Both Winkelmann [56] and Wang et al. [53] used the Chisholm correlation in combination with a void fraction model. Winkelmann combined the Chisholm correlation with the void model of Wallis, and Wang et al. combined Chisholm correlation with the void model of Zivi. Lovich and Carey [35] also propose a relation between the two-phase multiplier and the Lockhart-Martinelli parameter, see Equation 5.25, and a void fraction model , see Equation 5.26, for a PHE with a corrugation angle of $\beta = 30°$.

$${\Phi_L}^2 = 1 + \frac{10.1}{X^{1.37}} + \frac{1}{X^2} \tag{5.25}$$

Lovich and Carey correlated the two-phase multiplier Φ_L and the void fraction ϵ using X as the variable. The void fraction was determined by isolating the two-phase flow in the test section at the end of each experiment.

$$\epsilon = (1 + X^{0.565})^{-0.986} \tag{5.26}$$

The homogeneous model for the volumetric void fraction is given by Equation 5.27.

$$\epsilon = \left(1 + \frac{1-x}{x}\frac{\rho_V}{\rho_L}\right)^{-1} \tag{5.27}$$

5.4.2. Volumetric void fraction of visualization experiments

First, the two-phase liquid multiplier and Lockhart-Martinelli parameter are determined for the GPHE in the OTEC demo. The method used for determining the frictional two-phase pressure drop $\Delta P_{f,TP}$ is explained in section 5.3.1. The frictional pressure drop for the liquid phase and vapor phase are determined according to Equation 5.28 and 5.29:

$$\Delta P_{f,V} = \frac{2 f_V G_V^2 L_p}{\rho_V d_p} \tag{5.28}$$

$$\Delta P_{f,L} = \frac{2 f_L G_L^2 L_p}{\rho_L d_p} \tag{5.29}$$

Where $G_L = (1-x)G$ kgm^{-2}s^{-1} and $G_V = xG$ kgm^{-2}s^{-1}.

The liquid and vapor Fanning friction factors f_L and f_V are determined by using Equation 5.30 and 5.31 for laminar and turbulent conditions. These friction factors were correlated by Winkelmann [56] for a corrugated plate heat exchanger.

$$f_{L,V} = 0.3 + \frac{53}{Re_{L,V}} \quad \text{for } Re_{L,V} \leq 1700 \tag{5.30}$$

$$f_{L,V} = \frac{1}{{Re_{L,V}}^{0.135}} \quad \text{for } Re_{L,V} > 1700 \tag{5.31}$$

Where $Re_V = \frac{xGd_h}{\mu_V}$ and $Re_L = \frac{(1-x)Gd_h}{\mu_L}$. Equations 5.28 - 5.31 are used to calculate the two-phase multiplier Φ_L and the Lockhart-Martinelli parameter X of the experiments, defined by equations 5.20 and 5.21. The vapor frictional pressure drop increases with an increasing vapor quality, which indicates that the Lockhart-Martinelli parameter X is a strong function of x and should decrease with an increasing vapor quality. This behaviour is confirmed in Figure 5.15.

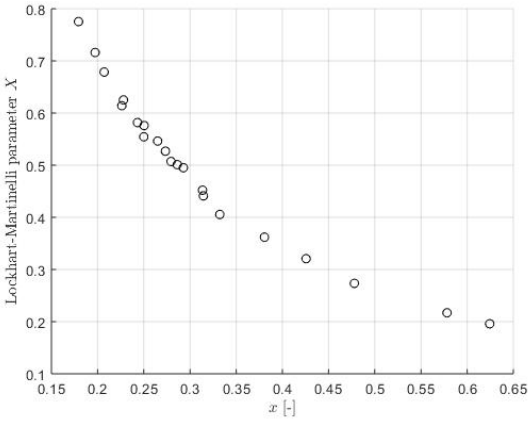

Figure 5.15: The Lockhart-Martinelli parameter X versus average vapor quality x for the GPHE

The Chisholm correlation, defined by Equation 5.22, is used to form a correlation between Φ_L and X for the GPHE. C is determined by iteration for each data point and averaged to gain the constant C. For the visualization experiments, C = 2.64, see Equation 5.32.

$$\Phi_L = 1 + \frac{2.64}{X} + \frac{1}{X^2} \tag{5.32}$$

The experimental results and correlation are presented in Figure 5.16. For C = 2.64, the correlation predicts the two-phase multiplier with an average deviation of 13.73 %. The correlation predicts the two-phase frictional pressure drop $\Delta P_{f,TP} = \Phi_L^2 \Delta P_{f,L}$ with an average deviation of 25.25 %. Winkelmann [56] performed the same comparisons to the Chisholm correlation with C-value of 6 and the deviations varied between +/- 10 % - 20%.

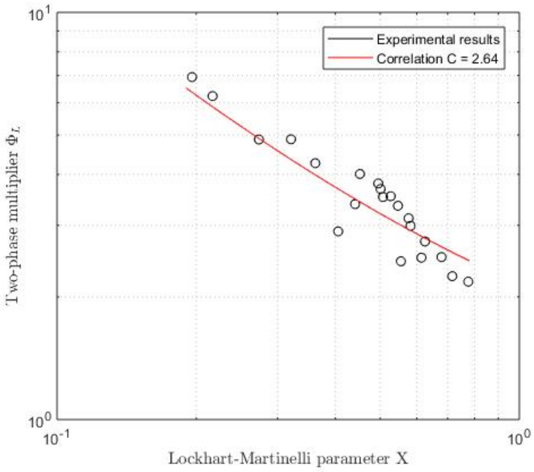

Figure 5.16: Experimental two-phase multiplier Φ_L results and Chisholm correlation with C = 2.64 versus Lockhart-Martinelli parameter X

The value of C of the current study is lower as compared to the C values of the other presented studies, see Table 5.3. The current correlation is compared to correlations of previous studies within the experimental conditions of the visualization experiments, see the left figure in Figure 5.17. The current correlation seems to follow the trend-line of the correlations of the other studies, indicating that for the same range of X, the growth of the ratio between the two-phase friction pressure drop over the liquid frictional pressure drop is similar for decreasing X. However, the line has a lower off-set, indicating that for the GPHE this ratio is smaller as compared to the studies with water and lower corrugation angles.

Table 5.3: Studies that make use of Chisholm relation in a void fraction model

Study	*Fluid*	*Corrugation angle*	*C-value*	*limits*
Wang et al. [53]	Steam (condensation)	$\beta = 30\,°$	16	0.02 <X <0.04
Winkelmann [56]	Air/water	$\beta = 25.7\,°$	6	0.01 <X <1
Tribbe & Muller Steinhagen [48]	Air/water	$\beta = 30, 60\,°$	8	0.06 <X <10
Lovich & Carey [35]	R-113	$\beta = 30\,°$	See eq. 5.25	
Current study	Ammonia	$\beta = 60\,°$	2.64	0.18 <X <0.8

The right hand side figure in Figure 5.17 shows the behaviour of the correlations for the various studies in a wide range of X that exceeds the X-range of the visualization experiments. The deviation between the correlation of the current study and that of the previous studies is largest around $X = 1$ and least for large and small X. However, this deviation is dependent on the form of the correlation that is chosen to fit. For example, the correlation formed by Lovich & Carey is of a different form and shows a steeper line. Finally, the correlation from Wallis [52] is used (defined by Equation 5.23) to determine the volumetric void fraction relation ϵ for the GPHE, see Figure 5.18. The scattered results seem to follow a parabolic line, but do not deviate from the trend for varying mass fluxes. The volumetric void fraction ϵ seems to be independent from the mass flux G. As is expected, the volumetric void fraction ϵ increases with average vapor quality x.

5.4.3. Relation between volumetric void fraction and flow pattern

Figure 5.19 shows the volumetric void fraction predicted by various models. The void fraction model of Wallis [52] uses the two-phase multiplier Φ_L, Lovich & Carey [35] use the Lockhart-Martinelli parameter X, and both the homogeneous model and the model of Zivi [60] make use of ρ_V, ρ_L and x. The homogeneous model

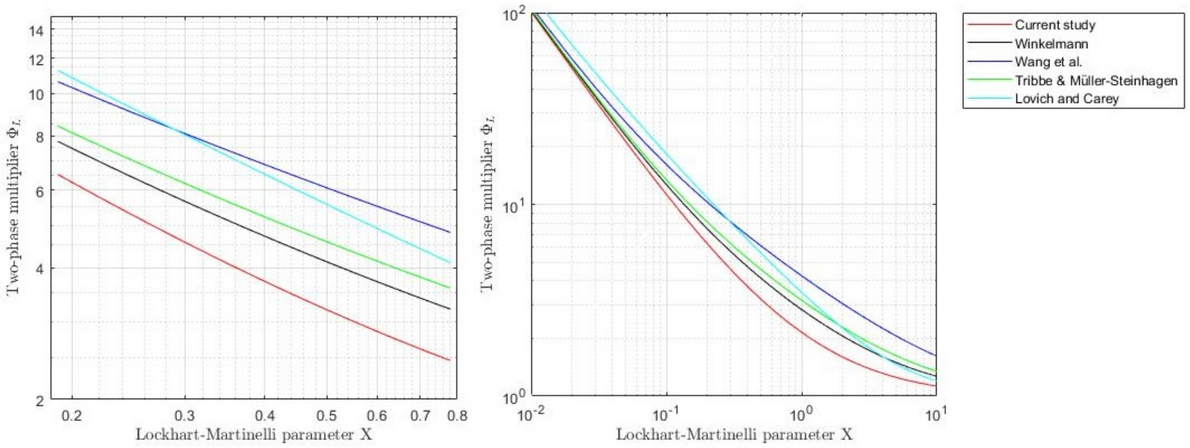

Figure 5.17: Two-phase multiplier correlation of current study and several other studies within limits of visualization experiments

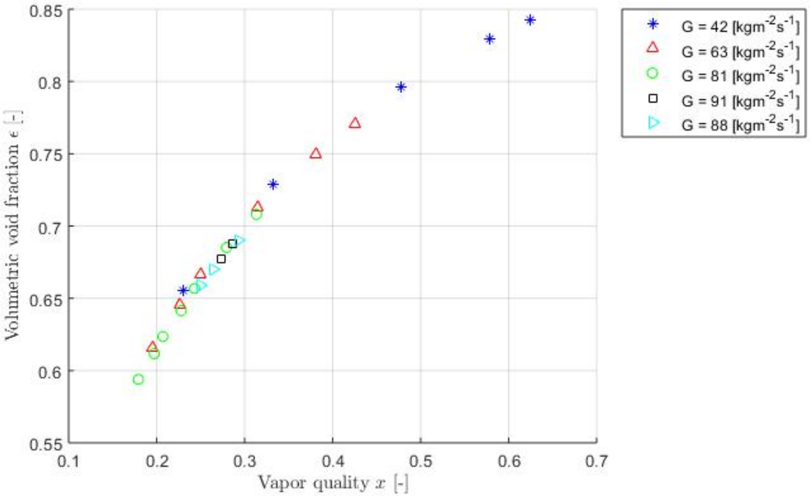

Figure 5.18: Volumetric void fraction ϵ by relation from Wallis [52] versus average quality x for all sets

predicts an almost entirely filled channel with vapor if the flow inside the channel was homogeneous. However, from the visualization it could be seen that there was a strong division between the path of the liquid flow and vapor flow, indicating that the assumption for a homogeneous flow cannot be made for the GPHE as the flow is separated. The correlation of Zivi is close to the homogeneous model but includes an analytically derived slip ratio S into the relation for the void fraction. The model by Wallis [52] is initially developed for annular flow in tubes, but is also applied for determining the void fraction inside a plate heat exchanger by Winkelmann [56]. Lovich & Carey [35] developed a void fraction relation from two-phase flow experiments in a vertical cross ribbed plate heat exchanger with a corrugation angle of $\beta = 30\,°$. It is expected that the analytically derived void fraction relation for annular flow by Wallis [52] and the experimentally determined relation by Lovich & Carey [35] for a cross ribbed PHE predict the void fraction inside the GPHE best. These relations involve most components that are based on separated flow. Finally, the void fraction model by Wallis [52] is taken for reference since the two-phase multiplier could be compared to those of the previous studies and showed a similar trend.

With a vapor quality of 20%, the vapor volume inside the channel is around 60 %. With a vapor quality of 60 %, the vapor volume is around 85 %. Figure 5.19 also shows for which data points a void was seen on the surface of the GPHE (i.e. partial film flow), indicated by red data points. Data points where the entire surface of the polymer was wetted (i.e. film flow) is indicated by black data points. One can see that the partial film flow is observed for all volumetric void fractions, indicating that the volumetric void fraction does

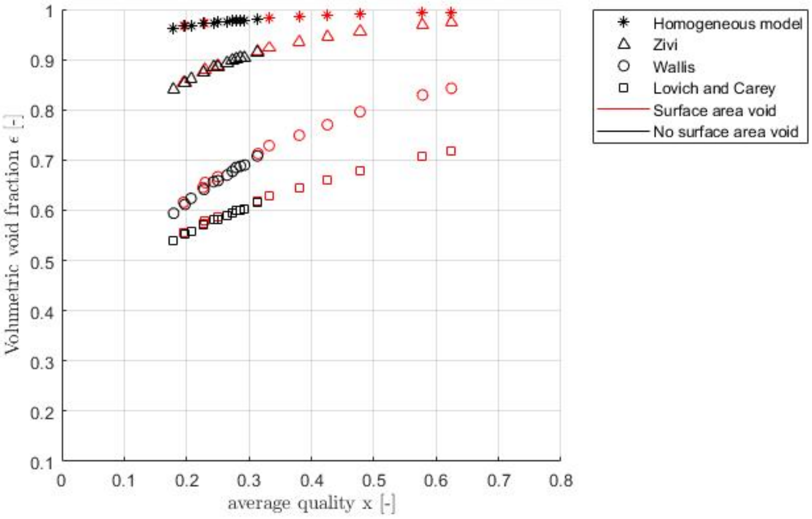

Figure 5.19: Volumetric void fraction ϵ from various models versus average quality x

not necessarily determine the transition between partial film and film flow. This result is not unexpected, since the conclusion was drawn that the mass flux does not influence the volumetric void fraction. On the other hand, from the visualization experiments it is known that the mass flux does influence the occurrence of surface area voids. However, this result does not say anything about the relation between the quality, volumetric void fraction and the growth of the surface area void on the plate. This analysis is performed in the next section.

5.4.4. Surface area void fraction by previous studies

Determining the void fraction by image processing has not been done as extensively as developing a volumetric void fraction model as described in section 5.4.1. However, Kim [28] estimated the wet surface area for water flows in a plate heat exchanger by observation, despite drawing the conclusion that it is likely to contain a large error. The following relation was developed:

$$\frac{A_{wet}}{A_{eff}} = 0.052 Re_f^{0.58} \tag{5.33}$$

Where Re_f is the film Reynolds number for a liquid falling film flow, $Re_f = \frac{4G(1-x)}{\mu_L \Pi}$. Π is the perimeter of the channel, $\Pi = 2d_g + 2L_p$. In this case, the surface area void fraction ϵ_A becomes:

$$\epsilon_A = 1 - \frac{A_{wet}}{A_{eff}} \tag{5.34}$$

5.4.5. Surface area void fraction from visualization experiments

Image processing by Matlab is used to get an estimation of the surface area void fraction of the GPHE. The software Photon Fastcam Viewer connected to the high speed camera both processed the frames into images that were stored consecutively over time, as well as videos. From both the videos and images the following was observed. During the experiments the liquid was either a rough or a smooth film. When the liquid showed rough film characteristics, a lot of movement and color change on the video was seen. The rough film zone mostly covered the upper half and a small corner on the bottom right. The smooth film was mostly seen for high mass flux on the lower diagonal of the top window, and for low mass flux on the upper diagonal of the top window. The smooth film showed also movement and change of grey-scale on the image due to the pulsating liquid movement created by the piston pump. The void zone turned opaque and remained mostly static during every steady state subset. This observed phenomenon is used for image processing, where the images are processed in such a way that the smooth and rough film zone were assigned different thresholds than the static voids.

For every subset, 6000 pictures were taken in a time-span of 2 seconds. To save memory, 600 pictures that showed most movement were saved for creating videos and processing the images. The camera was mounted on a tripod, located with a horizontal distance of 50 cm from the plate. To make pictures of the top, middle and bottom window, the height of the tripod was adjusted for every subset. This means that the horizontal distance, height, angle and amount of illumination that enters the lens are slightly different for every subset. This makes image processing more difficult for Matlab, and for every subset boundary conditions have to be given as an input for the code in Matlab to process the data correctly. Figure 5.20 shows the flow diagram of the code used for processing the image.

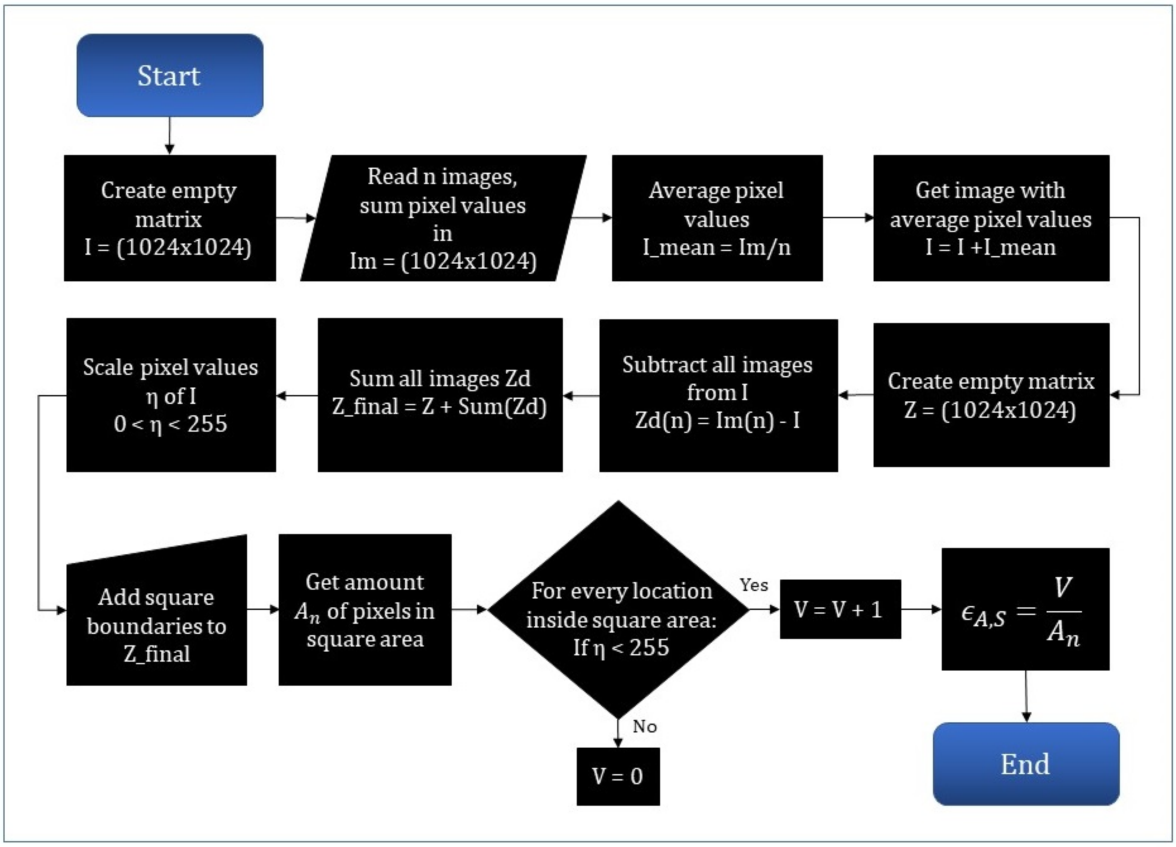

Figure 5.20: Flow diagram of Matlab program for estimating the surface area void fraction

The first step is to create an image that represents the average of all images from that subset. This means that the average of the pixels of all images for a specific location is taken. This is done for all locations on the image. An empty matrix I is created with the same amount of entries as the amount of pixels in the image (1024 x 1024). All images for the subset are read by Matlab, and the pixel value is taken from every image and summed for every pixel location. I_m is a matrix containing all summed pixel values. Next, all summed pixel values are divided over the amount of images, returning a matrix I with average pixel values over all images per location in the image.

Next, an image is created that represents the amount of movement in an image versus the static zone in the image. For image Z_d, image I is subtracted from all images, so than what remains are the pixels that have changed, i.e. the smooth and rough film zones. This is done for every image and summed so that an image Z_{final} is gained that presents all the movement with a bright color. All pixel values are scaled from 0 to 255, where 0 returns a black color and 255 a bright yellow color. The dark color represents the pixels that remained static and a bright color the summation of all the movements, see Figure 5.21 and 5.22. One can see that the moving liquid zone is larger for a higher mass flux, and that the static part in image Z_d is smaller for a higher mass flux than with a lower mass flux. The higher vapor quality returns a large surface area void fraction, which is in accordance with the expectations. As a check, all gained images from the Matlab code are compared to the original images, and the location and size of the void seem to match.

Finally, boundaries are created to select the square area A,S where the amount of pixels are counted to represent the total square pixel area of the top window, A_n. Next, the amount of pixels V are counted that are below a pixel value of 255, representing the static pixel values. The gained $\epsilon_{A,S}$ represents the void fraction within the square A,S that is selected. The square selected is the largest rectangular that could be selected from the image, i.e. the area of the top window without the inlet zone, see Figure 5.23.

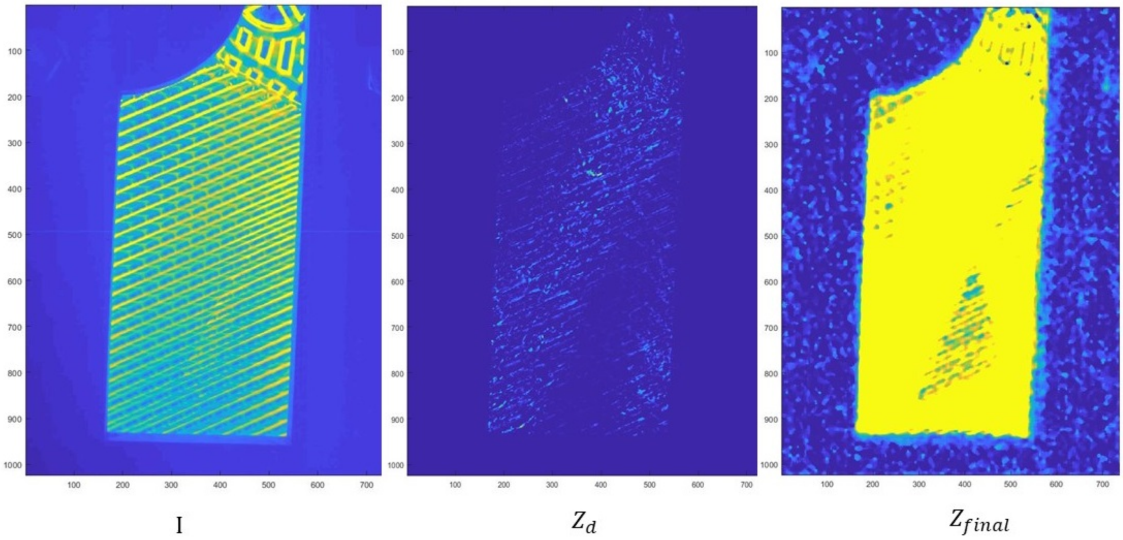

Figure 5.21: $G = 64$ kgm^{-2}s^{-1}, $x = 0.2$ Left) Image I. Middle) Image Z_d. Right) Image Z_{final}

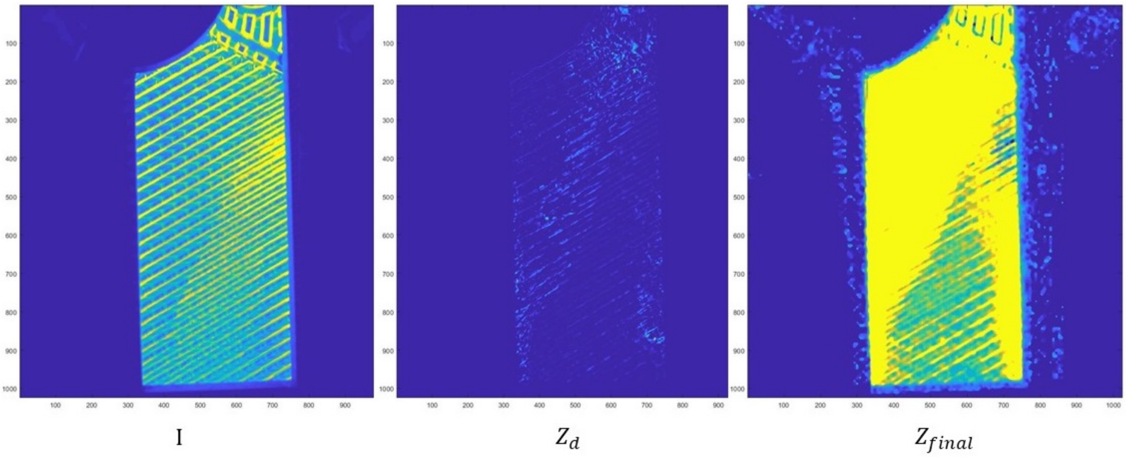

Figure 5.22: $G = 43$ $[kg/m^2 s]$, $x = 0.33$ Left) Image I. Middle) Image Z_d. Right) Image Z_{final}

The actual square area in m^2 is gained from the measurement tool in SolidWorks. To convert this square area void fraction to the void fraction over the effective heat transfer area, Equation 5.35 is applied:

$$\epsilon_A = \frac{\epsilon_{A,S}}{z} \tag{5.35}$$

Where $z = \frac{A_{eff}}{A,S}$, $A_{eff} = 0.0640$ m^2, $A,S = 0.01458$ m^2, and $z = 4.39$. The results are presented in Table 5.4, where only the sets are presented where voids were seen. For the rest of the sets, $\epsilon_A = 0$ %.

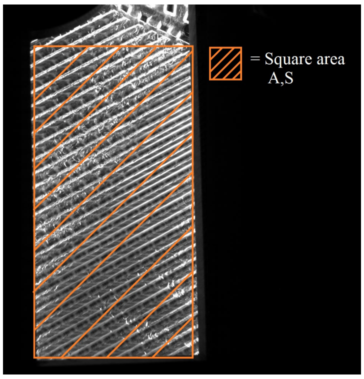

Figure 5.23: Selected square area A,S

Table 5.4: Surface area void fraction on GPHE for the visualization experiments

$G = 43$ [kgm^{-2}s^{-1}]						
x [-]	0.23	0.33	0.48	0.58	0.62	
ϵ_A [%]	4.91	8.37	8.64	10.58	15.12	
$G = 64$ [kg/m^{2}s]						
x [-]	0.19	0.22	0.25	0.32	0.38	0.43
ϵ_A [%]	1.55	0	1.94	3.27	3.4	4.39

Here, x is the average vapor quality. The table shows that a void covers the surface area of the plate between 1.55 % and 15.12 %. From the table it can be seen that the void fraction increases with an increasing vapor quality. Second, the size of the void is larger with the lower mass flux as compared to the higher mass flux with the same vapor quality, see Figure 5.24. However, the growth of the void seems to follow the same trend. For $G = 64$ kgm^{-2}s^{-1} and $x = 0.22$, $\epsilon_A = 0$. This experiment is performed on another day, where first a series of experiments with a high mass flux was performed. Therefore, the area was already entirely wetted. This could indicate that once the area is wetted, no dry-outs appear when lowering the mass flux.

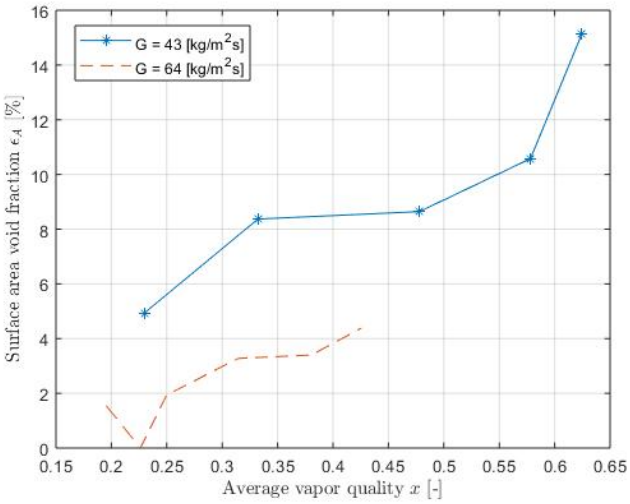

Figure 5.24: The surface area void fraction ϵ_A versus average vapor quality x for different mass fluxes

.

Comparing surface area void fraction from literature and from visualization experiments

Kim [28] used a power correlation for the surface area void fraction in the form of:

$$\epsilon_A = 1 - aRe_f^b \tag{5.36}$$

The surface area void fraction gained from the experimental data is plotted against the film Reynolds number and a correlation is formed in the form of Equation 5.36. Table 5.5 gives the a and b values that are used by [28] and the fitted correlation. The quality of the fit is evaluated as follows. The sum of squares due to error (SSE) [1] is a measure for the random error and should be close to zero if it is considered useful for prediction. For this fit, the SSE = 0.0022. The R-square [2] measures the success of the fit by evaluating the variation of the data, and can only take on a value between 0 and 1. An R-square value close to 1 means that the fit explains close to 100 % of the variation in the data about the average. For this fit, the R-square = 0.943. The Root Mean Squared Error (RMSE)[3] is the fit standard error and estimates the standard deviation of the random component in the data and should be close to zero for a useful prediction. Here, the RMSE = 0.010. This is considered an acceptable fit for the correlation and is presented in Figure 5.25.

Table 5.5: Parameters used for power correlation by Kim [28] and the visualization experiments

	Correlation by Kim [28]	*Correlation by experiment*	*Limit*
a	0.052	0.58	$0 < Re_f < 165$
b	0.58	0.1	$60 < Re_f < 230$

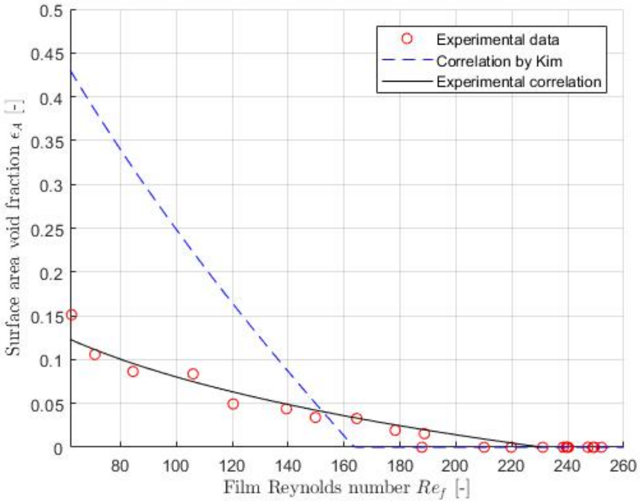

Figure 5.25: Surface area void fraction ϵ_A versus film Reynolds number Re_f, from Kim [28] and experimental results

Kim's correlation [28] is fitted for water in a PHE without corrugations, where liquid only flows over the plate. In the visualization experiments, a condensing flow is observed with a corrugation pattern and a corrugation angle of $\beta = 60\ °$. The corrugations and the pattern of the inlet zone contribute to a better distribution of the liquid over the plate, explaining the lower surface area void fraction values for the lower range of the film Reynolds number. The fact that the surface voids remain on the plate for higher film Reynolds numbers is due to the vapor inside the channel, which is not present in the experiments performed by Kim [28]. At last, the surface tension of pure ammonia is lower than that of water. The average surface tension σ of pure ammonia for the experimental conditions of the GPHE is 0.028 [Nm^{-1}] as compared to 0.0736 [Nm^{-1}] for water. This means that the surface tension force at the surface of the plate is lower and shows better wettability than in the case of water, which is in accordance with the results presented in Figure 5.25.

---

[1] SSE = $\sum_{i=1}^{n} (y - \hat{y})^2$, where n is the number of data-points, y is the measured value and $\hat{y}$ is the value from the correlation

[2] R-square = $1 - \frac{SSE}{\sum_{i=1}^{n} (y - \bar{y})^2}$, where $\bar{y}$ is the average of the measured datapoints

[3] RMSE = $\sqrt{\frac{SSE}{n}}$

5.4.6. Relating volumetric void fraction, surface area void fraction and vapor quality

Figure 5.26 and 5.27 show the surface area void fraction versus average vapor quality and film Reynolds number. Only the data points are shown where a surface void did occur. In other words, these figures hold for partial film flow.

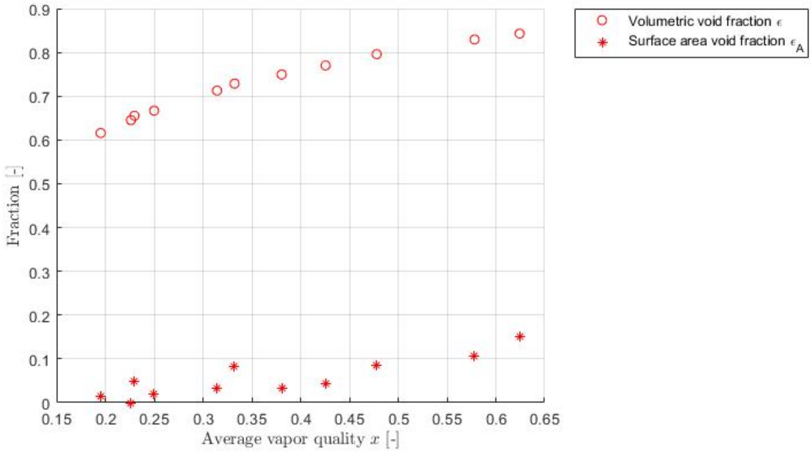

Figure 5.26: Volumetric void fraction ϵ and surface area void fraction ϵ_A versus average vapor quality x

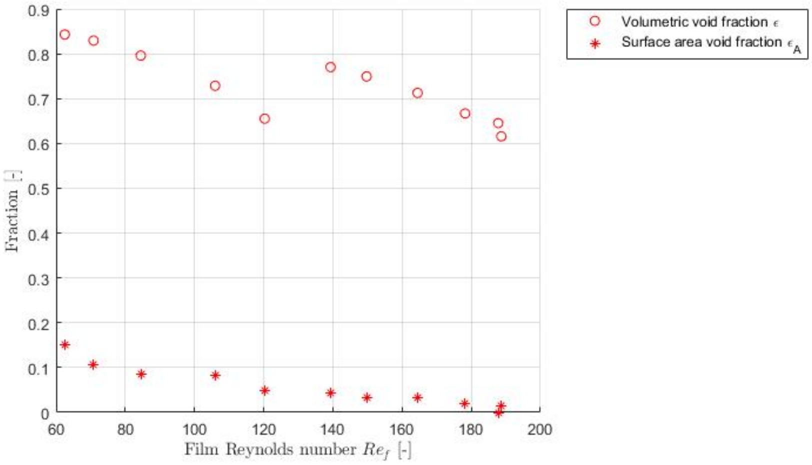

Figure 5.27: Volumetric void fraction ϵ and surface area void fraction ϵ_A versus film Reynolds number Re_f

From Figure 5.26 one can see that the surface area void fraction follows the same trend as the volumetric void fraction for an increasing vapor quality. This means that once a void occurs on the plate, this void will grow when the volumetric void fraction inside the channel increases. Once a void is present, the growth of the surface area void is significant. By increasing x from 0.19 to 0.62, ϵ grew with 30 % and ϵ_A grew from 1.55 % to 15.12 %, which is almost 10 times as large. However, the vapor quality is not the best parameter for comparison, since for the same vapor qualities but a higher mass flux no voids will be apparent. The film Reynolds number takes both x and G in account and the transition between partial film flow and film flow was apparent at $Re_f \approx 200$. Figure 5.27 shows that ϵ_A and ϵ both decrease with an increasing film Reynolds number, as is expected. The behaviour of both void fractions seems strongly related with the film Reynolds number. As is seen in Figure 5.25, there is no partial film flow observed for a film Reynolds number above 200. This means that the surface area void fraction can be related to the volumetric void fraction for $60 < Re_f < 200$. Another fitting is performed, see Figure 5.28. A power relation is used since the Matlab fitting tool showed the best goodness of fit for this correlation (SSE = 0.004, R-square = 0.8, RMSE = 0.002).

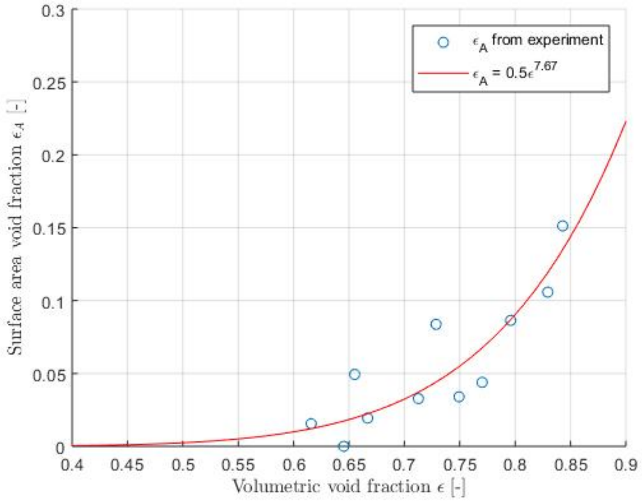

Figure 5.28: Relation between surface area void fraction ϵ_A and volumetric void fraction ϵ that holds between $60 < Re_f < 200$

5.4.7. Relating surface area void fraction and HTCs

Figure 5.29 shows the surface area void fraction, the ammonia HTCs and the liquid Reynolds number for the visualization experiments. When the size of the surface area void increases, the slope of the HTCs of the ammonia becomes less steep, which is in accordance with the expectations. It is expected that for an increasing vapor quality, the HTC increases as well. The liquid layer covering the walls of the channel becomes thinner, and this reduces the thermal resistance. However, when the volumetric void fraction inside the channel becomes too large, the liquid layer disappears on some locations on the heat transfer plate. This causes a negative effect on the heat transfer, because the heat transfer from the vapor to the wall is less than the heat transfer from the liquid to the wall. The slope of the ammonia HTCs shows more linear characteristics for the conditions where no surface area voids are seen.

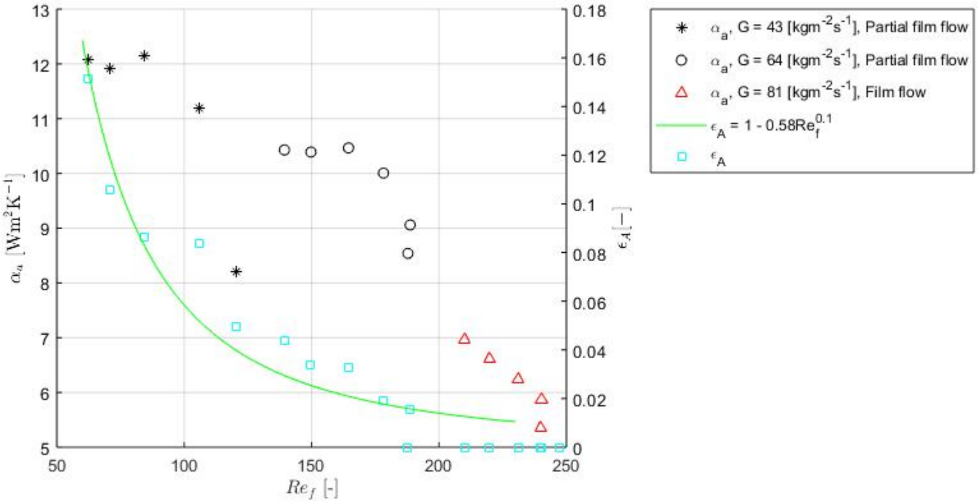

Figure 5.29: Ammonia HTC, surface area void fraction and liquid Reynolds number for set 1, 2 and 3 of the visualization experiments

5.4.8. Summary and conclusions

The volumetric void fraction is determined for all subsets of the visualization experiments performed on the GPHE. The volumetric void fraction is based on the two-phase multiplier and Lockhart-Martinelli parameter, which have been used in many previous studies for determining the volumetric void fraction. Volumetric void fraction correlations from previous studies are compared to investigate whether the gained volumetric void fraction behaves reasonably. The volumetric void fraction correlation by Wallis [52] has been considered to apply. According to the calculations, the volumetric void in the channel laid between 58% and 85% and increase with vapor quality x.

By image processing using Matlab, the surface area void fraction is estimated for all subsets. This is done to investigate if the growth of the surface area void, observed for partial film flow, is the cause of the decay in the slope of the HTCs for increasing vapor quality. Second, because the volumetric void fraction is used in modelling of heat exchangers, it is useful to investigate if there is a relationship between ϵ and ϵ_A and if possible to relate them. A relation is identified between the volumetric void fraction and surface area, where the surface area void grows with the volumetric void fraction. Another correlation is fitted where the surface area void fraction is a function of the film Reynolds number in the same form as the correlation by Kim [28] for a falling water film. By comparison it could be seen that the surface area void fraction is lower for the GPHE than observed by Kim, which can be explained by the lower surface tension of the ammonia. The surface area void fraction and the volumetric void fraction are correlated for $60 < Re_f < 200$.

Finally, the behaviour of the HTCs of the ammonia is compared to the increase of the surface area void on the plate. And as suspected, the decay in the slope of HTCs identified in section 5.3.2 strongly relates to the growth of the surface area void. An increasing surface area void counteracts on the heat transfer from the working fluid to the wall as the heat transfer coefficient from vapor ammonia to the wall is expected to be lower than from the liquid ammonia to the wall. This effect is shown in Figure 5.29. These results show that partial film flow that includes large surface area voids have a negative effect on the heat transfer.

5.5. Flow pattern map analysis

In section 5.4 a void fraction analysis is performed to get a better understanding of what is happening inside the channel during condensation. This section elaborates on phenomena that influence the behaviour of the flow patterns. This is done by evaluating the observed flow patterns and comparing these to dimensionless numbers that describe the ratio between certain physical phenomena. Second, the flow pattern map proposed by Tao is compared to the observations and experimental conditions of the visualization experiments. At last, a flow pattern map is proposed for the GPHE. The fluid properties of the sets are presented in Table 5.6.

Table 5.6: Average fluid properties of experimental sets

Set	G [kgm^{-2}s^{-1}]	P [kPa]	T [K]	x range [-]	Re_L [-]	Re_V [-]	ρ_L [kgm^{-3}]	ρ_V [kgm^{-3}]	μ_L [Pas^{-1}]	μ_V [Pas^{-1}]	σ [Nm^{-1}]
1	43	681	287	0.22-0.62	492	5917	620	5.36	$1.5*10^{-4}$	$9.5*10^{-6}$	0.0283
2	64	687	287.2	0.19-0.42	891.5	6297	620	5.4	$1.5*10^{-4}$	$9.5*10^{-6}$	0.0282
3	81	682	287.2	0.18-0.31	1223	6307	620	5.37	$1.48*10^{-4}$	$9.5*10^{-6}$	0.0283
4	91	701	288	0.27-0.28	1333	8029	619.1	5.52	$1.47*10^{-4}$	$9.48*10^{-6}$	0.0280
5	88	710	288.4	0.25-0.29	1337	7612	618.6	5.6	$1.46*10^{-4}$	$9.5*10^{-6}$	0.0279

During the sets, the temperature T and pressure P of the working fluid inside the GPHE did not vary much, which is why the average pressure and temperature of every set are presented in the table. One can see that the pressure and temperature did not vary much per set as well. The fluid properties are gained from Refprop, using Matlab, and are a function of the pressure and temperature. This explains why the density, viscosity and surface tension values remain quite constant for all visualization experiments. The Reynolds numbers however, vary strongly because they are a function of mass flux and vapor quality, which differ significantly per set.

5.5.1. Physical phenomena that influence the flow pattern

Figure 5.30 gives a schematic representation of the side view of the channel for certain conditions. Set 1, G = 41 kgm^{-2}s^{-1}, x = 0.62 has the largest volumetric void fraction and surface area void and lowest Reynolds numbers. The liquid film shows a smooth flow. Set 2, G = 64 kgm^{-2}s^{-1}, x = 0.42, the volumetric void fraction and surface area void decrease. The liquid film is still mostly smooth, but also shows rough flow behaviour. For set 3, 4 and 5, the mass flux is between 80 and 91 kgm^{-2}s^{-1} , the volumetric void fraction remains more or less the same, there is no surface area void left and both the liquid and vapor show rough film flow characteristics.

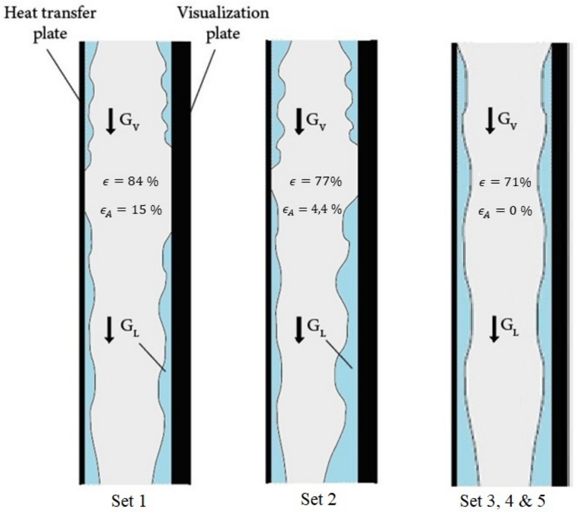

Figure 5.30: Schematic representation of partial film flow, void size and liquid distribution

The results of the previous section show that if the surface area of the plate is not entirely wetted this has a negative influence on the heat transfer. Surface tension is expected to influence the wettability of the plate. A higher surface tension will lead to larger voids. For a lower mass flux, gravity plays a non-negligible role in the downward film flow. If the effect of surface tension is dominant over the gravity forces, it is expected that voids appear on the surface. The inertia of the liquid is expected to have an influence on the wettability as well. If the inertia forces are significantly larger than the surface tension forces, the liquid will spread out over the surface. For some subsets within set 4 and 5, i.e. for higher mass fluxes, a wavy flow was observed. A wavy pattern of the liquid was observed in all windows, but might be due to the piston movement of the process pump. Wavy flow can be observed in downward condensing flow, and is caused by viscous forces that counteract on the gravitational force.

Dimensionless numbers

Dimensionless numbers describe the ratio between physical phenomena and are used to investigate which can or cannot be neglected with respect to another. Dimensionless numbers are compared to the observed flow patterns to determine which phenomena are dominant and which could describe a transition between the partial film and film flow. In the next figures, the color black indicates partial film flow while the red color indicates film flow. The Reynolds number is a dimensionless number that represents inertia force over viscous force, and it is investigated what the influence of the vapor Reynolds number Re_V, liquid Reynolds number Re_L and Reynolds equivalent number are on the observed flow patterns.

Figure 5.31 shows both the Re_V versus Re_L and Re_{eq} versus Re_L. It shows that for all Reynolds numbers, the values are much greater than one, indicating that the inertia force is strongly dominating viscous forces. It can also be observed that both the vapor and equivalent Reynolds number do not contribute greatly in determining the transition from partial film flow to film flow. However, the liquid Reynolds number does play an important role, which is expected since the film Reynolds number showed to be strongly related to the surface area void fraction. A transition line describes the transition from partial film fow to film flow indicated by the black dotted line, described by the following relation:

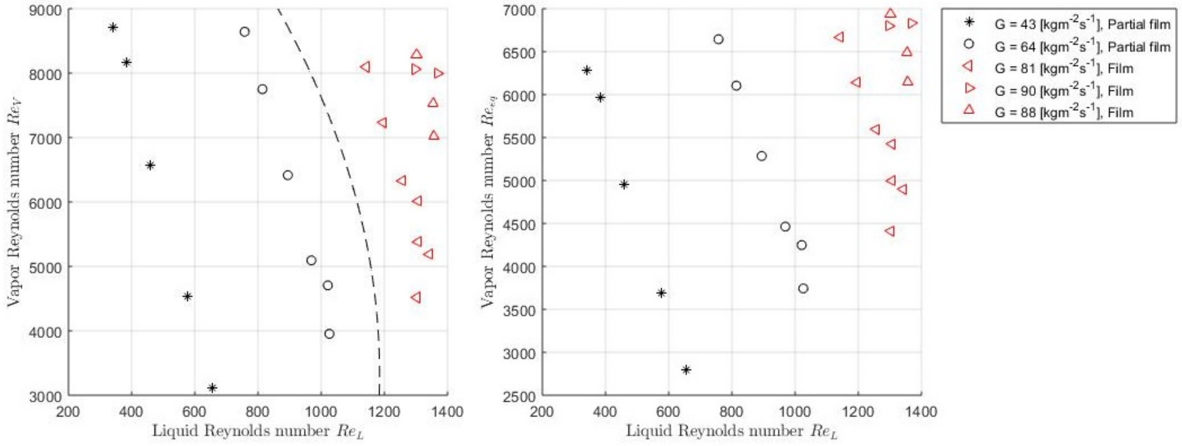

Figure 5.31: Flow patterns for Reynolds numbers in the system. Left) The vapor Reynolds number Re_V versus the liquid Reynolds number Re_L including transition line. Right) The Reynolds equivalent number Re_{eq} versus the liquid Reynolds number Re_L

$$Re_L = c1Re_V{}^2 + c2Re_V + c3 \tag{5.37}$$

Where c_1 = -1E^{-5}, c_2 = 0.0665, and c_3 = 1074. It is only used for the vapor and liquid Reynolds number, because from the visualization experiment it is observed that the flow is strongly separated. The equivalent Reynolds number assumes homogeneous flow, and therefore the vapor Reynolds numbers is used in the relation for the transition line instead of the equivalent Reynolds number.

The Weber number We is the ratio of inertia to surface tension, and both the liquid Weber number We_L and vapor Weber number We_V are presented for each set in Figure 5.32. It shows that for all sets, the liquid Weber number is below 1. This indicates that the surface tension force is non-negligible with respect to inertia force in the liquid. Generally, it holds that for lower liquid Weber values the liquid has a tendency to take on a stronger curved shape on the free surface, i.e. on the surface between the liquid and the vapor. This phenomenon causes the voids. As is expected, the effect of surface tension decreases with higher inertia of the liquid, i.e. when film flow occurs. The effect of surface tension is largest for small mass fluxes and high quality. The vapor Weber number shows that the inertia of the vapor is dominant over the surface tension.

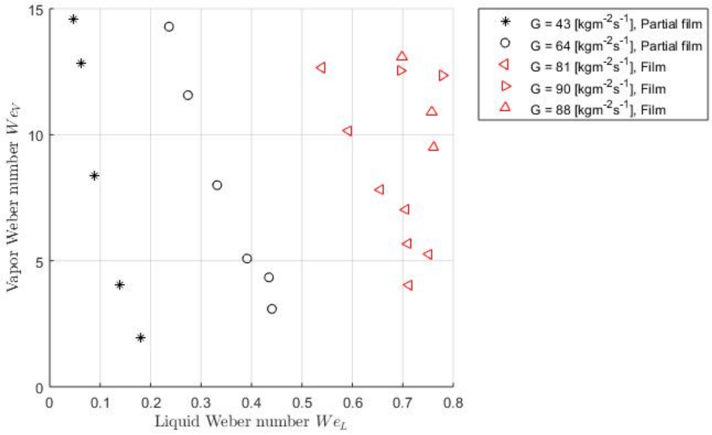

Figure 5.32: Flow patterns for Weber numbers in the system. The vapor Weber number We_V versus the liquid Weber number We_L

Zhao and Rezkallah [59] performed a flow pattern study for a micro-gravity environment and concluded that for $We_V < 1$ the flow pattern was a bubbly flow in a surface tension dominated regime. For $We_V > 20$ the flow behaved as annular flow in an inertia dominated regime. In this study, the vapor Weber number showed an annular flow for $1.9 < We_V < 15$, and the liquid Weber number shows a transitional value from partial film flow to film flow for $We_L \approx 0.5$. However, like Re_L, the transition is dependent on other factors.

The confinement number Co takes the square root of the inverse Bond number Bd, and involves the ratio of surface tension over gravity. The confinement number is used for comparison by Kim et al. [29] for the refrigerant R-245fa in an upward evaporator. In that study it is stated that a confinement number Co below 0.5 no bubble confinement takes place. However, when looking at Figure 5.33, for condensing flow of ammonia this threshold is higher. In this study, no bubbles are observed and $Co > 0.5$ for all sets. Second, the confinement number falls in the same range for every set, meaning that this dimensionless number is not useful for determining a transition between film flow and partial film flow.

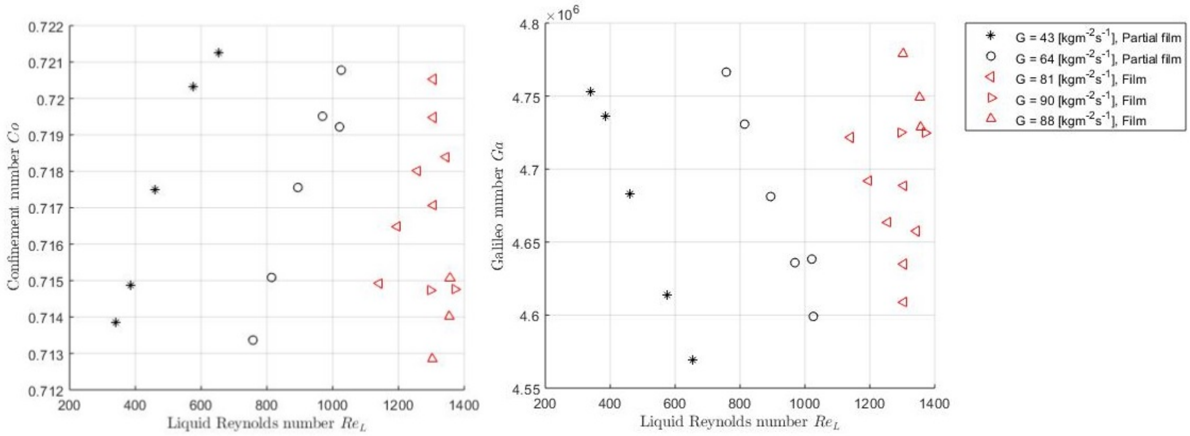

Figure 5.33: Flow patterns for confinement number, Galileo number and liquid Reynolds number. Left). The confinement number Co versus the liquid Reynolds number Re_L. Right) The Galileo number Ga versus the liquid Reynolds number Re_L

The Galileo number is the ratio of gravitational force over viscous force. A wavy flow is characterized by a small Galileo number. A wavy flow was sometimes observed for higher mass fluxes, but it could be due to the piston movement of the pump instead of a result of viscous forces. From Figure 5.33 it could be seen that the gravitational force is much larger than the viscous force, erasing the possibility that the waves were due to viscous forces.

5.5.2. Comparison of flow pattern maps

In this section, the recognized flow patterns of the current study are compared to specific and general flow pattern maps proposed in previous studies. The focus is on film flow and partial film flow, since no other flow patterns are observed within the visualization experiments. In literature, various types of flow pattern maps are proposed, which combine different properties or conditions on their axes. There has been no record of a performed flow visualization for condensing ammonia in a corrugated plate heat exchanger, which stresses the importance to investigate whether the observed flow patterns agree with the expected flow patterns proposed by flow pattern maps. The results of the visualization experiments are presented in several proposed flow pattern maps and compared to studies which overlap in the map.

Flow pattern map based on two-phase Froude number, fluid properties and liquid Reynolds number
Tao et al. [45] proposed a general flow pattern map for vertical PHEs based on the two-phase Froude number Fr_{TP}, a property modifying parameter Λ and the liquid Reynolds number Re_L.

The map includes all the properties that describe the physical phenomena which are considered to be relevant for determining the transition between film flow and partial film flow within the GPHE. The map is based on the experimental results of multiple flow pattern studies ([20],[38],[49],[48],[51],[56]) on PHEs that include various working fluids except ammonia. The experimental conditions are presented in the flow pattern map by Tao in Figure 5.34. This map predicts mostly churn flow for the experimental conditions of the visualization experiments. The visualization experiments however, showed partial film flow and film flow only. For G = 42 and x = 0.2, the map predicts film flow where in the visualization experiment partial film flow is ob-

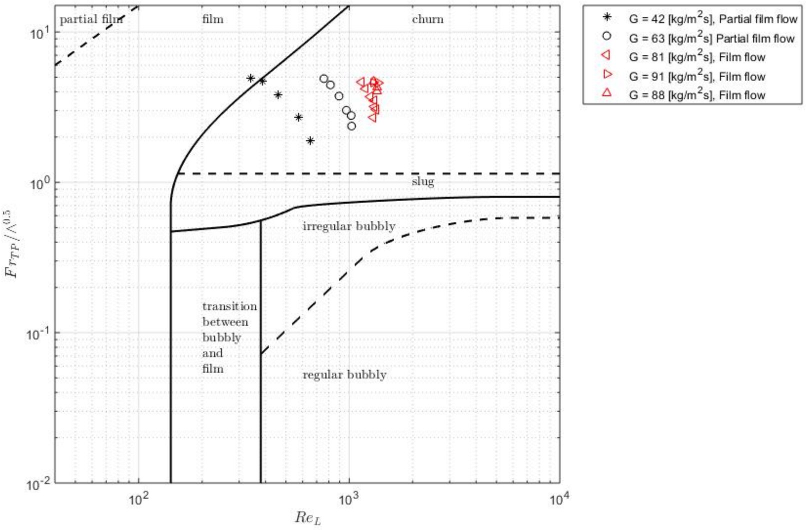

Figure 5.34: The experimental conditions presented in the flow pattern map proposed by Tao et al. [45] for plate heat exchangers

served. This flow pattern map does not predict the right flow pattern for downward condensing ammonia in the GPHE for these experimental conditions. However, the upper side of the flow pattern map (for $\frac{Fr_{TP}}{\Lambda^{0.5}} > 1.8$) is only based on the experimental results of Tribbe & Müller-Steinhagen [48][49] and Winkelmann [56]. It is possible that other transition lines would have been suggested by Tao et al. [45] if more experimental results were available in that range of the map. Tribbe & Müller-Steinhagen [49] did observe air/water film and partial film flow for similar positions on the flow pattern map [45]. In the future, the classified flow patterns and experimental conditions from the visualization experiments can be included in the work of Tao to increase the accuracy of the general flow pattern map proposed by Tao.

Flow pattern maps based on superficial vapor and liquid velocities
Tribbe & Müller-Steinhagen [48][49] ($\beta = 60°$), Vlasiogannis [51] ($\beta = 60°$), Nilpueng & Wongwises [38] ($\beta = 10°/60°$), and Winkelmann [56] ($\beta = 25.7°$) also observed film flow in their studies and based the flow pattern map on the superficial vapor and liquid velocities, which include the inertia of the vapor and the liquid.

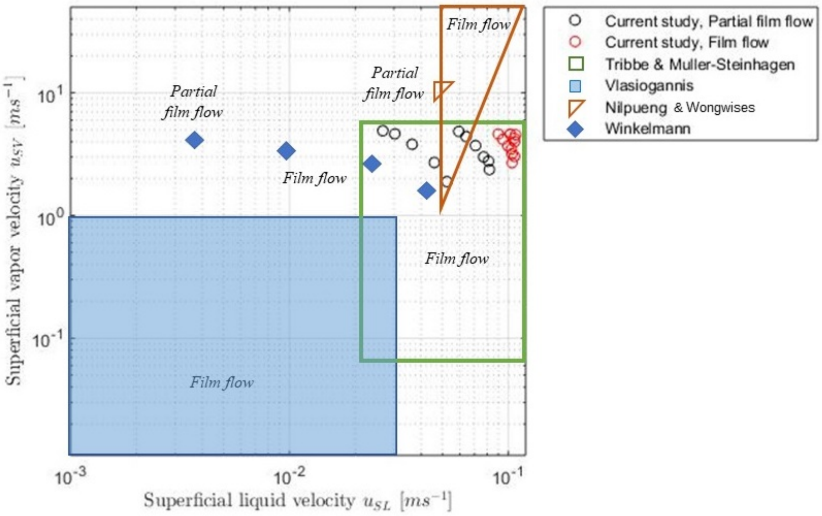

Figure 5.35: The experimental conditions presented in a flow pattern map described by the superficial vapor and liquid velocities

However, the superficial velocity is a function of x, G and $\rho_{L,V}$, thus the map does not include gravity and surface tension which are considered to non-negligible for the condensing process in the GPHE. Second, the hydraulic diameter is not directly involved, which is a function of the corrugation angle. Figure 5.35 shows the experimental conditions of the visualization experiments, and the ranges where partial film and film flow were recognized by previous studies. There seems to be an agreement that partial film flow occurs for lower limits of the superficial liquid velocity. The experimental conditions of Nilpueng & Wongwises and Winkelmann overlap with the current study. The recognized flow patterns by Nilpueng & Wongwises are in best agreement with the recognized flow pattern of the current study. Winkelmann visualized air/water with the lowest corrugation angle and has observed film flow where partial film is observed for the current study. Water has a significant higher surface tension, which makes the film flow observed by Winkelmann contradict the expectations.

Flow pattern maps based on vapor quality and mass flux
Al-Zaidi et al.[3] performed flow visualization in micro-channels with the refrigerant HFE-7100. Jassim et al.[26] investigated the upward flow pattern of R-134a inside a corrugated plate heat exchanger with an angle of $\beta = 60°$. In these studies, the flow pattern maps were based on only vapor quality and mass flux, see Figure 5.36 and solely film flow is observed. There is an overlap between the conditions of Jassim et al. and the current study, where R-134a showed film flow and pure ammonia showed partial film flow. This can be explained by the fact that surface tension of ammonia is approximately a factor 3 larger with respect to R-134a and therefore it is expected that R-134a is less subjected to the occurrence of voids for the same conditions. This stresses the importance of including fluid properties into flow pattern maps.

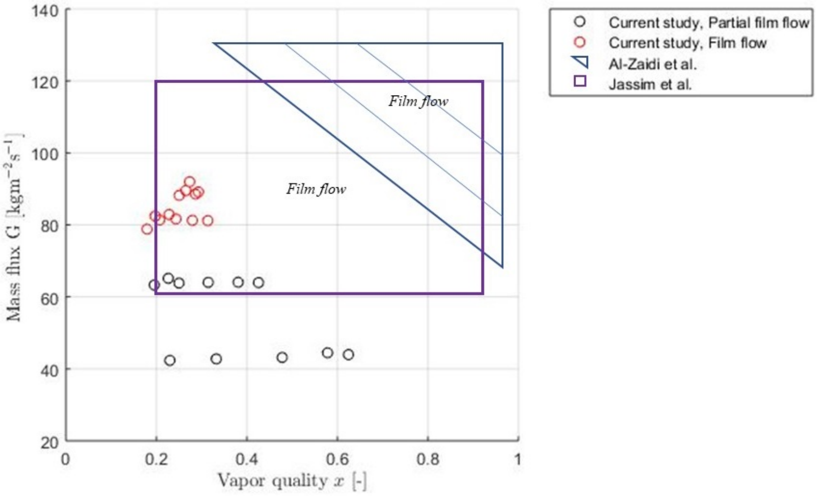

Figure 5.36: The experimental conditions presented in a flow pattern map described by the vapor quality and mass flux

5.5.3. Proposed flow pattern map

A flow pattern map for the downward condensing ammonia in the GPHE is constructed based on the parameters proposed by Tao et al. [45]. As is apparent from the dimensionless numbers analysis, the inertia of the liquid and the surface tension play an important role in determining the transition from partial film flow to film flow and should therefore be included in the flow pattern map. Gravity should not be neglected in the downward condensing flow as well as the corrugation angle which is included in the hydraulic diameter. The flow pattern map proposed by Tao et al. includes all these properties in the axes and is therefore expected to be more relevant than the flow patterns described by G & x or u_{SL} & u_{SV} only. Figure 5.37 presents the proposed flow pattern map for downward condensing ammonia inside a GPHE with a corrugation angle of $\beta = 60°$.

The map includes the experimental conditions of the visualization experiments and the dashed line describes the transition from partial film flow to film flow. At last, an indication for rough film flow and smooth film flow is included that describe the transition from a smooth liquid flow to a rough liquid flow. The proposed

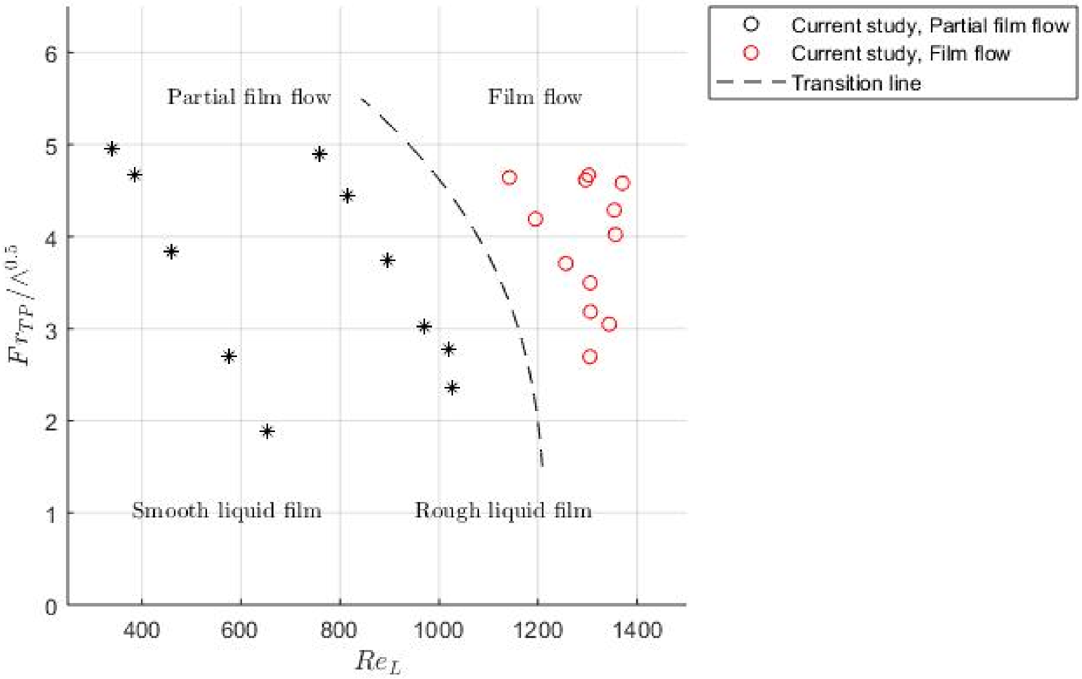

Figure 5.37: The proposed flow pattern map as a function of Fr_{TP}, Λ and Re_L for condensing ammonia inside a corrugated GPHE with a corrugation angle of $\beta = 60°$ describing the transition from partial film to film flow

transition line differs from the proposed transition line by Tao et al. as it is in the opposite direction and more curved. The curve of the proposed transition line is based on the experimental conditions of the visualization study. However, if another experimental plan would have been executed, than the observations and experimental conditions would have differed from the current one. Because the experimental conditions of Winkelmann give a positive linear slope on the map, the transition line follows the same trend. It can be concluded that the experimental approach of a visualization study influences the slope and location of the transition lines.

5.5.4. Conclusions on phenomena that influence the flow pattern

From the analysis of the dimensionless numbers the following can be concluded:

- The liquid Reynolds number Re_L describes the inertia of the liquid over the viscous forces. Re_L showed to play a dominant role in the transition from partial film to film flow. A correlation for Re_L is developed that describes this transition as a function of the vapor Reynolds number Re_V.
- The liquid Weber number of $We_L \approx 0.5$ describes the transition from partial film to film flow with respect to inertia over surface tension. The Weber number indicates that for partial film flow, surface tension forces play a more dominant role than for film flow. This is in accordance with the expectations.
- Inertia and surface tension are identified to play an important role for the experimental conditions in the GPHE. Surface tension and inertia are involved in the transition from partial film to film flow. Gravity may not be neglected and viscous forces appear to have a negligible influence.
- Even though the flow sometimes appeared as a wavy flow, it can be concluded that this is due to the movement of the piston inside the pump and not to the role of viscous forces and therefore cannot be classified as wavy flow

The following can be concluded with respect to the compared flow pattern maps:

- The proposed general flow pattern map for PHEs by Tao et al. [45] does not agree with the experimental conditions of the visualization study and the observed flow patterns. The flow pattern map by Tao et al. predicts mostly churn flow for the conditions where partial film and film flow are observed in the visualization experiments. For one data point, film flow is predicted by the map of Tao et al, where in the visualization experiments partial film flow is observed.
- The constructed transition lines proposed in the flow pattern map by Tao et al. are based on observed flow patterns in previous studies. The transition lines for the upper half of the flow pattern map, i.e. $\frac{Fr_{TP}}{\Lambda^{0.5}} > 1.8$ are based on few experiments. The experimental conditions of the visualization experiments are between $1.8 < Fr_{TP} < 5.0$ and the results of this visualization study can be used to improve the accuracy of the flow pattern map constructed by Tao et al.
- The proposed flow pattern maps by previous studies based on the superficial liquid and vapor velocity shows that partial film flow agrees with a lower superficial liquid velocity, and film flow with a higher superficial liquid velocity. The other studies mostly showed film flow for the conditions where in this study partial film flow is observed, and it is expected that this flow pattern map does not take enough parameters into account such as fluid properties that play an important role in the occurrence of flow patterns. The same holds for the proposed flow pattern maps by previous studies based on the mass flux and vapor quality.
- A flow pattern map for downward condensing ammonia in the GPHE is proposed, based on the two-phase Froude number Fr_{TP}, the liquid Reynolds number Re_L and the fluid property modifying parameter Λ. These parameters include all the parameters that are considered relevant for the occurring flow patterns in the GPHE.
- The transition line between partial film flow and film flow is in opposite direction as the proposed transition line by Tao et al. [45]. It is expected that this is because the transition line is influenced by the performed experimental conditions of the visualization studies. The fewer the amount of experimental results, the more uncertain the shape and location of the transition line becomes. However, it does agree that the partial film flow regime is on the left hand side of the film flow regime.
- It can be concluded that more visualization studies need to be performed in order to optimize the accuracy of general flow pattern maps of PHEs.

6

Conclusions and discussion

In this chapter, the final conclusions of this research are presented by answering the research questions consecutively. Some results and certain statements made in this study are discussed on their accuracy and likeliness. Recommendations are given for future research if certain elements of this experimental research are desired to be repeated. At last, recommendations are given on using certain results of this research for future modelling.

6.1. Conclusions

The main research question of this study is which flow patterns are dominant inside the GPHE of the OTEC demo and how they relate to the performance of the GPHE. The conclusions are given by answering the subquestions and main question of this research.

(i) How are flow patterns identified by previous studies and is there a consistency in the classification of the flow patterns?
Flow patterns are identified in many previous visualization studies, but there has been no record of a visualization study on downward condensing ammonia in a corrugated PHE. It can be concluded that classification of the flow patterns is quite subjective. For this reason, a schematic representation of flow configurations based on the previous visualization studies is proposed to classify the flow patterns in the GPHE. Flow recording is mostly done by use of a high speed camera, and the use has been proven to be sufficient for this study as well with a frame rate of 3000 fps and resolution of 1024 x 1024 pixels. LED-strips have not been used in previous studies but prove to be sufficient and give no complications on reflections or significant addition of heat.

(ii) Which visualization plate material is suitable for the OTEC demo conditions to enable visualization?
An important remark is that in the future, no materials should be selected for producing components in a system that contains a strong chemical, without performing chemical tests first on the material. The chemical charts proposed by companies or literature often do not state the experimental conditions, while the chemical resistance of a material is often very dependent on the test conditions. Glass is not advised to use as a visualization material inside the setup because safety is not guaranteed. The risks for using glass are high as glass is vulnerable to bending and stress concentrations, to which it will be subjected for the conditions inside the GPHE. Second, the available production methods are expensive and time costly. PS proved to be mechanically fit as a corrugated top layer for the visualization plate in the GPHE. PMMA proved to be stiff and strong enough to withstand the pressures during mounting and operation. PS showed a good chemical resistance for at least four days, while PMMA showed to be highly chemically unresistant to ammonia. Therefore, the PS top layer of the visualization plate served as a chemical resistant barrier between the ammonia and PMMA plate. An UV-hardening glue proved to be fit for assembling PMMA onto PS, but the chemical resistance of the glue to ammonia is unknown. The durability of the visualization plate was limited, since the first signs of fatigue started to show after 7 days. The PS layer absorbed the ammonia and it is expected that the loss in opacity is due to a chemical reaction between the glue and ammonia. Eventually, the PS layer showed

cracks and it was considered that the plate was no longer safe after 10 days. The PS/PMMA visualization plate performed well enough to complete a visualization study, but for future research it is not advised to produce a visualization plate from this material and glue combination for pure ammonia visualization experiments.

(iii) Which flow patterns are identified during the single-channel visualization experiments?
Partial film flow and film flow are observed for $43 \leq G \leq 91$ [kgm^{-2}s^{-1}]. No other flow patterns are observed in the visualization experiment. For $G \leq 64$ [kgm^{-2}s^{-1}] partial film flow is observed and for $G \geq 81$ [kgm^{-2}s^{-1}], film flow is observed. A transition is thus observed by increasing G from partial film flow to film flow. Partial film flow shows a surface area void on the transparent plate, indicated by a studded area. Once a surface area void is present on the plate, the size of the void increases with vapor quality. For larger mass fluxes, increasing the vapor quality did not produce surface area void fractions. For $G = 43$ [kgm^{-2}s^{-1}], the liquid film showed smooth characteristics. With increasing G, the smooth film transitioned into a rough film.

(iv) How are the occurring flow patterns related to heat transfer and pressure drop in the GPHE?
The observed partial film flow and film flow occurred for different experimental conditions, and therefore they correspond to different pressure drop and heat transfer behaviour. The pressure drop is strongly increased with both mass flux and vapor quality. Film flow appeared for the higher mass flux range, corresponding to a higher pressure drop over the GPHE. Partial film flow is seen for the lower mass fluxes, and corresponds to a lower pressure drop. For all visualization experiments, $Re_{eq} > 1650$, therefore the condensation mechanism is expected to be convective condensation. In this mechanism, the HTCs increase with mass flux. The overall HTCs and ammonia HTCs are determined. If in the same set the mass flux was (unintentionally) increased a little, the HTCs increased with a large jump. It is therefore concluded that HTCs increase with mass flux. Second, the HTCs of the ammonia increase strongly with vapor quality, but showed different behaviour for partial film flow as compared to film flow. The slope of the HTCs with increasing vapor quality showed linear characteristics for film flow, but the slope for partial film flow showed either a strong buckle or a stabilizing gradient for increasing vapor quality. This means that, after a certain point, the HTCs remained constant while increasing vapor quality. Image processing with Matlab shows that this negative effect on the HTCs for partial film flow is related to the growth of the surface area void on the heat transfer plate. The surface area void fraction on the plate is estimated and related to the film Reynolds number, volumetric void fraction and HTCs. A correlation is fitted for the surface area void fraction ϵ_A to the film Reynolds number Re_f which holds between $60 < Re_f < 230$, which shows a high ϵ_A for a low Re_f and approaches zero when Re_f reaches 230. Once a surface area void is present, the surface area void increases for an increasing volumetric void fraction. An increasing volumetric void fraction generally increases the HTCs for ammonia, but the increase becomes less when the surface area void grows. A surface area void has a negative influence on the HTCs, most probably due to the heat transfer being lower from vapor ammonia to the wall than for liquid ammonia to the wall. It can be concluded that film flow is expected to have the best heat transfer performance, but also creates the largest pressure drop in the GPHE.

(v) Which physical phenomena play a dominant role in the transition between the flow patterns?
The inertia of the liquid is a dominant factor in determining partial film flow and film flow. A higher liquid inertia, represented by a high value for the liquid (film) Reynolds number, distributes the liquid of the channel better on the walls, and film flow is observed. When the liquid inertia is lower, the surface tension becomes a more dominant force and surface area voids are observed on the plate. This is represented by the liquid Weber number. The Reynolds number shows that viscous forces do not play a significant role, while the confinement number shows that gravity plays a non-negligible role in the downward falling film. The Galileo number shows that the observed waves in the flow are not due to to viscous forces, and thus can be related to the pulsating flow generated by the pump.

(vi) Do the observed flow patterns match the proposed flow pattern maps by previous studies for the experimental conditions of the visualization experiments?
The flow patterns observed in the GPHE do not match the predicted flow patterns in the flow pattern map by Tao et al. [45] for the experimental conditions of the visualization experiments. The experimental conditions of the visualization experiment occur in that map for $Fr_{TP} > 1.8$, where the transition lines are based on few experimental studies. The amount of previous experimental studies determines the accuracy of such a constructed flow pattern map, and can explain why the observed flow patterns do not match the predictions of the flow pattern map. The results of these visualization experiments can be used to increase the accuracy of the flow pattern map by Tao et al. [45]. Flow pattern maps based on the superficial velocities or on G versus x, do not show the best agreement, which is expected to be due to the fact that the axes do not include

fluid properties and geometric parameters. For these reasons, a flow pattern map specifically for downward condensing ammonia in the OTEC GPHE is proposed. The map is based on the axes proposed by Tao et al., since these axes include Fr_{TP}, Re_L and Λ and the hydraulic diameter, which contain the identified relevant parameters for downward condensing ammonia in the GPHE.

(vii) Based on the experimental conditions, pressure drop and calculated HTCs of the multi-channel experiments, which flow patterns are expected to occur for multiple channel configurations in the GPHE?
For multi-channel configurations, the mass flux of the ammonia decreases. This means that the liquid inertia for every channel drops and that surface tension becomes more significant. The pressure drop in the multi-channel configuration shows to be more dependent on vapor quality than on mass flux and shows different behaviour than the single-channel configuration. It is expected that the liquid layers covering the channel are very thin which cause the pressure drop to be low. The HTCs show the same behaviour with increasing vapor quality as for the partial film flow observed in the visualization experiments. The HTCs show a clear buckle for $G = 22$ [kgm^{-2}s^{-1}] and $G = 40$ [kgm^{-2}s^{-1}] with increasing vapor quality. The buckle or change in slope is not very apparent for $G = 31$ [kgm^{-2}s^{-1}], but this might be the case if the vapor quality was further increased. It is therefore expected that partial film is occurring in the multi-channel GPHE for these experimental conditions.

The main research question is answered by saying that the performance of the GPHE and the occurring flow pattern are related. Film flow corresponds to a larger pressure drop in the GPHE, while partial film flow contains surface area voids on the heat transfer plate which have a negative effect on the heat transfer. The best condition for GPHE with respect to the performance is a film flow that does not create a very high pressure drop. An optimum is reached when the volumetric void fraction is large enough to create a thin liquid layer covering the channels, and the mass flux is just large enough to ensure that the inertia force of the liquid prevents the occurrence of surface area voids.

6.2. Discussion

Chemical compatibility to materials
It is known that PS is chemically compatible to liquid and vapor ammonia for seven days. If in the future it is desired to produce another plate for visualization, it is advised to perform chemical tests on transparent PP and PSU, since they are expected to have a good resistance to pure ammonia. For ammonia-water tests, it might be the case that the durability of a polymer plate will last longer. Water is not vaporized, which means that the film will consist of both ammonia and all the water present in the channel. This reduces the concentration and the plate is expected to last longer.

Accuracy of heat transfer coefficients
The values of the overall and ammonia HTCs are strongly dependent on the inlet and outlet temperature values of ammonia and water of the GPHE, see Equation 5.14. The most critical temperature is $T_{a,i}$ that can be determined in several ways. The values measured by the temperature sensor located before the inlet of the GPHE can be used, or f.e. the calculated saturated temperature (by Refprop) based on the inlet pressure determined by $P_{a,i} = P_{a,o} + \Delta P_{exp}$. The temperature sensor is not located right before the inlet of the GPHE, and therefore considered to be less accurate than the saturated temperature calculated by Refprop. For the multi-channel experiments, the saturated temperature values calculated by Refprop are used. When this is done for the visualization experiments, the HTCs either become negative or give very high values. However, when the sensor inlet temperature is used, the HTCs are in the same range as the calculated HTCs for the single-channel experiments performed by Tao. For this reason, the inlet temperature sensor values are used instead of the calculated inlet saturated temperature of the ammonia. It is difficult to declare what causes the difference in the calculated HTCs. It might be due to a heat transfer unbalance during the visualization experiments, the water side heat transfer correlation giving too large values, or other temperature sensors that give inaccurate values. More research is required on the factors that influence the accuracy of the HTCs to answer this question.

Volumetric void fraction
Methods proposed in literature are used to estimate the volumetric void fraction. The results are compared to the volumetric void fractions by other correlations, and the results seem reasonable but a deviation from reality is likely.

Image processing for determining surface area void fraction
The surface area void fraction is determined by image processing using Matlab. Image processing is based on the observation that the image of the studded window remained static. The moving film flow showed different pixel values over time. The pixels that changed value over time are subtracted from the average pixel values. This gave a clear distinction between the static region and dynamic region in the image generated by Matlab. At last, a rectangular area is selected for every measurement that represents the square region in the top window. The fact that for every measurement the camera and tripod were adjusted, introduces a small error in converting the surface area void fraction over the selected square to the entire heat transfer area. Second, the stainless steel plate with windows blocks a part of the sight. It is possible, especially for large surface area void fraction numbers, that voids did appear behind the stainless steel pressure plate but could not be seen by the camera. It is therefore possible that some values are under-predicted. On the other hand, the images are processed for surface area voids on the transparent plate, which has not been cooled from the other side. It is possible that the behaviour of the voids on the stainless steel plate behave different due to the cooling on the other side. A large deviation from reality in the determination of the surface area void fraction is therefore likely. However, is does give a first estimation on the fraction and growth for varying experimental circumstances.

Accuracy of the experimental results
During performing the experiments, it was aimed to keep all the conditions as equal as possible while varying one or two parameters. However, due to the limits of the system, the cold water flow could not be kept the same value for all sets but varied significantly. This effects pressure drop and heat transfer results. Second, the system also limited the vapor quality range by increasing mass flux, which influences the judgement of the results. For example, it is noticed that the HTCs for a low mass flux are higher than those with a higher mass flux. But this observation is also due to the fact that the vapor quality range is higher, making it seem that the HTCs are much larger, but the effect is less when the HTCs for varying mass flux for the same vapor quality are compared.

Accuracy of flow pattern observations and flow pattern map
The approach of performing the experiments and the experimental conditions influence how one thinks that the flow patterns are related to transition lines in the flow pattern map. Now, a curve is proposed that represents a transition line between film flow and partial film flow. However, if another approach was executed, such as keeping the vapor quality constant and increasing the mass flux per set, the experimental conditions would have formed another pattern/structure on the flow pattern map. Therefore, it is known that this curve holds for the observations seen in the visualization experiments, but the curve might change its shape when the experimental conditions are changed as well. This note should be taken into account when forming flow pattern maps or making assumptions on the flow pattern behaviour based on flow pattern maps constructed from a small amount of data-points.

6.3. Recommendations

Film flow and partial film flow are observed in the GPHE of the OTEC setup. For future research on flow patterns the following is recommended:

Perform more extensive research of flow patterns of ammonia in plate heat exchangers
The proposed flow pattern map for condensing ammonia is based on a small set of experiments, where due to the limits of the system, the variation of the experimental conditions is not very extensive. Only film flow and partial film flow are observed, while it is recommended to find out for which conditions bubbly, churn and slug flow appear. In this way, a more accurate flow pattern map can be constructed for ammonia and contribute to the accuracy of the general flow pattern map proposed by Tao et al. [45].

Optimize falling film model for predicting heat transfer and pressure drop GPHE
Now the flow configuration and the flow patterns are known inside the GPHE, an optimized model can be written for the GPHE. Geschiere [18] has adapted a falling film absorption model to the operating conditions of the brazed condenser of the Kalina OTEC cycle. This model allows for local prediction of heat and mass transfer for a film flow pattern. Dahlgren [16] generated a model for predicting the pressure drop and heat transfer performance inside the GPHE based on a temperature gradient. A new optimized falling film condenser model can be written for the GPHE that includes elements of the model by Geschiere, Dahlgren and

this study. From this study, the surface area void fraction can be implemented in the model and related to different heat transfer correlations. When partial film flow occurs, it is advised to the model the process in such a way that a Nusselt number is involved that describes the heat transfer from vapor to the wall, instead of from liquid to the wall only. The recognized dominant factors such as surface tension, inertia of the liquid and gravity should be included.

A

Conference paper

Manuscript ID: 746
DOI: 10.18462/iir.icr.2019.746

Flow visualization of ammonia inside a Gasketed Plate Heat Exchanger condenser

Maaike LEICHSENRING[(a)], Xuan TAO[(a)], Carlos INFANTE FERREIRA[(a)], Joost KIRKENIER[(b)]

[(a)] Delft University of Technology
Delft, 2628CB 39, Netherlands, X.Tao@tudelft.nl
[(b)] Bluerise B.V.
Delft, 2612PA 6, Netherlands, j.kirkenier@bluerise.nl

ABSTRACT

Most of the previously published flow pattern maps for plate heat exchangers have been based on air-water experiments. In this study, vertical downward flow of condensing ammonia in a gasketed plate heat exchanger is visualized. Polystyrene is tested on its chemical compatibility to liquid ammonia and proven to be resistant for several days. A 25 mm thick transparent plate has been machined from Polystyrene and Polymethylmethacrylaat with the same corrugation profile as the stainless steel heat transfer plates. The study distinguishes between partial film and film flow and the influence of mass flux and vapor quality is observed. The experimental operational conditions are compared to a flow pattern map of air/water two-phase flow in plate heat exchangers and film transition lines in mini-tubes. The results show that more visualization studies are required to extend the applicability of the flow pattern map for different condensing fluids inside gasketed plate heat exchangers.

Keywords: Two-phase flow, vertical downward flow, flow patterns, plate heat exchangers, flow visualization, ammonia, condensation

1. INTRODUCTION

Plate heat exchangers (PHEs) have a wide range of applications due to their superior performance in relation to favourable heat transfer coefficients (HTCs), compactness, design flexibility and thermal effectiveness (Thulukannam, 2013). However, the two-phase behaviour inside the PHEs is yet not fully understood, resulting in over- or underestimating by several published heat transfer and pressure drop correlations, which are limited by the range of conditions they cover (Amalfi et al., 2016). Tao et al. (2018) conclude that better predictions of flow patterns in plate heat exchangers will improve the calculation of heat transfer and pressure drop. Flow patterns are determined visually by an experimental setup where the flow is observed through a transparent plate. Flow patterns are defined by the geometric configurations of vapor and liquid and are classified into four main flow patterns: bubbly, slug, churn and film flow. The sequence of occurrence is based on the increase of the vapor mass flux. Al-Zaidi et al. (2017), Arima et al. (2008) and Arima et al. (2011) conclude that the average vapor quality also plays a significant role, as it is observed that a low vapor quality corresponds to bubbly flow and a high vapor quality to film flow. It is expected that the various flow patterns relate to different forms of heat transfer inside condensers. Vlasiogannis et al. (2001) conclude that film flow shows particularly favourable heat transfer enhancement as compared to the other flow regimes. Al-Zaidi et al. (2017) compared the flow patterns to the local condensation heat transfer coefficient and concluded that for film flow the heat transfer coefficient (HTC) is largest. A flow pattern map helps distinguish the various regimes in a graphical way. Tao et al. (2018) created a flow pattern map for two-phase vertical downward flow in plate heat exchangers including the property modifying group Λ, see Eq. (1), that enables the inclusion of fluid properties into the flow pattern map.

$$\Lambda = \mu_L \mu_w^{-1} \rho_L^{-1/4} \; \rho_w^{1/4} \; \sigma_L^{-3/4} \sigma_w^{3/4} \qquad \text{Eq. (1)}$$

The axes of the flow pattern map make use of dimensionless groups: the liquid Reynolds number Re_L, and the two-phase Froude number Fr_{TP}, see Eq. (2) and Eq. (3).

$$\mathrm{Re}_L = G(1-x)d_h\mu_L^{-1} \qquad \text{Eq. (2)}$$

$$\mathrm{Fr}_{TP} = xG\big(gd_h\,\rho_G\,(\rho_L-\rho_G\,)\big)^{-0.5} \qquad \text{Eq. (3)}$$

Flow visualization of pure ammonia condensing flow inside a corrugated vertical plate heat exchanger has not been investigated previously. This study compares the results of pure ammonia flow visualization in a vertical downward PHE to the flow pattern map constructed by Tao et al. (2018). Section 2 explains the experimental setup and the performed research to enable the construction of a durable transparent test plate. Section 3 explains the test procedure and section 4 discusses the results of the visualization experiments.

2. EXPERIMENTAL SETUP

2.1. Experimental Apparatus and Procedure

In cooperation with the Delft University of Technology, Bluerise B.V. constructed a small scale OTEC-plant to test the performance of the OTEC-cycle and optimize its outputs. The 100 W OTEC demo consists of an Organic Rankine cycle using pure ammonia as the working fluid. Figure 1 shows a schematic representation of the experimental setup.

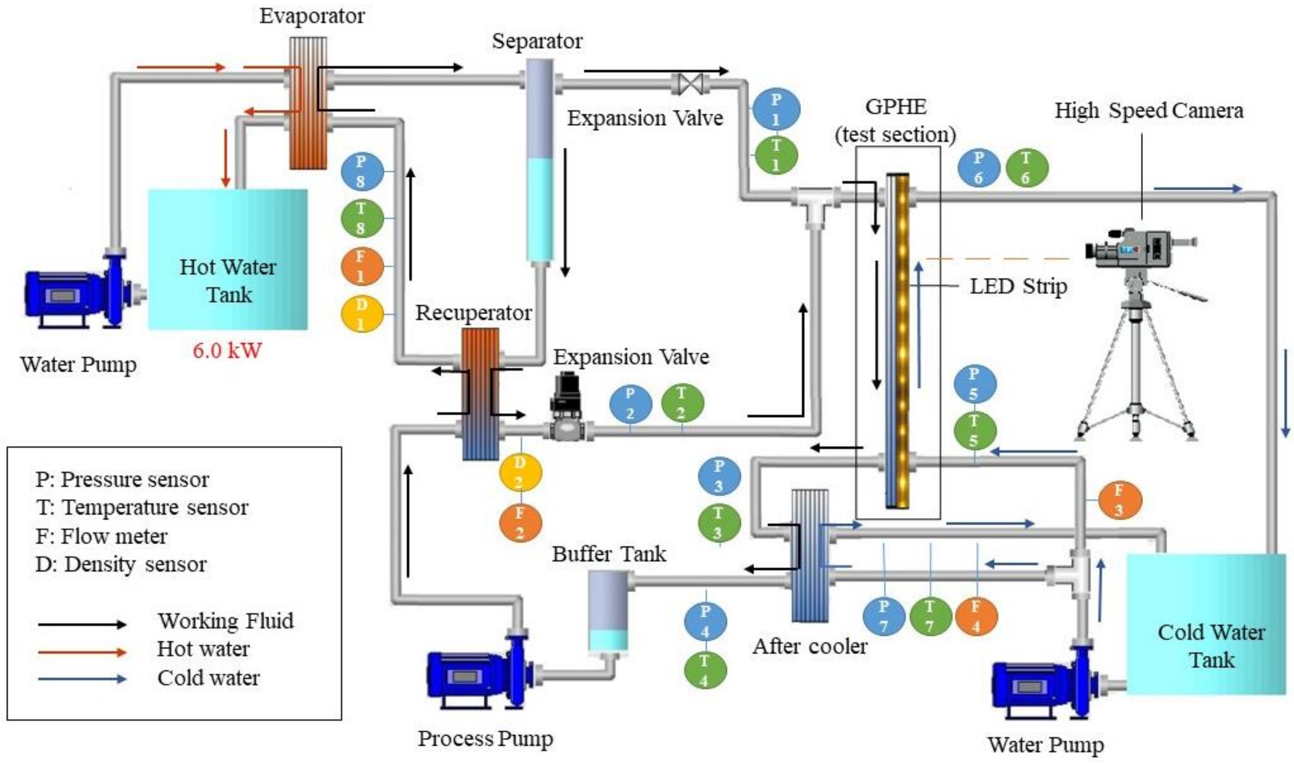

Figure 1: Experimental setup diagram of OTEC demo cycle

Pure ammonia is vaporized while flowing through the evaporator due to the counter current hot water flow. The separator splits the remaining liquid ammonia from the vapor and sends it to the recuperator, which acts as a preheater for the ammonia that is to be heated. The pure ammonia vapor is sent through a turbine and is reunited with the ammonia liquid right before the test section. The two-phase working fluid is condensed in the Gasketed Plate Heat Exchanger (GPHE) by a cold water stream from the cold water tank. A sub-cooler and buffer tank are placed to guarantee that all vapor in the working fluid flow is fully condensed by the time it reaches the process pump. The hot water tank is heated by a heating coil and the cold water tank is connected to a refrigeration system.

2.2. Test Section for Visualization

The test section is a GPHE, containing a cold water channel and a working fluid channel. Table 1 gives the detailed geometric parameters of the stainless-steel plate used for heat transfer.
Figure 2 shows its schematic diagram.

Table 1: Geometric parameters of the heat transfer plates

Channel gap d_g	1.72 (mm)	Plate length $\mathrm{L_v}$	0.668 (m)
Chevron angle β	63 (°)	Plate pitch p_{cp}	2.3 (mm)
Corrugation pitch p	7.5 (mm)	Plate thickness d_p	0.58 (m)
Corrugation wavelength Λ_{wave}	6.67 (mm)	Plate width L_h	0.06 (m)
Effective heat transfer area A_e	0.537(m^2)	Port diameter D_p	0.035 (m)
Effective width heat transfer L_w	0.095 (m)	Thermal conductivity κ	16.3 (W.m $^{-1}$K $^{-1}$)

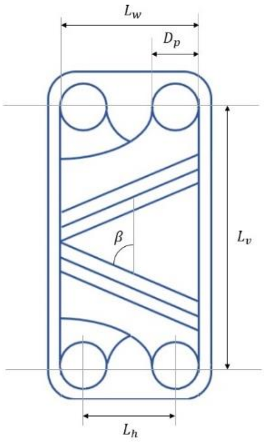

Figure 2: Schematic representation of the corrugated heat transfer plates of the GPHE

The PHE includes a 95 cm x 12.5 cm transparent corrugated polymer plate that enables visualization of the condensing ammonia on the working fluid side. This visualization plate has the same geometric specifications as the heat transfer plate except for the plate thickness, which is 25 mm. The plate is illuminated by a 500 cm LED strip including 300 LED's that encircles the plate from its sides twice. A 3000 fps high speed camera is placed in front of the visualization plate to capture the flow patterns under varying operating conditions. Figure 3 shows the transparent polymer plate, the visualization section including pressure plate and illumination and the placement of the camera.

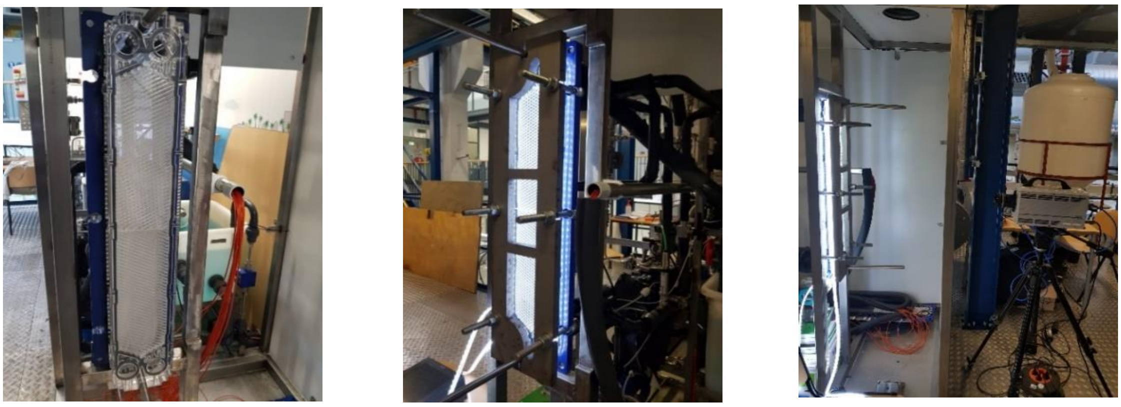

Figure 3: Left) Corrugated visualization plate. Middle) Visualization section including illumination and pressure plate. Right) Visualization section and high speed camera

2.3. Material Selection of Visualization Plate

The challenge is finding a material that meets the following criteria: Chemically compatible to ammonia, transparency, high strength (able to withstand an operational pressure up to 12 bar) and machinable into the corrugation patterns. Arima et al. (2011) and Xue et al. (2013) use glass in front of a flat plate. However, machining a brittle material such as glass into a corrugation pattern contains large risks on mechanical performance due its brittle structure (Lutgendorf, 2014). The latter stresses the importance of finding a polymer (as is used by Al-Zaidi et al. (2017), Grabenstein et al. (2016), Jassim et al. (2006), Tribbe & Muller-Steinhagen (2001) and Vlasiogannis et al. (2001)) that meets the requirements. According to the material database CES Edupack (2018), Polystyrene (PS) is a polymer that meets the optical, mechanical and machinability criteria. Generally, it is stated that this material is chemically compatible to ammonia (CES Edupack, 2018) but it is not mentioned for which experimental conditions this applies such as phase, temperature, pressure and the ammonia being a pure fluid or a diluted mixture. Woishnis and Ebjesajjad (2012) show an extensive research on PS stating that PS is highly compatible to an aqueous solution with 25% ammonia at room temperature for years, but no data is found for pure ammonia. Therefore, several samples are placed in a pressure vessel filled with pure, liquid ammonia at a pressure of 8 bar absolute and ambient temperature for four days. The samples are machined into the desired corrugated pattern, compressed onto each other by two stainless steel clamps.

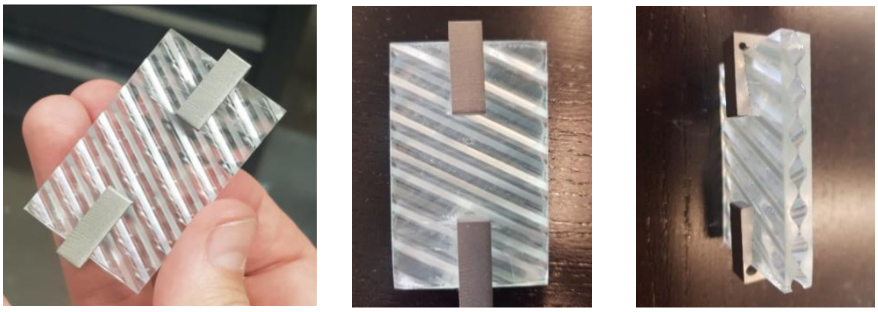

Figure 4: Left) Samples before test. Middle) Frontal view samples after test. Right) Top view samples after test

Fig. 4 shows the clamped corrugated samples before and after the test. The material shows a slight bend and tiny damages on the locations of contact between the samples, but it did not reduce the transparency significantly. A sheet of PS has a maximum thickness of 4.75 mm, onto which the corrugated pattern is machined by a CNC-machine. The corrugated PS sheet is glued with a UV light curing adhesive onto a PMMA plate of 20 mm thickness to benefit from the superior mechanical properties that PMMA has relative to PS.

3. TEST PROCEDURE

The ammonia mass flux G_a is determined by Eq. (4). The ammonia mass flow $\dot{m}_a$ is measured by flow meter F1, see Figure 1. The flow passage area A_f is calculated by multiplying L_w, the effective heat transfer width with d_g, the channel gap.

$$G_a = \dot{m}_a A_f^{-1}$$ Eq. (4)

The single phase condition at the outlet of the after cooler is used to determine the enthalpy of the liquid ammonia. The average quality $\bar{x}$ inside the GPHE is determined by Eq. (5). An energy balance is used to determine the two-phase enthalpy at the inlet of the after cooler, which is assumed to be the same as the enthalpy at the outlet x_{out} of the GPHE. A second energy balance determines the enthalpy of the ammonia at the inlet of the GPHE x_{in} which is determined by Eq. (6). $h_{L,sat}$ and $h_{V,sat}$ represent the saturated liquid and vapour phase enthalpy of the ammonia at the inlet conditions of the condenser.

$$\bar{x} = 0.5(x_{in} + x_{out})$$ Eq. (5)

$$x_{in} = (h_{in} - h_{L,sat})\left(h_{V,sat} - h_{L,sat}\right)^{-1}$$ Eq. (6)

Experiments are performed where the mass flux G_a is kept constant and the vapor quality x_{in} is increased. Both the influence of the mass flux and inlet quality on the flow configurations are recorded for the top, middle and bottom windows.

4. EXPERIMENTAL RESULTS

For all recorded conditions, a framerate of 3000 fps with a resolution of 1024 x 1024 pixels is used. The transparent plate remained intact for 7 days, but on the 8th day of performing experiments degradation in the material was visible in the form of small cracks in the PS surface and crystal shaped spots between the PS and PMMA layer that grew in size over time. It is concluded that PS has a limited durability when in contact with pure ammonia.

4.1. Flow Pattern and Path over the Length of the Heat Transfer Plate

For all performed experiments, no bubbles, slugs or churns were detected and only film flow and partial film flow are observed. The path of the flow remained similar under the various circumstances. Figure 5 shows the path of the flow over the different windows. Due to the shapes of the distribution zone at the inlet, the liquid flow is pushed to the left which causes most of the liquid flow to disperse over the left upper diagonal of the window. It is expected that in that zone also vapor is present, but less than in the lower diagonal.

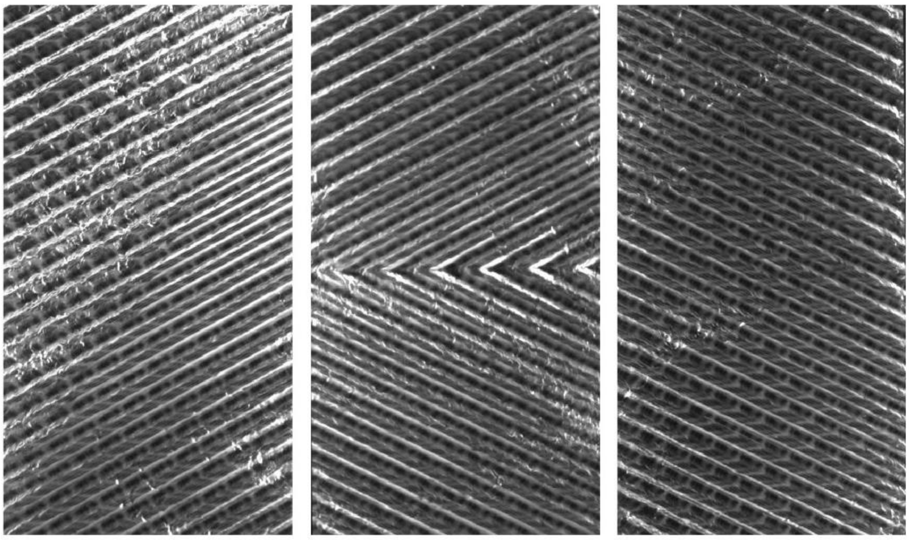

Figure 5: G = 91 kg/m^{2}s, $\overline{x}$ = 0.27. Left) Top window. Middle) Middle window. Right) Bottom window

The area of the upper diagonal covered by mainly a rough liquid film decreases for smaller mass fluxes. This area is indicated by the zones that reflect light in various directions. Most of the vapor flows at the lower diagonal of the top window, indicated by a still image. In the middle window the corrugation direction switches and this sudden change in flow direction causes the liquid to evenly distribute over the corrugations in the lower part of the middle window. Less vapor is detected. The bottom window is mostly covered in a smooth liquid film.

4.2. Influence of Vapor Quality and Mass flux on flow configuration

A distinction can be made between film flow and partial film flow, see Figure ***6***. Film flow includes a liquid layer on both plates while partial film flow leaves dry patches when the amount of liquid film is limited and unable to cover the entire plate. If partial film flow occurs in the GPHE and dry patches are present on the transparent plate, an opaque surface will be visible.

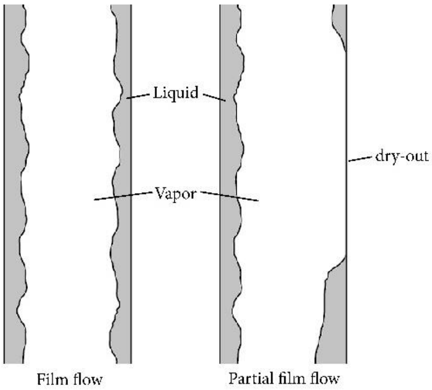

Figure 6: Schematic representation of film flow and partial film flow inside the channel (side view of GPHE)

The distribution of the vapor phase and liquid phases differs at varying circumstances, see Figure 7. Only the top window is represented in the figure since this window shows the varying configurations most clearly.

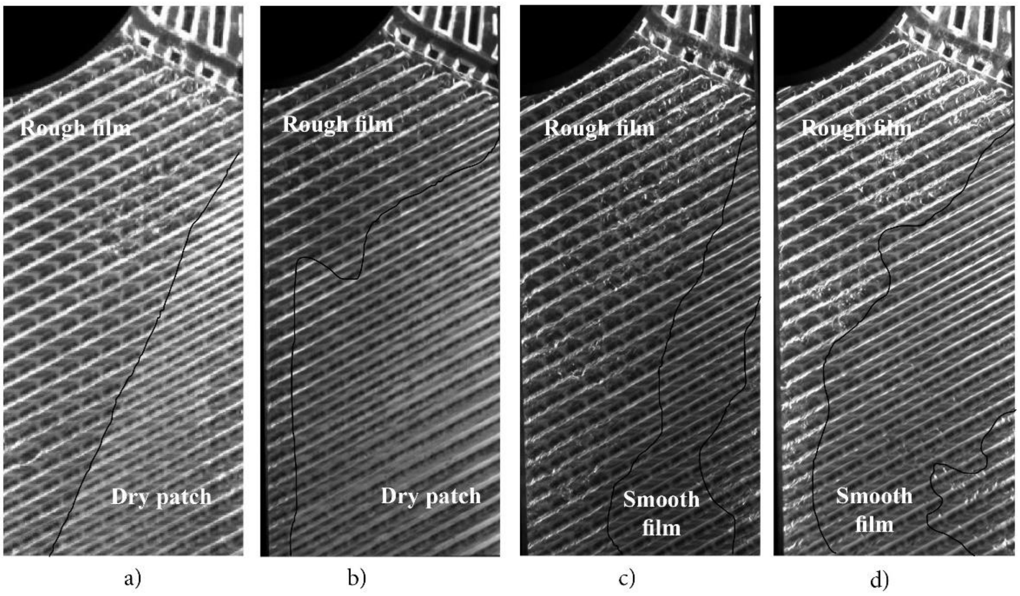

Figure 7: a) G = 43 kg/m^{2}s, x_{in} = 0.26. b) G = 43 kg/m^{2}s, x_{in}= 0.69. c) G = 81 kg/m^{2}s, x_{in}= 0.19. d) G = 81 kg/m^{2}s, x_{in}= 0.34

From Figure 7 a, b, at a constant mass flux but increasing vapor quality the vapor contact area increases. With a lower mass flux, the contact between the transparent plate and vapor turns the surface opaque, indicating a zone of dry-out, i.e. partial film flow. With a higher mass flux, Figure 7 c, d shows an enhanced rough film flow of the upper diagonal, in the figure indicated by the higher amount of light reflectance. The lower diagonal shows a clear surface, even when the vapor quality is increased, indicating film flow. An increased liquid entrainment in the lower diagonal wets the surface of the transparent plate that causes the clarity of that area. The lower diagonal shows no light reflectance indicating a smooth film flow, see Figure 7 c, d.

4.3. Comparison of Results to Flow Pattern Map by Tao et al. (2018)

The operating conditions of the experiments are represented in Fig. 8. Fig. 8 shows a flow pattern map constructed by Tao et al. (2018) for plate heat exchangers that makes use of the dimensionless quantities Re_L and Fr_{TP} which account for gravity, viscous forces, inertia and fluid properties. This construction is based on results from previous visualization experiments for two-phase vertical downward flow of mainly air-water mixtures in plate heat exchangers. The viscosity, surface tension and vapour-liquid density ratio of ammonia locate its operating conditions at high values of the y-axis. In this operating range also Tribbe & Muller-Steinhagen (2001) have identified film and partial film flow conditions. Fig. 8 also shows the film and film-slug transition lines which apply for mini-tubes (see Tao et al., 2018). This indicates that the film transition line, most probably, is located at higher values of Re_L than expected from the air-water experiments. More visualization studies with a wider range of experimental conditions on condensing flow of pure ammonia in vertical PHE's are required to accurately describe the flow pattern behaviour of pure ammonia in this type of heat exchangers and extend the applicability of the flow pattern map for different fluids.

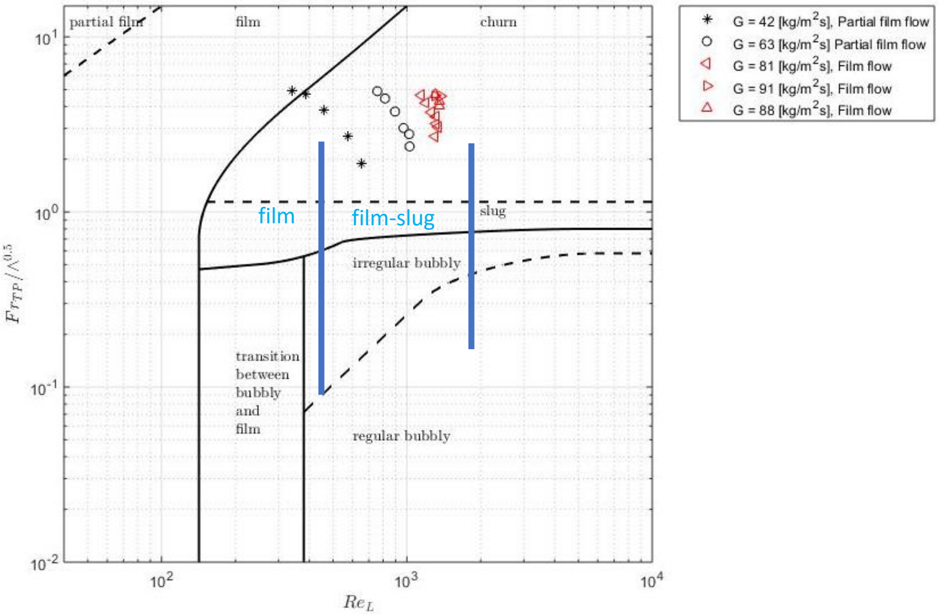

Figure 8: Experimental operating conditions shown in simplified flow pattern map of two-phase flow in PHEs by Tao et al. (2018) based on air/water data, including the film transition lines in mini-tubes (indicated with blue lines) reported by Tao et al. (2018)

5. CONCLUSIONS

The flow morphology of pure ammonia in a vertical downward GPHE has been captured. A corrugated visualization plate is produced from transparent PS by a CNC-machine and has proven to be chemically compatible to pure ammonia for several days and mechanically resistant to a condensation pressure up to 7 bar absolute. For all conditions introduced, film flow and partial film flow is observed. The flow patterns were most visible on the top window, where most of the liquid phase covers the left upper diagonal and most of the vapor the lower diagonal of the window. An increased vapor quality increases the area of dry-out (partial film flow) on the visualization plate. Increasing the mass flux enhances the rough film flow, creating more liquid entrainment in the lower diagonal resulting in film flow. The operating conditions during the performed ammonia condensation experiments (liquid Reynolds number and two-phase Froude number) have been indicated in the flow pattern map constructed by Tao et al. (2018). The results indicate that the film flow and partial film flow transition line needs to be moved to higher values of the Re_L than indicated in the flow pattern map which is mainly based on air-water experiments. More visualization studies are required to extend the applicability of the flow pattern map for different condensing fluids inside GPHE's.

ACKNOWLEDGEMENTS

The authors would like to acknowledge the financial support from the China Scholarship Council and Koudegroep Delft-Wageningen.

NOMENCLATURE

Abbreviations		p	Corrugation pitch [mm]
GPHE	Gasketed plate heat exchanger	p_{cp}	plate pitch [mm]
HTC	Heat transfer coefficient	Re	Reynolds number [-]
LED	Light emitting diode	x	Vapor quality [-]

OTEC	Ocean thermal energy conversion	$\bar{x}$	Average vapor quality [-]
PHE	Plate heat exchanger	*Greek*	
PMMA	Polymethylmethacrylaat	β	Chevron angle [°]
PS	Polystyrene	Λ	Property modifying parameter [-]
Symbols		Λ_{wave}	Corrugation wavelength [mm]
A_e	Effective heat transfer area [$\mathrm{m^{2}}$]	κ	Thermal conductivity [$\mathrm{Wm^{-1}K^{-1}}$]
A_f	Flow passage area [$\mathrm{m^{2}}$]	μ	Dynamic viscosity [Pas]
d_g	Channel gap [mm]	ρ	Density [$\mathrm{kgm^{-3}}$]
d_h	Hydraulic diameter [m]	σ	Surface tension [$\mathrm{Nm^{-1}}$]
d_p	Plate thickness [mm]	*Subscripts*	
D_p	Port Diameter [m]	a	Ammonia
Fr	Froude number [-]	G	Gas
g	Gravitational constant [m$\mathrm{s^{-2}}$]	in	Inlet conditions
G	Mass flux [$\mathrm{kgs^{-1}m^{-2}}$]	L	Liquid
h	Enthalpy [$\mathrm{Jkg^{-1}}$]	out	Outlet conditions
L_h	Plate width [m]	*sat*	Saturated
L_v	Plate length [m]	*TP*	Two-phase
L_w	Effective heat transfer width [m]	V	Vapor
$\dot{m}$	Mass flow [$\mathrm{kgs^{-1}}$]	w	Water

REFERENCES

Al-Zaidi, A., Mahmoud, M. & Karayiannis, T., 2017. Condensation flow patterns and heat transfer in horizontal microchannels. Experimental Thermal and Fluid Science 90, 153-173.

Amalfi, R., Vakili-Farahani, F. & Thome, J., 2016. Flow boiling and frictional pressure gradients in plate heat exchangers. International Journal of Refrigeration 61,166-184.

CES Edupack 2018, Granta Design Limited.

Arima, H., Kim, J., Okamoto, A. & Ikegami, Y., 2008. Local boiling heat transfer characteristics of ammonia in a vertical plate evaporator. International Journal of Refrigeration 33, 359-370.

Arima, H., Okamoto, A. & Ikegami, Y., 2011. Local boiling heat transfer characteristics of ammonia/water binary mixture in a vertical plate evaporator. International Journal of Refrigeration 34, 648-657.

Grabenstein, V., Plzin, A. & Kabelac, S., 2016. Experimental investigation of the flow pattern, pressure drop and void fraction of two-phase flow in the corrugated gap of a plate heat exchanger. International Journal of Multiphase Flow 91, 155-169.

Jassim, E., Newell, T. & Chato, J., 2006. Two-phase flow visualization in chevron and bumpy style flat plate heat exchangers. Heat transfer Engineering 27, 20.

Kim, H., Liebenberg, L. & Jacobi, A., 2018. Flow Visualization of Two-Phase R-245fa at Low Mass Flux in a plate Heate Exchanger near the Micro-Macroscale Transition. Proceedings of the 17th International Refrigeration and Air Conditioning Conference, Indiana, U.S.

Lutgendorf, J., 2014. Structural design of glass geometries, Delft: Delft University of Technology.

Tao, X., Nuijten, M. & Infante Ferreira, C., 2018. Two-phase vertical downward flow in plate heat exchangers: Flow patterns and condensation mechanisms. International Journal of Refrigeration 85, 489-510.

Thulukannam, K., 2013. Heat Exchanger Design Handbook. Taylor & Francis Inc., Boca Raton

Tribbe, C. & Muller-Steinhagen, M., 2001. Gas/Liquid flow in plate-and-frame heat exchangers - Part II: Two-phase multiplier and flow pattern analysis. Heat transfer engineering 22, 12-21.

Vlasiogiannis, P., Karagiannis, G., Argyropoulos, P. & Bontozoglou, B., 2001. Air-water two-phase flow and heat transfer in plate heat exchanger. International Journal of Multiphase Flow 28, 757-772.

Woishnis, W. A. & Ebnesajjad, S., 2012. Chemical Resistance of Thermoplastics. William Andrew Publishing, Norwich.

Xue, Z., Qu, W. & Xie, M., 2013. Full visualization and startup performance of an ammonia pulsating heat pipe. Propulsion and power research 2(4), 263-268.

B

Finite Element results

The results of the FEA element presented by Solidworks Simulations are presented below.

B.1. PMMA

FEA results of the maximum principle stresses in the PMMA plate due to tightening of the bolts up to 100 Nm, see Figure B.1 and Figure B.2.

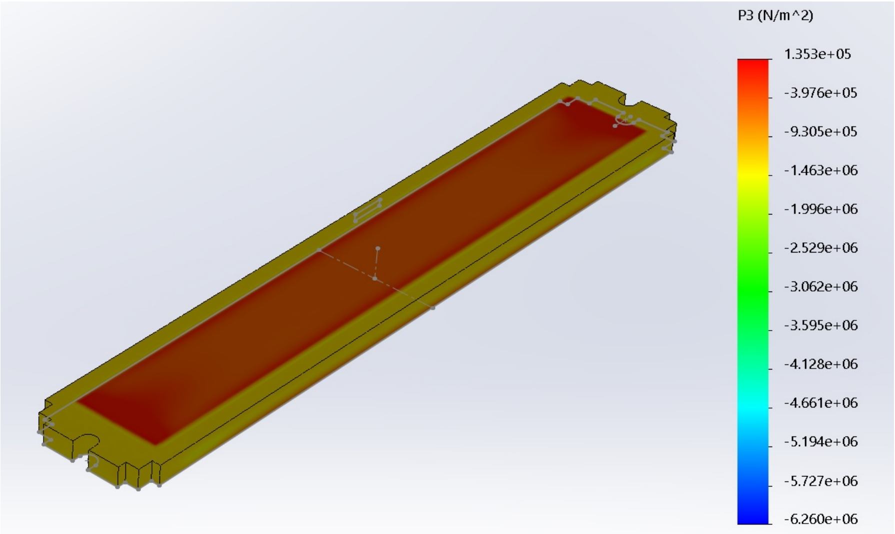

Figure B.1: Range of principle stress in PMMA plate due to tightening of the bolts up to 100 Nm

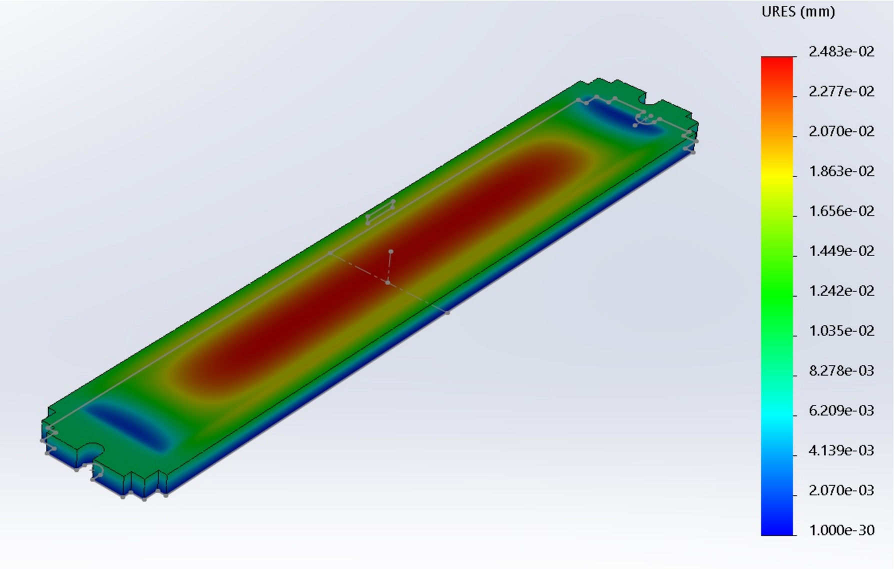

Figure B.2: Range of PMMA plate displacement due to tightening of the bolts up to 100 Nm

Figure B.4 and B.3 present the FEA calculations of the maximum principle stresses and displacements due to bending during an operational pressure of 12 bar.

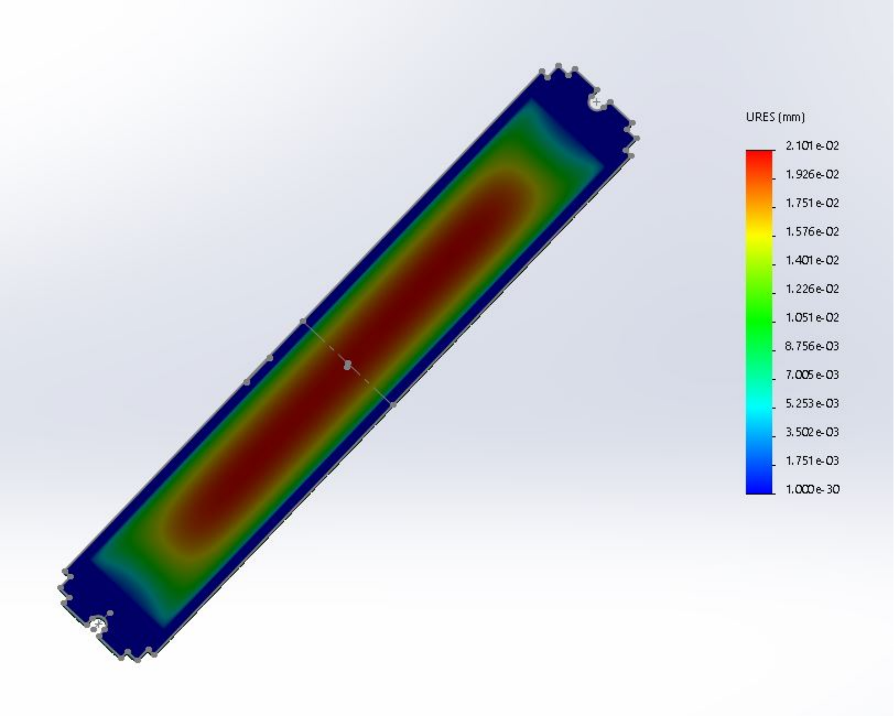

Figure B.3: Range of PMMA plate bending displacement due to an operational pressure of 12 bar

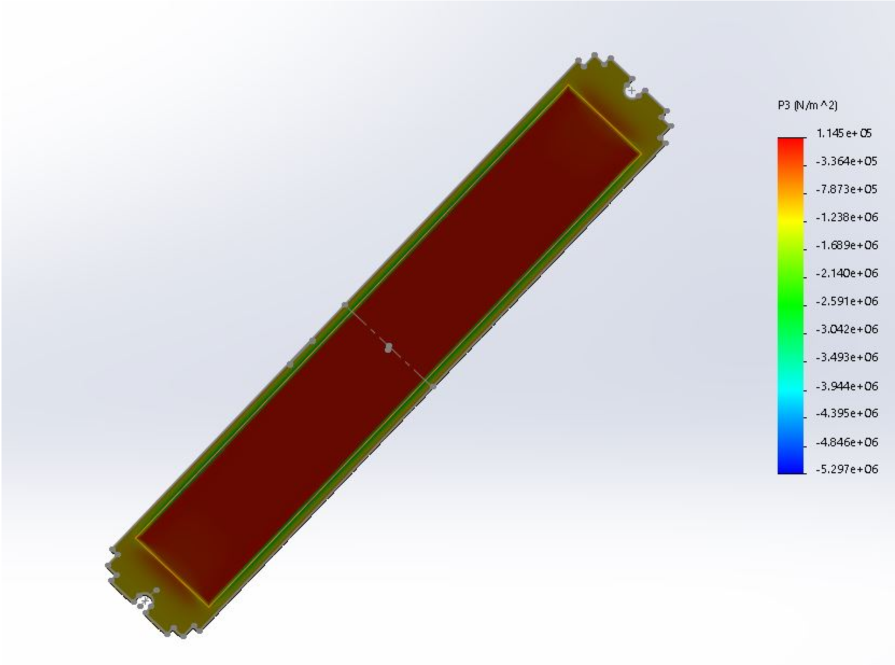

Figure B.4: Range of principle stresses in PMMA plate bending due to an operational pressure of 12 bar

B.2. Glass

The FEA calculations are given for glass of bending due to an operational pressure of 12 bar. Figure B.5 and B.6 give the maximum principle stress and displacement of the glass plate.

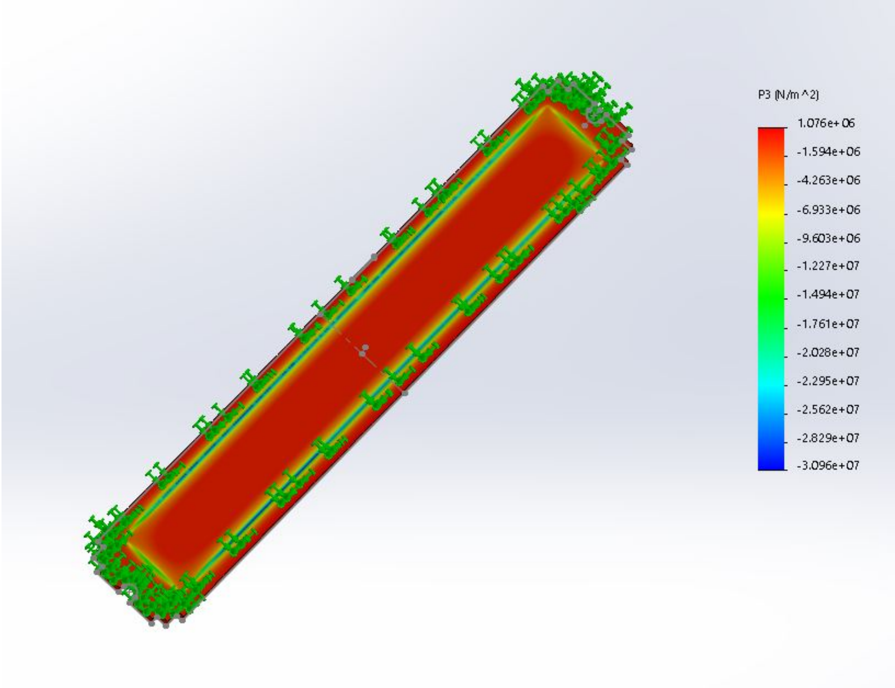

Figure B.5: Range of Principle stresses for bending glass plate due to an operational pressure of 12 bar

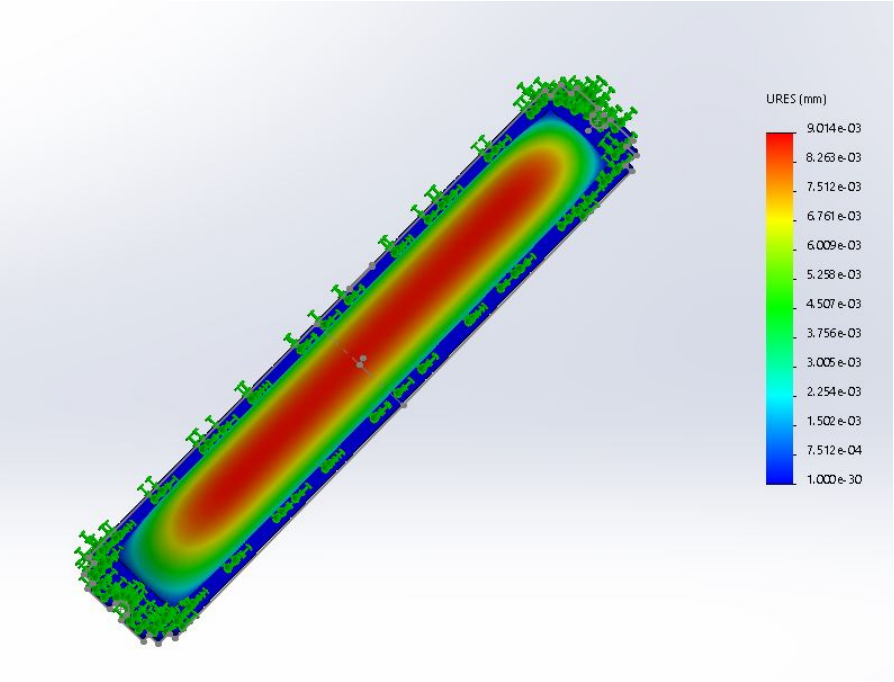

Figure B.6: Range of displacement for bending glass plate due to an operational pressure of 12 bar

Bibliography

[1] W. W. Akers, H. A. Deans, and O. K. Crosser. Condensing heat transfer within horizontal tubes. *Chem. Eng. Progr*, 54:89–90, 1958.

[2] J. Ed Akin. *Finite Element Analysis Concepts via Solidworks*. World scientific publishing Co. Pte. Ltd., 2010.

[3] A. Al-Zaidi, M. Mahmoud, and T. Karayiannis. Condensation flow patterns and heat transfer in horizontal micro-channels. *Experimental thermal and fluid science*, 90:153–173, 2017.

[4] A. A. S. Alshqirate, M. A. Hammad, and M. Tarawneh. Parameters affecting heat transfer during condensation inside micro-pipes: surface tension effect. *Exp. Heat transfer*, 28:405–416, 2015.

[5] R. Amalfi, F. Vakili-Farahani, and J. Thome. Flow boiling and frictional pressure gradients in plate heat exchangers. *International Journal of Refrigeration*, 61:166–184, 2016.

[6] H. Arima, J. Kim, A. Okamoto, and Y. Ikegami. Local boiling heat transfer characteristics of ammonia in a vertical plate evaporator. *International Journal of Refrigeration*, 33:359–370, 2008.

[7] H. Arima, A. Okamoto, and Y. Ikegami. Local boiling heat transfer characteristics of ammonia/water binary mixture in a vertical plate evaporator. *International journal of refrigeration*, 34:648–657, 2010.

[8] H. Asano, N. Takenaka, T. Wakabayashi, and T. Fujii. Visualisation and void fraction distribution of downward-gas liquid two=phase flow in a plate heat exchanger by neutron radiography. *Nuclear instruments and Methods in Physics Research Section A: Accelerators, spectrometers, detectors and associated equipment*, 542:154, 2005.

[9] J.W.M. Bush. Interfacial phenomena. *Massachusetts Institute of Technology*, 2013.

[10] D. Butterworth. A comparison of some void-fraction relationships for co-current gas-liquid flow. *International Journal of Multiphase Flow*, 1:845–850, 1975.

[11] Eriks B.V. Resistance to chemical agents. `https://solutions-in-plastics.info/nl`. [Accessed 20-10-2018].

[12] W.D. Callister. *Materials Science and Engineering, an Introduction*. John Wiley & Sons, 2007.

[13] T.S. Carswell and H.K. Nason. Effect of environmental conditions on the mechanical properties of organic plates. *Symposium on Plastics*, 1944.

[14] D. Chisholm. Two-phase flow in pipelines and heat exchangers. *Heat transfer Engineering*, 6:48–57, 1983.

[15] J. G. Collier and J.R. Thome. *Convective Boiling and Condensation*. Clarendon press, Oxford, 1994.

[16] M.E. Dahlgren. Experimental study of transport phenomena in condenser of an otec-cycle. Master's thesis, Delft University of Technology, 2018.

[17] Gammacril. Chemical resistance p.m.m.a. `http://www-eng.lbl.gov/~shuman/XENON/MATERIALS&COMPONENTS/TMA_PMMA/Acrylic-Rod-and-Tube_chemical-resistance.pdf`, 2018. [Accessed:15-10-2018].

[18] F. Geschiere. Modelling and model validation of the performance of an ammonia-water otec condenser heat exchanger using advanced condenser models. Master's thesis, Delft University of Technology, 2018.

[19] R. Goudriaan. Performance analysis of ammonia and ammonia-water as working fluids for otec power plants. Master's thesis, Technical University Delft, 2016.

[20] V. Grabenstein, A. E. Polzin, and S. Kabelac. Experimental investigation of the flow pattern, pressure drop and void fraction of two-phase flow in the corrugated gap of a plate heat exchanger. *International Journal of Multiphase Flow*, 91:155–169, 2016.

[21] R. Haj-Ali, B.S. Wei, J. Choi, and R. Popil. Refined nonlinear finite element models for corrugated fiberboard. *Composite Structures*, 87:321–333, 2009.

[22] F. Incropera, D. Dewitt, T.L. Bergman, and A.S. Lavine. *Fundamentals of Heat and Mass Transfer.* John Wiley & Sons, 2002.

[23] Cyro Industries. Acrylite - chemical resistance in general use. `http://www.sdplastics.com/acryliteliterature/1554BChemResistanceChart.pdf`, 2001. [Accessed:15-10-2018].

[24] Nederlands Normalisatie Instituut. Nen 2608,2014: Glass in building, requirements and determination method, 2014.

[25] T.A. Jankowski, E.N. Schmierer, F.C. Prenger, and S.P. Ashworth. A series pressure drop representation for flow through orifices. *Journal of Fluids Engineering*, 130, 2008.

[26] E. Jassim, T. Newell, and J. Chato. Two-phase flow visualization in chevron and bumpy style flat plate heat exchangers. *Heat transfer engineering*, 27:20, 2006.

[27] E.W. Jassim. Probabilistic flow regime map modeling of two-phase flow. Thesis, University of Illinois, 2001.

[28] D.S. Kim. Solar absorption cooling. Phd thesis, Technical University Delft, 2007.

[29] H.J. Kim, L. Liebenberg, and M. Jacobi. Flow visualization of two-phase refrigerant r-245fa in a brazed plate heat exchanger near the micro-macro scale transition. *International Conference on Boiling and Condensation Heat Transfer*, 5:27–32, 2018.

[30] L. Kuikhoven. Influence of ammonia concentration on the performance of otec power cycles. Master's thesis, Delft University of Technology, 2016.

[31] Brain Research lab. Plexiglass chemical resistance properties. `https://www.brainresearchlab.com/wp-content/uploads/Plexiglass-Chemical-Resistance-Properties.pdf`. [Accessed:15-10-2018].

[32] Granta Design Limited. Ces edupack, 2018.

[33] G. Longo. Heat transfer and pressure drop during hfc refrigerant saturated vapour condensation inside a brazed plate heat exchanger. *Int. J. Refrigeration*, 33:944–953, 2010a.

[34] G. Longo. Heat transfer and pressure drop during hydrocarbon refrigerant condensation inside a brazed plate heat exchanger. *Int. J. Refrigeration*, 33:944–953, 2010b.

[35] M.A. Lovich and V.P. Carey. Assessment of the combined pressure drop and heat transfer performance of a cross-ribbed channel geometry in a compact evaporator cold plate. *Heat transfer 1990*, 5:27–32, 1990.

[36] J. Lutgendorf. Structural design of glass geometries. Master's thesis, Delft University of Technology, 2014.

[37] AZO Materials. Polymethylmethacrylate - acrylic - pmma general purpose. `https://www.azom.com/article.aspx?ArticleID=788`, 2000. [Accessed:15-8-2018].

[38] K. Nilpueng and S. Wongwises. Two-phase gas–liquid flow characteristics inside a plate heat exchanger. *Experimental thermal and fluid science*, 34:1217–1229, 2009.

[39] T. Oshinowo and M. Charles. Vertical two-phase flow part i flow pattern correlations. *The Canadian Journal of Chemical Engineering*, 52:25–36, 1974.

[40] R.H. Perry, D.W. Green, and D.E. Ackers. *Perry's chemical engineers handbook.* McGraw-Hill, 1963.

[41] Nalgene Labwear Thermo Scientific. Chemical compatibility guide. `http://www.Nalgenelabwear.com`, 2008. [Accessed 20-10-2018].

[42] R.F. Scrutton. The ductile-brittle transition when machining perspex. *International Journal of Production Research*, 4:3–9, 2007.

[43] P. Stephan, H. Martin, S. Kabelac, D. Mewes, M. Kind, and K. Schaber. *VDI Heat Altas*. Springer, 2010.

[44] X. Tao, M.E. Dahlgren, and C.A. Infante Ferreira. Condensation heat transfer and pressure drop of nh3 and nh3/h2o within a plate heat exchanger. *13th IIR Gustav Lorentzen Conference on Natural Refrigerants. Valencia, Spain*, 2018.

[45] X. Tao, M.P. Nuijten, and C.A. Infante Ferreira. Two-phase vertical downward flow in plate heat exchangers, flow patterns and condensation mechanisms. *International Journal of Refrigeration*, 85:489–510, 2018.

[46] J. Thulukkanam. *Heat exchangers design handbook*. CRC press, 2013.

[47] Engineering Toolbox. Friction and friction coefficients. `https://www.engineeringtoolbox.com/friction-coefficients-d$_$778.html`, 2000. [Accessed:20-8-2018].

[48] C. Tribbe and H. M. Müller-Steinhagen. Gas/liquid flow in plate-and-frame heat exchangers - part i: Pressure drop measurements. *Heat transfer engineering*, 22:5–11, 2001a.

[49] C. Tribbe and H. M. Müller-Steinhagen. Gas/liquid flow in plate-and-frame heat exchangers - part ii: two-phase multiplier and flow pattern analysis. *Heat transfer engineering*, 22:12–21, 2001b.

[50] F.A. Veer. The strength of glass, a nontransparent value. *Heron*, 52, 2007.

[51] P. Vlasiogiannis, G. Karagiannis, P. Argyropoulos, and V. Bontozoglou. Air-water two-phase flow and heat transfer in plate heat exchanger. *International journal of multiphase flow*, 28:757–772, 2001.

[52] G. B. Wallis. *One-dimensional two-phase flow*. McGraw-Hil, 1969.

[53] L.K. Wang, B. Sundén, and Q.S. Yang. Pressure drop analysis of steam condensation in a plate heat exchanger. *Heat Transfer Engineering*, 20:71–77, 1999.

[54] H. Westergaard. Stresses in concrete pavements computed by theoretical analysis. *Public roads*, 7:25–35, 1926.

[55] A.A.J. Willighagen. Polymer heat exchangers for ocean thermal energy conversion. Master's thesis, Delft University of Technology, 2017.

[56] D. Winkelmann. Condensation of pure refrigerants and their zeotropic mixtures in plate heat exchangers. Master's thesis, Technischen Universität Berlin, 2010.

[57] Z. Xue, W. Qu, and M. Xie. Full visualization and startup performance of an ammonia pulsating heat pipe. *Propulsion and power research*, 2, 2013.

[58] J. Zhang, H. Zhang, and J. Zhang. Evaluation of liquid ammonia treatment on surface characteristics of hemp fiber. *Cellulose*, 21:569–579, 2014.

[59] L. Zhao and K.S. Rezkallah. Gas-liquid flow patterns at micro-gravity conditions. *International Journal of Multiphase Flow*, 19:751–763, 1993.

[60] S.M. Zivi. Estimation of steady-state steam void-fraction by means of the principle of minimum entropy production. *J. Heat Transfer*, 86:247–252, 1964.